Universität Bremen

ZENTRUM FÜR
ANGEWANDTE RAUMFAHRTTECHNOLOGIE
UND MIKROGRAVITATION

ZARM

ZARM
Applied Space Technology and
Microgravity

Master Thesis:

Study of Space-Environmental Effects on Interplanetary Trajectories

Moritz Huckfeldt
moritz.huckfeldt@uni-bremen.de

Matriculation Number: 4123353
Course of Study: Space Engineering I

First Reviewer: Prof. Dr. Claus Braxmaier
Second Reviewer: Dr.-Ing. Benny Rievers

December 13, 2020

Eigenständigkeitserklärung

Hiermit bestätige ich, dass die vorliegende Arbeit von mir selbständig verfasst wurde, ich keine anderen als die angegebenen Hilfsmittel – insbesondere keine im Quellenverzeichnis nicht benannten Internet-Quellen – benutzt habe und die Arbeit von mir vorher nicht in einem anderen Prüfungsverfahren eingereicht wurde. Die eingereichte schriftliche Fassung entspricht der auf dem elektronischen Speichermedium. Ich bin damit einverstanden, dass die Masterarbeit veröffentlicht wird.

Bremen, 13. Dezember 2020, Moritz Huckfeldt

Abstract

Since the early 90s of the last century, when the Galileo spacecraft used Earth for two gravity-assist manoeuvres, scientist puzzle over the origin of an unexpected velocity difference associated with Earth-gravity assists. As this is not limited to one occurrence but was detected for several spacecraft, numerous scientific papers about this so called Flyby Anomaly have been published since then, trying to explain the velocity change with various physical relations. However, no scientifically sound explanation has been found up to today.

The aim of this master thesis is the simulation of interplanetary trajectories of flown missions, the comparison of the simulation results to the measurement data and the evaluation of the use of the High Performance Satellite Dynamics Simulator (HPS) in analyses of the Flyby Anomaly. The simulations are done with the HPS, a simulation tool developed at ZARM. For the HPS to be able to simulate gravity assists, the source code has to be adapted. This master thesis includes a short review of the current state of the art regarding the simulation of interplanetary trajectories and possible Flyby-Anomaly explanations. The theoretical background for the the orbital dynamics of interplanetary trajectories, perturbation forces acting on a spacecraft and necessary coordinate transformations are presented as well. The results of the customized HPS are evaluated to ensure accurate simulations. Based on literature recommendations and the to examined Flyby Anomaly, the influence of gravitational effects and non-gravitational perturbations on the simulations are investigated. Using the tracking data of the explored space-flight mission as a comparison, the results of the simulations are discussed and evaluated.

The results show which perturbations are essential for an adequate precision and which can be neglected. Further, different attitudes are compared and the mostly unknown attitude of the examined spacecraft is validated. Regarding the application of the HPS for the analysis of the Flyby Anomaly it is detected that velocity difference of the studied non-gravitational perturbations at the periapsis has the wrong sign. However, small errors in the investigated non-graitational perturbations could produce velocity changes similar to the anomaly.

Zusammenfassung

Seit den frühen 90er Jahren des letzten Jahrhunderts, als bei dem Vorbeiflug der Galileo Sonde, eine unerwartete Differenz zwischen eintreffender und verlassender Geschwindigkeit des Raumfahrzeugs festgestellt wurde, rätseln Wissenschaftler über den Ursprung dieses Erdflybyphänomens. Da diese Entdeckung nicht auf eine Instanz limitiert ist, sondern bei mehreren Raumfahrzeugen erkannt wurde, wurden seitdem mehrere wissenschaftliche Untersuchungen bezüglich möglicher Gründe dieser so genannten Flyby Anomalie veröffentlicht. Bis heute wurde jedoch keine wissenschaftlich plausible Erklärung gefunden.

Das Ziel dieser Masterarbeit ist das Simulieren interplanetarer Flugbahnen von geflogenen Missionen, der Vergleich der Simulationsergebnisse zu Messdaten und die Beurteilung des High Performance Satellite Dynamics Simulator (HPS) zur Analyse der Flyby-Anomalie. Die Simulationen werden mit dem HPS, eines am ZARM entwickelten Simulationstools, durchgeführt, wessen Quellcode für die Simulation von interplanetaren Flugbahnen angepasst werden muss. Diese Masterarbeit gibt einen kurzen Überblick über den Stand der Technik bezüglich der Simulation von interplanetaren Missionen und möglicher physikalischer Erklärungen der Flyby Anomalie. Außerdem werden die nötigen theoretischen Hintergründe für die Orbitmechanik, auf das Raumfahrzeug wirkende Störkräfte und notwnedige Koordinatentransformationen erläutert. Die Ergebnisse des angepassten HPS werden zur Sicherstellung der Richtigkeit evaluiert. Darauffolgend können Untersuchungen bezüglich der gravitativen Effekte und nicht-gravitativen Störkräfte basierend auf Literaturempfehlungen und der zu untersuchenden Flyby Anomalie stattfinden. Weitere Simulationsergebnisse werden bezogen auf die Messdaten ausgewertet und diskutiert.

Die Ergebnisse zeigen, welche Störkräfte notwendig für eine ausreichende Genauigkeit sind und welche vernachlässigt werden können. Des Weiteren werden verschiedene Ausrichtungen des Raumfahrzeugs verglichen und anhand der Simulationen kann die überwiegend unbekannte wirkliche Ausrichtung bestätigt werden. Bezüglich der Anwendung des HPS zur Analyse der Flyby Anomalie lässt sich feststellen, dass das Vorzeichen des Geschwindigkeitsunterschieds am Perizentrum für keine der nicht-gravitativen Störkräfte mit der Flyby-Anomalie übereinstimmt. Jedoch könnten schon kleine Abweichungen in den Modellen der untersuchten nicht-gravitativen Störgrößen für Geschwindigkeitsunterschiede von ähnlicher Größe der Anomlie verantwortlich sein.

Contents

List of Figures

List of Tables

Nomenclature

List of Acronyms and Abbreviations

Alb	albedo
ANSYS	Analysis System
C3BM	complete three-body model
CERES	Cloud and Earth's Radiant Energy System
cFPA	constant flight path angle
CIP	Celestial Intermediate Pole
CoM	centre of mass
DE	Development/Lunar Ephemeris
DPODP	Double-Precision Orbit Determination Program
ECEF	Earth-centred, Earth-fixed
ECI	Earth-centred inertial
EGA	Earth-gravity assist
Eq	Equation
FE	finite elements
FK5	Fifth Fundamental Catalogue
GCRF	Geocentric Celestial Reference Frame
GCRS	Geocentric Celestial Reference System
GMAT	General Mission Analysis Tool
GRACE	Gravity Recovery and Climate Experiment
HCI	Heliocentric Ecliptic Inertial
HGA	high-gain antenna
HPS	High Performance Satellite Dynamics Simulator
IAU	International Astronomical Union
ICGEM	International Centre for Global Earth Models
ICRF	International Celestial Reference Frame
ICRS	International Celestial Reference System
IEEE	Institute of Electrical and Electronics Engineers
IERS	International Earth Rotation and Reference Systems Service

IR	infrared
ITRF	International Terrestrial Reference Frame
ITRS	International Terrestrial Reference System
JB2008	Jacchia-Bowman empirical thermospheric density model
JGM-3	Joint Gravity Model
JPL	Jet Propulsion Laboratory
LAGEOS	Laser Geodynamics Satellite
LEO	Low-Earth orbit
LoS	line of sight
NASA	National Aeronautics and Space Administration
NEAR	Near Earth Asteroid Rendezvous
NHPS	new High Performance Satellite Dynamics Simulator
OoM	Order of Magnitude
SC	spacecraft
SHM	spherical harmonics Earth potential field model
SoI	Sphere of Influence
SRP	solar radiation pressure
SSB	solar-system barycentre
TDB	Barycentric Dynamical Time
TRP	thermal radiation pressure
TT	Terrestrial Time
VLBI	Very Long Baseline Interferometry
ZARM	Zentrum für angewandte Raumfahrttechnologie und Mikrogravitation

List of Symbols

α	view angle, °; deflection angle, °; absorptivity
β	angle of asymptote, °
Δ	difference
Δv_p	Flyby Anomaly
δ	offset, °
ε	emissivity; obliquity
λ	longitude, °; wavelength
Λ	entry of look-up table for thermal radiation pressure
μ	gravitational parameter, $\mathrm{m}^3\,\mathrm{s}^{-2}$
∇	Nabla operator
ν	true anomaly, °
ν_∞	true anomaly of asymptote, °
Ω	solid angle, sr; longitude of ascending node, °
ω	argument of periapsis, °

Φ	potential, $\mathrm{m^2\,s^{-2}}$; radiant flux, W
ϕ, θ, ψ	rotation angle, $^\circ$
ϕ	latitude, $^\circ$
ρ	density, $\mathrm{kg\,m^{-3}}$; reflectivity
σ	Stefan-Boltzmann constant, $\mathrm{W\,m^{-2}\,K^{-4}}$
θ	azimuth angle, $^\circ$
θ_S	angle between Sun and normal vector, $^\circ$
ξ, η, ζ	Cartesian vector components
$\boldsymbol{\omega}$	rotational velocity vector, $\mathrm{s^{-1}}$
A	area, $\mathrm{m^2}$
a	semi-major axis, m
C, S	Stokes' coefficients
c	speed of light, $\mathrm{m\,s^{-1}}$
$C_{i,n}$	Chebychev coefficient
C_D	drag coefficient
C_R	radiation pressure coefficient
E_{exp}	exponent of Earth-Sun distance
e	eccentricity
$f(x)$	function of x
f_{s1}, f_{s2}	scale factor
F	focal point; hyperbolic eccentric anomaly
f	factor
G	gravitational constant, $\mathrm{m^3\,kg^{-1}\,s^{-2}}$
h_p	periapsis altitude, m
i, j, k, l	nodal identification number
$\overline{ij}$	vector from i to j, m
I	eclipse condition
i	inclination, $^\circ$
J	zonal coefficient
JD	Julian days
l	degree
L	radiance, $\mathrm{W\,sr^{-1}\,m^{-2}}$
M, m	mass, kg
M	exitance, $\mathrm{W\,m^{-3}}$; mean anomaly
m	order
n	number of
O	origin, order
$P(x)$	approximation of x
P	Legendre polynomial; point
p	pressure, $\mathrm{kg\,m^{-1}\,s^{-2}}$; point

Q	heat flux, $\mathrm{W\,m^{-2}}$
q	point
R	radius, m
r	distance, radius, m
S_0	solar irradiance, $\mathrm{W\,m^{-2}}$
SC_{exp}	exponent of spacecraft-Sun distance
s	variable for evaluation of Chebychev polynomial
T	temperature, K; Julian centuries
T_n	Chebychev polynomial of first kind
t	time, s
V	volume, $\mathrm{m^3}$
v	velocity, $\mathrm{m\,s^{-1}}$
x, y, z	Cartesian vector components
$\boldsymbol{A}$	dominating gravitational acceleration vector, $\mathrm{m\,s^{-2}}$
$\boldsymbol{a}$	acceleration vector, $\mathrm{m\,s^{-2}}$
$\boldsymbol{e}$	basis vector
$\boldsymbol{F}, \boldsymbol{f}$	force vector, N
$\boldsymbol{h}$	angular momentum vector, $\mathrm{m^2\,s^{-1}}$
$\boldsymbol{n}$	normal vector
$\boldsymbol{n}_h$	local horizontal direction
$\boldsymbol{P}$	perturbing gravitational acceleration vector, $\mathrm{m\,s^{-2}}$
$\boldsymbol{p}$	perturbation, $\mathrm{m\,s^{-2}}$
$\boldsymbol{q}$	attitude quaternion
$\boldsymbol{r}$	position vector, m
$\boldsymbol{T}, \boldsymbol{t}$	torque vector, N m
$\boldsymbol{u}$	line of sight vector
$\boldsymbol{v}$	velocity vector, $\mathrm{m\,s^{-1}}$

List of Subscripts and Superscripts

∞	infinity
0	reference, moving
$3rd$	third body
atm	atmosphere
B	black body
b	body frame
c	cross section
cb	central body
D	Drag
d	diffuse

E	Earth
ecl	ecliptic
equ	equatorial
f	final
g	gravitational
gen	generated
h	heliocentric
hem	hemisphere
i	index, initial
in	incoming, incident
int	interval
j	index
l	lever arm
M	number of
mb	major body
N, n	number of
new	new
ng	non-gravitational
out	outgoing
p	planet
P	point
p	periapsis
ref	reference
rel	relative
s	specular
S	Sun
s	scaled
sh	shadowing
sim	simulation
SR	solar radiation
$start$	start
T	transposed
tot	total
v	volume
$\prime$	rotated; derivation with respect to x
$\dot{}$	first time derivation
$\ddot{}$	second time derivation
$\hat{}$	unit vector
$\bar{}$	normalized

Chapter 1

Introduction

The study of the Galileo spacecraft's Doppler ranging data in December 1990 revealed an unexpected frequency shift between the pre- and post encounter data. However, the second gravity assist of Galileo in 1992 showed no frequency shift. Since then, several spacecraft bound for planets in our solar system came back to Earth to target it for a Gravity-Assist manoeuvre. Its purpose being the gain or loss of heliocentric orbital energy to be able to reach the target body. The tracking and ranging data of some of those spacecraft's flybys showed similar frequency shifts, but not all and no distinct cause could be found. [1] Because of the inconsistency of the anomaly, scientists are trying to explain this phenomenon with different approaches. From standard Newtonian physics due to space phenomena which were not considered in the mission design [2], over general and special relativity influences [3, 4], to unparticle physics based theory [5], to name just a few.
This phenomenon was titled *Flyby Anomaly* by the scientists and its still unknown cause is the motivation for this master thesis as a reliable assessment of gravity assists is of great importance for the design and analysis of space missions. The goal is to simulate a gravity-assist trajectory around Earth including the influence of third-body gravitational accelerations as well as the major non-gravitational perturbations induced on the spacecraft by its surrounding space environment. The distinctive feature of the simulation is the utilization of a 3D finite element (FE) model of the spacecraft for a detailed calculation of the non-gravitational perturbations [6].
The baseline tool for the simulation of the spacecraft trajectories is the High Performance Satellite Dynamics Simulator (HPS), providing a MATLAB/Simulink user interface. It was developed to simulate drag-free satellite missions, using numerical integration of the equations of motion. Included in the tool are models of Earth's gravitational and magnetic field, ephemerides of other planets, as well as modules regarding external forces and torques

due to the space environment by means of finite elements. [6] In the course of this master thesis the HPS is adapted for the simulation of interplanetary trajectories and gravity assists. The changes are described in Chapter 5, the evaluation of the new model is reported in Chapter 6 and the description of the detailed simulation procedure of the HPS is given in Chapter 4.
By means of 3D modelling already flown spacecraft and using tracking data as initial conditions for the simulations, the real trajectories are reproduced as accurate as possible. Beforehand, gravitational effects and non-gravitational perturbations are studied with respect to their influence on the simulated trajectories. The magnitude of the non-gravitational effects is also evaluated for varying attitudes to validate the mostly unknown actual attitude of the real spacecraft. Derived from the influence of each non-gravitational perturbation a statement about possible causes of the Flyby Anomaly is made. Conclusively, based on the remaining differences between simulation and tracking data a crude survey about the general behaviour of the simulation for differing initial inputs is performed. The results of the studies and comparisons are presented in Chapter 7.

1.1 Task Description

The definitions of the tasks for this master thesis were formulated as stated below.

1. Adaptation of the successfully used satellite-mission-simulation platform HPS, such that interplanetary trajectories can be computed. This includes the incorporation of changes of the dynamic core, to enable the switching of the gravitational main body on basis of the Sphere of Influence (SoI).

2. Simulation of interplanetary trajectories of flown spacecraft, whose position and velocity were tracked with sufficient accuracy, regarding all relevant perturbations. Parameter analysis with respect to the unknown or not precisely known parameters (e.g. attitude, surface properties) to estimate an overall error of the simulation

3. Comparison and evaluation of the simulation results to the measurement data.

Chapter 2

Theoretical Background

In this chapter, the fundamental principles of space flight are explained as they are necessary to understand the simulation of interplanetary trajectories. This includes the equations of motion, which describe the motion of a body under influence of external accelerations, as well as perturbing accelerations on the flight path. Additionally, the reference frames used for the simulation and the transformation procedures between those frames are described.

2.1 Orbital Dynamics

All of the equations described in this chapter are of Newtonian nature because the simulation tool used in this master thesis utilizes Newtonian laws. This theory of gravity describes the laws of gravity accurately enough for most astronautical problems. However, relativistic descriptions of the laws of gravity result in a higher precision needed to account for discrepancies between observations and Newtonian predictions of particular events [7, p. 2]. Therefore, it is deemed adequate to use a relativistic correction term to increase the precision in the space-flight simulations.

2.1.1 Equations of Motion

Regarding Newton's postulation that all masses experience forces of attraction from each other which are proportional to the product of their masses and inversely proportional to the squared distance between their centres of mass (CoM) [8, p. 46], the resulting equation reads as follows [7, p. 3]:

$$\boldsymbol{F}_g = -\frac{MmG\boldsymbol{r}}{r^3}. \tag{2.1}$$

$\boldsymbol{F}_g$ denotes the gravitational force, M and m the masses of two bodies, G the universal gravitational constant and $\boldsymbol{r}$ the position vector of the body of mass m with respect to the body of mass M. The Euclidean distance between the CoM of the two bodies is indicated with r.
In addition to gravitational influences a body moving through space experiences non-gravitational accelerations. These terms are commonly called perturbations, as they yield a diversion from a Keplerian orbit. The equation of motion can be written as the addition of a gravitational and non-gravitational acceleration ($\boldsymbol{a}_g$ and $\boldsymbol{a}_{ng}$, respectively):

$$\boldsymbol{a} = \boldsymbol{a}_g + \boldsymbol{a}_{ng}. \tag{2.2}$$

2.1.1.1 Two-Body Model

For this section, M denotes the mass of the central body (i.e. Earth) and m the mass of the observed body, for example a satellite. Therefore, $\boldsymbol{r}$ can be interpreted as the satellite's position vector. The universal gravitational constant and the mass of the central body can be multiplied to describe the gravitational parameter μ.

Newtonian Gravity
Assuming that the satellite's mass is several orders of magnitude (OoM) smaller than Earth's and using the following relation of force, acceleration and mass,

$$\boldsymbol{F}_g = -\frac{MmG\boldsymbol{r}}{r^3} = m \cdot \boldsymbol{a}, \tag{2.3}$$

the gravitational acceleration acting on the satellite due to the central body can be derived:

$$\boldsymbol{a} = -\frac{\mu\boldsymbol{r}}{r^3}. \tag{2.4}$$

Considering that Earth is the dominating gravitational body influencing a satellite, Eq. (2.4) is sufficient to describe the satellite's flight path [9, p. 9f.]. Based on these assumptions, the system is called *two-body system*. It is mostly used for planet-bound orbits.

However, this system and Eq. (2.4) are simplifications. Eq. (2.4) can be used if the central body is assumed to be symmetrical and homogeneous and its mass can be concentrated at its centre [7, p. 3]. In reality, most celestial bodies are neither symmetrical nor homogeneous, thus more complex formulations are necessary to describe their gravitational influence. For Earth, detailed models of its gravitational potential are available and should be incorporated for space-flight simulations. Those models are for example based on Gravity Recovery And Climate Experiment (GRACE) data and are available from the International Centre for Global Earth Models (ICGEM) homepage [10]. The influence of other celestial bodies in the solar system are OoM smaller than Earth's gravitation but have to be considered for precise simulations. They can be computed as small perturbations to the two-body system [9, p. 10]. Those effects, in addition to non-gravitational influences on the satellites flight path, are described in Section 2.1.2.

Spherical Harmonics Earth Potential Field

The tool used for this master thesis, the HPS, uses two different representations for a more precise calculation of the gravitational acceleration acting on a satellite [6, p. 147].

As stated before, the Newtonian Eq. (2.4) only holds for the acceleration of a point mass. The same holds true for Eq. (2.1). To calculate the attractive force of a body with varying density ρ in the volume V acting on a point mass m at point p outside the body, one needs to solve the volume integral. This integral can be expressed as the sum of all forces produced by infinitely many and small mass elements $\rho \mathrm{d}V$. Dividing by the sample mass gives the acceleration-vector field describing the gravitational field of the central body [11, p. 2]:

$$\boldsymbol{a}(p) = G \int_V \frac{\rho(q)}{r^2} \frac{\boldsymbol{r}}{r} \mathrm{d}V(q), \tag{2.5}$$

where $\boldsymbol{r}$ is the vector from point p to the volume element $\mathrm{d}V$ at point q in the body. The vector field $\boldsymbol{a}$ can be described by a scalar field Φ by the following relation:

$$\boldsymbol{a}(p) = \nabla \Phi(p). \tag{2.6}$$

Here, ∇ denotes the Nabla operator and Φ is called potential [11, p. 2]. Following Eq. (2.5) the gravitational potential of a body can be described by:

$$\Phi(p) = G \int_v \frac{\rho(q)}{r} \mathrm{d}V(q), \tag{2.7}$$

which satisfies Poisson's equation:

$$\nabla^2 \Phi(r) = -4\pi G \rho(r), \tag{2.8}$$

where ∇^2 denotes the Laplace operator. For positions r outside of the body the density ρ is zero and the potential satisfies the Laplace equation:

$$\nabla^2 \Phi(r) = 0. \tag{2.9}$$

A function that satisfies Laplace's equation is called harmonic function. The theory of harmonic functions states that the knowledge of one equipotential surface is sufficient to define a harmonic function. An equipotential surface visualizes a potential and means that the potential has the same value across the whole surface. [11, p. 2]
To approximate the gravitational potential of e.g. Earth, an appropriate mathematical formulation is needed. Out of all possible representations, the solid spherical harmonics are used almost exclusively for the modelling. Solid spherical harmonics are an orthogonal set of equations that satisfy Laplace's equation (Eq. (2.9)) in spherical coordinates. The gravitational potential Φ at an arbitrary point (r, λ, ϕ) on or above Earth's surface can be expressed as the sum over a degree and order of a spherical harmonic expansion:

$$\Phi(r, \lambda, \phi) = \frac{GM}{r} \sum_{l=0}^{l_{max}} \sum_{m=0}^{l} \left(\frac{R_E}{r}\right)^l \bar{P}_{lm} \sin(\phi) \left(\bar{C}_{lm} \cos(m\lambda) + \bar{S}_{lm} \sin(m\lambda)\right). \tag{2.10}$$

The following list contains the notation of the equation above.

r, λ, ϕ	- spherical geocentric coordinates (radius, longitude, latitude)
R_E	- Earth's reference radius
GM	- gravitational constant and Earth's mass
l, m	- degree and order of spherical harmonic
$\bar{P}_{lm}$	- normalized Legendre polynomial
$\bar{C}_{lm}$, $\bar{S}_{lm}$	- normalized Stokes' coefficients

Further descriptions of the functions and coefficients can be found in Global Models by Barthelmes [11].
The spherical harmonics Earth potential field model (SHM) is the most precise approximation of Earth's potential field used by the HPS. A second model of the potential field can be selected in the HPS as well. For this second model, Eq. (2.10) is simplified to a certain degree. In this case Earth's potential field is assumed to be rotationally symmetric. Therefore, the potential does not depend on the azimuth angle θ, respectively on the longitude

λ [12, p. 662]. The model contains only zonal harmonic coefficients J_n and is dependent on the latitude ϕ. The terms of sine of $m\lambda$ and the cosine of $m\lambda$ reduce to zero and one, respectively. With the relation [13, p. 1]

$$J_n = -C_{n0}, \tag{2.11}$$

Eq. (2.10) is reduced to [6, p. 147]:

$$\Phi\left(r, \lambda, \phi\right) = \frac{GM}{r} \sum_{n=0}^{n_{max}} \left(\frac{R_E}{r}\right)^n \bar{J}_n \bar{P}_{n0} \sin\left(\phi\right). \tag{2.12}$$

Here, the degree is denoted by n and the remaining notation is the same as in the list above.

2.1.1.2 Interplanetary Trajectories

Due to the fact that more than two bodies need to be considered during interplanetary trajectories, the terminology is clarified in the following before describing the solution possibilities. Because the definition of *satellite* states that it is an artificial object orbiting around a planet or moon [14], in the following the terminology *spacecraft* is used for the observed body. The term interplanetary trajectory implies that the spacecraft (SC) is not on an orbit around one planet but moves between planets. Yet, it is still in a bound orbit around the centre of the solar system [8, p. 110f.]. If the trajectory shall describe the transfer from one planet to another, the problem includes four bodies: the departing and target body, the central body and the spacecraft [8, p. 111]. Because this master thesis investigates hyperbolic trajectories around Earth, the problem can be reduced to three bodies. The Sun is denoted as the *central body*, as it is located at the centre of the solar system and Earth is called *major body*. Both declarations are in accordance to Kemble [15, p. 168]. For the mathematical description of interplanetary trajectories several methods can be utilized. Variations of the segmentation of the trajectory, like the patched conics method, or a numerical calculation with a multi-body model.

Patched Conics

One possibility to calculate interplanetary trajectories is to sequence the trajectory into smaller parts depending on the closest body, or more precisely on which body's gravity is dominating [15, p. 168f.]. Planetary transfers are split into at least three legs, those legs can then be calculated with the two-body model, which defines the flight path as conical sections [9, p. 12ff.]. The geometrical form of the legs give this method its name - *Patched Conics*.

The first leg is the approach of the major body (mb) and describes a part of an orbit around the central body (cb), either an ellipse or hyperbola. The second segment is the leg around the major body, which is assumed to be a hyperbola for this thesis. The third leg is the departure from the major body, which can also be one of the two types mentioned for the approach. [15, p. 168]
The point in which one leg transitions into the next is defined by the gravitational influence of the central and major body. For the two bodies influencing the spacecraft a surface can be found where the ratios of the perturbation through the central body during a motion around the major body and the perturbation through the major body during a motion around the central body are equal [15, p. 138]. The relative position vectors of the three bodies are defined as pictured in Fig. 2.1.

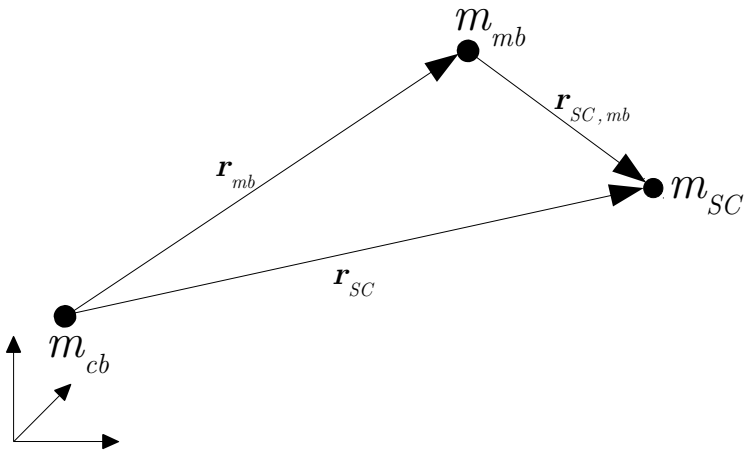

Figure 2.1: *Relative positions of central body, major body and spacecraft*

Using the vector orientation from Fig. 2.1 the equations for the spacecraft acceleration in the above mentioned cases read as follows [9, p. 123]:

$$\boldsymbol{a}_{SC,mb} = -\frac{G\left(m_{mb}+m_{SC}\right)}{r_{SC,mb}^3}\boldsymbol{r}_{SC,mb} - Gm_{cb}\left[\frac{\boldsymbol{r}_{SC}}{r_{SC}^3} - \frac{\boldsymbol{r}_{mb}}{r_{mb}^3}\right], \tag{2.13}$$

$$\boldsymbol{a}_{SC} = -\frac{G\left(m_{cb}+m_{SC}\right)}{r_{SC}^3}\boldsymbol{r}_{SC} - Gm_{mb}\left[\frac{\boldsymbol{r}_{SC,mb}}{r_{SC,mb}^3} + \frac{\boldsymbol{r}_{mb}}{r_{mb}^3}\right]. \tag{2.14}$$

The motion of the spacecraft around the major body including the perturbation is specified in Eq. (2.13) and the perturbed motion around the central body in Eq. (2.14). The first term on both right-hand sides can be shortened

to $\boldsymbol{A}_{mb}$ and $\boldsymbol{A}_{cb}$ respectively, describing the dominating gravitational acceleration due to the major and central body. Assuming that $m_{SC} \ll m_{cb}$ and $m_{SC} \ll m_{mb}$, the multiplication of G and the masses (m_{cb}, m_{mb}) yields the gravitational parameters μ_{cb} and μ_{mb}. The second term on both right-hand sides can be shortened to $\boldsymbol{P}_{cb}$ and $\boldsymbol{P}_{mb}$ respectively, describing the perturbing gravitational acceleration from the central and major body.
The equilibrium of the dominating and perturbing gravitational accelerations,

$$\frac{\boldsymbol{P}_{mb}}{\boldsymbol{A}_{cb}} = \frac{\boldsymbol{P}_{cb}}{\boldsymbol{A}_{mb}}, \tag{2.15}$$

defines the point at which the legs transit from one to the other. This equilibrium represents a near spherical surface and is called the Sphere of Influence (SoI). The centre of the SoI is coincident with the centre of the major body and its radius is given by [9, p. 123f.]:

$$r_{SoI} \approx \left(\frac{m_{mb}}{m_{cb}}\right)^{\frac{2}{5}} r_{mb}. \tag{2.16}$$

For Earth this sphere has a radius of $0.924 \cdot 10^9$ m [8, p. 113].

n-Body Model

A second method to calculate interplanetary trajectories is to consider that the motion of a spacecraft is actually influenced by multiple gravitational bodies. Thus, this method is more precise than the patched conics. Depending on the distance to those bodies, a dominating one cannot be clearly defined and the perturbations of the third bodies in the two-body model are significantly increased. [15, p. 135]
To understand the motion of the spacecraft due to several gravitational bodies the two-body model, namely Eq. (2.4), is expanded. By adding one body to the model one obtains Eq. (2.14) which describes the three-body model [15, p.141]. Adding a second gravitational body to the equation yields that no analytical solution for this model exists. However, the precise motion of the spacecraft can be obtained by numerical integration [15, p. 142]. In the same fashion as for the second body, all other major bodies in the solar system can be added to the equation. This leads to

$$\boldsymbol{a}_{SC} = -\mu_{cb}\frac{\boldsymbol{r}_{SC}}{r_{SC}^3} + \sum_{i=1}^{n}\left(-\mu_i\left[\frac{\boldsymbol{r}_{SC,i}}{r_{SC,i}^3} + \frac{\boldsymbol{r}_i}{r_i^3}\right]\right). \tag{2.17}$$

Here, i denotes the control variable to sum over all considered bodies. The maximum number of possible bodies is denoted by n and can equal twelve,

if for example the number of planets in the solar system, the dwarf planet Pluto and Earth's Moon are considered. If the positions of other bodies in the solar system are known, the number n could also be higher. The position vector of every gravitational body with respect to the centre of the solar system is described with $\boldsymbol{r}_i$, the position of the spacecraft with respect to the gravitational body is $\boldsymbol{r}_{SC,i}$. r_i and $r_{SC,i}$ denote the magnitude of the position vectors. For the gravitational parameter of the additional bodies the sign μ_i is used.
Integrating this differential equation yields the most accurate description of the spacecraft's trajectory, as the only errors arise from integrator drifts, the number of regarded bodies and the accuracy of the gravity model [15, p. 219].

2.1.2 Perturbations

Johannes Kepler was the first scientist to provide laws for planetary motion. His laws were solely based on empirical data and not supported by a fundamental theory. The theory matching his proposed laws was the principle of gravitational force, which was developed by Sir Isaac Newton some decades later. [9, p. 5]
The orbital shape described by Kepler's three laws is called Keplerian Orbit. This kind of motion can only occur under the assumption of two bodies in space. It is known today that not only all bodies with mass influence each other, but that there are also other physical effects controlling the trajectory of everything in space. [12, p. 652] Those effects are called perturbations and can be added as additional acceleration terms to the equations of motion. The most influential effects are described in this chapter.

2.1.2.1 Third-Body Perturbations

Retrospectively to the difference between the two-body and three-body model, the perturbation due to third bodies has already been introduced. Nevertheless, this section describes the equation for the acceleration and the usage of this perturbation.
In Curtis [12] Chapter 12 and Appendix C the geometry of three bodies in inertial space, similar to Figure 2.1, is used to derive the accelerations acting on every body due to the other two. To match the figure in [12] and Figure 2.1, the vector between the spacecraft and the third body has to be turned around in Figure 2.1. Now, $\boldsymbol{r}_{3,SC}$ describes the position of the third body with respect to the spacecraft, which is depicted in Figure 2.2. Using the vector orientation of Figure 2.2, the acceleration on a spacecraft with

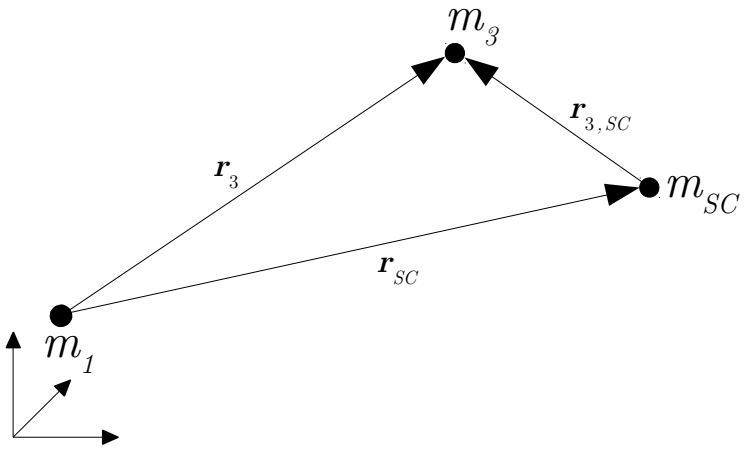

Figure 2.2: *Relative position of body 1, body 3 and spacecraft*

respect to body 1 reads as follows [12, p. 705],

$$\boldsymbol{a}_{SC} = \left(Gm_1 \frac{-\boldsymbol{r}_{SC}}{r_{SC}^3} + Gm_3 \frac{\boldsymbol{r}_{3,SC}}{r_{3,SC}^3} \right) - \left(Gm_{SC} \frac{\boldsymbol{r}_{SC}}{r_{SC}^3} + Gm_3 \frac{\boldsymbol{r}_3}{r_3^3} \right). \tag{2.18}$$

The terms in the first brackets describe the total acceleration of the spacecraft with respect to the centre of the inertial frame due to the other two bodies. The second-bracket terms describe the same for the first body. The first body can for example be Earth and the third body the Moon. Or as for a interplanetary view, the Sun and Earth.
Rearranging Eq. (2.18) and using $\mu = G\left(m_1 + m_{SC}\right)$ and $\mu_3 = Gm_3$ yields,

$$\boldsymbol{a_{SC}} = -\mu \frac{\boldsymbol{r}_{SC}}{r_{SC}^3} + \mu_3 \left(\frac{\boldsymbol{r}_{3,SC}}{r_{3,SC}^3} - \frac{\boldsymbol{r}_3}{r_3^3} \right). \tag{2.19}$$

The second term is the perturbing acceleration due to the third body,

$$\boldsymbol{p}_{3rd} = \mu_3 \left(\frac{\boldsymbol{r}_{3,SC}}{r_{3,SC}^3} - \frac{\boldsymbol{r}_3}{r_3^3} \right), \tag{2.20}$$

with

$$\boldsymbol{r}_{3,SC} = \boldsymbol{r}_3 - \boldsymbol{r}_{SC}. \tag{2.21}$$

Eq. (2.19) is a different representation of Eq. (2.14) and also Eq. (2.17) if n is equal to one. The perturbation term $\boldsymbol{p}_{3rd}$ can be calculated in this shape for every gravitational body. Therefore, the n-Body model is simply the extension of the two-body model by gravitational perturbations.

2.1.2.2 Atmospheric Drag

When a body of mass m and finite dimensions travels through a medium of density ρ it experiences an acceleration in opposite direction of its velocity vector [16, p. 10]. This perturbation is important for spacecraft trajectories near planets with a substantial atmosphere. For Earth, the density is defined by several models up to specific altitudes. The altitude to which the atmosphere is described varies depending on the model, for example up to 2000 km for Jacchia-Roberts or 1000 km for Harris-Priester [17].
The acceleration due to the residual atmosphere can be written as

$$\boldsymbol{a}_D = -\frac{1}{2}\rho v_{rel}^2 \frac{C_D A}{m} \hat{\boldsymbol{v}}_{rel}, \tag{2.22}$$

where $\hat{\boldsymbol{v}}_{rel}$ is the unit-spacecraft-velocity vector relative to the atmosphere, v_{rel} the euclidean norm of $\boldsymbol{v}_{rel}$, C_D the drag coefficient and A the projected area normal to the relative velocity vector. The relative velocity vector is calculated with the inertial velocity of a body and of the atmosphere at the position $\boldsymbol{r}$:

$$\boldsymbol{v}_{rel} = \boldsymbol{v} - \boldsymbol{\omega}_E \times \boldsymbol{r}. \tag{2.23}$$

It can be assumed that the atmosphere rotates with Earth with the same velocity, therefore the velocity of the atmosphere can be calculated by the rotational velocity vector $\boldsymbol{\omega}_E$ cross-multiplied with the spacecraft's position vector. [12, p. 656ff.]

2.1.2.3 Solar Radiation Pressure

The photosphere is the visible surface of the Sun. It acts like a black body emitting radiation over most of the electromagnetic spectrum. This solar radiation is comprised out of photons, which have no mass, but energy and momentum greater zero [12, p. 695]. Because of the momentum, the photons have an accelerative effect on a body. Using the radiation power of the Sun, the acceleration can be quantified. According to the Stefan-Boltzmann law for a black body and the inverse square law that governs the propagation of electromagnetic radiation in space, the radiation intensity S at the distance r from the Sun's centre is:

$$S = \sigma T^4 \left(\frac{R_0^2}{r^2}\right). \tag{2.24}$$

With R_0 describing the radius of the photosphere and r one astronomical unit, S is equal to $1367\,\mathrm{W/m^2}$, which is also known as the *solar constant*. [12, p. 695]
Through the devision of S with the speed of light, a momentum flux is calculated, which is also called *solar radiation pressure*. With the momentum flux, the solar radiation perturbation acting on a body can be calculated as follows:

$$\boldsymbol{a}_{SRP} = -I\frac{S}{c}\frac{C_R A}{m}\hat{\boldsymbol{u}}. \tag{2.25}$$

The first variable I represents the eclipse condition with a factor between zero and one. It describes if the line of sight (LoS) from the Sun to the body is obstructed by another body or not. Using again the example of a satellite orbiting Earth, the satellite can be partially or totally shadowed or not shadowed at all by Earth. Which leads to the following eclipse conditions [6, p. 207]:

Partial Eclipse	$I = (0, 1)$
Annular Eclipse	$I = (0, 1)$
Total Eclipse	$I = 0$
No Eclipse	$I = 1$

The effect of the surface condition is described by C_R, which is called radiation pressure coefficient and lies between one and two. If all the incoming radiation is absorbed, the surface acts as a black radiator, the coefficient becomes one. If the opposite is the case and all radiation is reflected, the coefficient becomes 2. Which means the momentum of the photons is reversed and the force doubles [12, p. 696].
The body properties are further described by A, the area which is impacted by the radiation, and m, its mass. To define the direction of the acceleration, the unit line of sight vector from the body to the Sun $\hat{\boldsymbol{u}}$ is used. In addition with the negative sign, it can be seen that the acceleration acts away from the Sun [12, p. 696].

2.1.2.4 Earth Albedo and Infrared

The radiation emitted from the Sun and impacting Earth is another source of perturbation due to partial reflection. This radiation is called albedo. The second radiation perturbation coming from Earth is its infrared (IR) emittance. These two phenomena should be considered if the observed body is close to Earth, similar to the drag perturbation. Due to the distance, different from the solar radiation pressure where the source could be assumed as a

point, every part of Earth's surface in the field of view has to be considered as a source of radiation [18]. This is done by incorporating the model of McCarthy and Martin, which divides the fraction of Earth's surface visible from the body into discrete segments dA, as depicted in Figure 2.3.

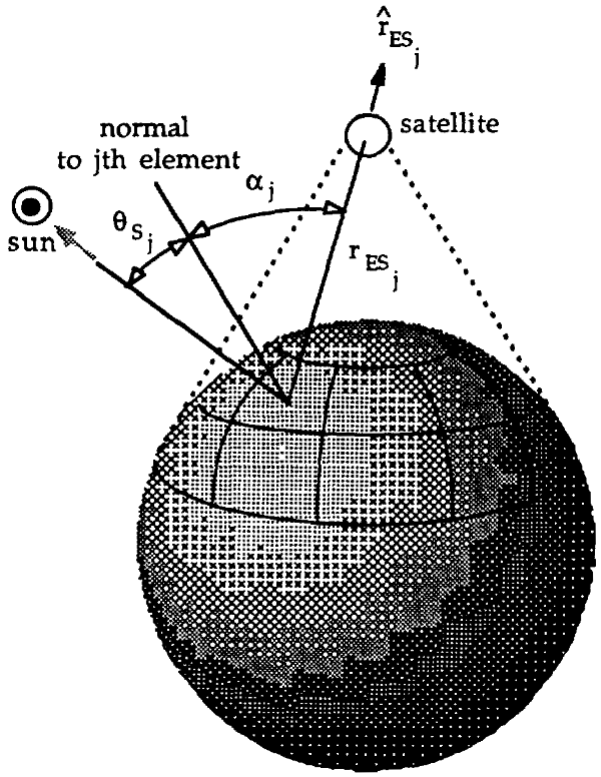

Figure 2.3: *Earth partitioning [19, Fig. 1]*

The segment dA has a certain radiance due to the reflected, as well as the emitted radiation (L_{Alb} and L_{IR}). With the radiance, the fraction of the total flux radiated by dA and intercepted by a surface A_c at the distance r can be calculated:

$$\mathrm{d}\Phi_{tot} = (L_{Alb} + L_{IR}) \frac{A_c}{r^2} \mathrm{d}A \cos(\alpha) . \tag{2.26}$$

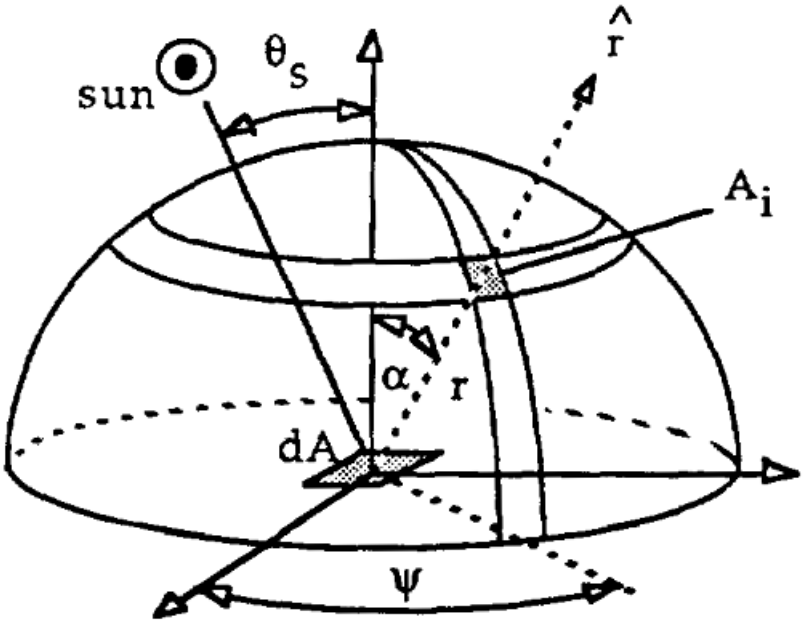

Figure 2.4: *Radiance geometry (Ψ is the azimuth angle θ) [19, Fig. 2]*

According to Knocke [19], who also refers to the model of McCarthy and Martin, the reflective behaviour of Earth's surface can be well approximated as a diffuse reflector. Additionally, the longwave emittance of Earth can also be assumed as purely diffuse. Therefore, Earth can be qualified as a Lambertian surface, meaning it is an purely diffuse emitter and reflector. The reflcetive radiance of the Earth can be quantified as [19]:

$$L_{Alb} = \frac{\rho S \cos(\theta_S)}{\pi}. \tag{2.27}$$

Here, ρS describes the fraction of the incident solar radiation flux that is reflected at Earth's surface and θ_S the inident angle of the flux as pictured in Figure 2.4. The emissive radiance of Earth is described as a fraction of a black-body radiation as follows: [19],

$$L_{IR} = \frac{\varepsilon M_B}{\pi}. \tag{2.28}$$

ε denotes the emission coefficient, which states the percentage of the black-body exitance M_B (radiation flux per unit area) that is emitted by Earth's surface. The factor π in Eq. (2.27) and (2.28) originates in the calculation of the flux of segment $\mathrm{d}A$ radiating into the hemisphere above it [19]. Finally, the total flux emitted by $\mathrm{d}A$ and intercepted by a body with cross section area A_c (perpendicular to LoS vector) can be calculated by combining Eq. (2.26), (2.27) and (2.28):

$$\mathrm{d}\Phi_{tot} = \left(\rho S \cos\left(\theta_S\right) + \varepsilon M_B\right) \frac{A_c}{\pi r^2} \cos\left(\alpha\right) \mathrm{d}A. \tag{2.29}$$

The acceleration is acting in the direction of the position vector $\boldsymbol{r}$ of the body with respect to Earth segment $\mathrm{d}A$, therefore a unit vector $\hat{\boldsymbol{r}}$ is used in the following equation:

$$\mathrm{d}\boldsymbol{a} = \frac{\mathrm{d}\Phi_{tot}}{mc}\hat{\boldsymbol{r}}. \tag{2.30}$$

This equation describes the acceleration acting on a body due to the radiation of one segment $\mathrm{d}A$. To calculate the total acceleration one needs to sum over all segments $\mathrm{d}A_j$ in the field of view of the body [19]:

$$\boldsymbol{a}_{Alb,IR} = \sum_j \mathrm{d}\boldsymbol{a}_j. \tag{2.31}$$

The field of view is indicated in Figure 2.3 with dotted lines.

2.1.2.5 Thermal Radiation Pressure

In addition to the incident radiation from the Sun and Earth, the emitted thermal radiation of the satellite also leads to a perturbing acceleration [20]. This effect is called thermal radiation pressure (TRP) and depends on the incoming heat flux as well as the heat produced internally. The acceleration is dependent on the temperature of the spacecraft which can be calculated with the Stefan-Boltzmann law from the heat balance if an instant heating/cooling is assumed and heat conduction is neglected:

$$T = \sqrt[4]{\frac{Q_{SR} + Q_{Alb} + Q_{IR} + Q_{gen}}{\sigma \varepsilon A}}. \tag{2.32}$$

For the calculation of the acceleration vector, the spacecraft surface has to be partitioned in i elements. Each element radiates and therefore produces an acceleration normal to its surface:

$$\boldsymbol{a}_{TRP,i} = -\frac{2}{3}\frac{\sigma \varepsilon_i A_i T_i^4}{mc}\boldsymbol{n}_i. \tag{2.33}$$

The variables ε_i, A_i and T_i denote the emissivity coefficient, the area and the temperature of element i, respectively. $\boldsymbol{n}_i$ denotes the normal vector of partition i and the factor of 2/3 is the result of the integration of the cosine law over a hemisphere [18]. The total acceleration is calculated by summing over all surface elements of the satellite, which also defines the direction of the resulting acceleration:

$$\boldsymbol{a}_{TRP} = \sum_{i=1}^{N} \boldsymbol{a}_{TRP,i}. \tag{2.34}$$

A description of the incorporation of the perturbations in the HPS is given in Chapter 4.

2.2 Gravity Assist

The gravity assist is a complex but efficient technique used in space flight. The gravitational field of a planet is used to increase or decrease the kinetic energy of a spacecraft with out the utilization of fuel [9, p. 129]. However, two particularities need to be considered. A gravity assist still abides the conservation laws of momentum and energy and the change of kinetic energy is only apparent in the heliocentric representation.
The interaction between the spacecraft of mass m and the planet of mass M is governed by Newton's third law and the momentum of the system is preserved if frictional losses are neglected [21]. The sum of momentum of spacecraft and planet before and after the encounter are equal:

$$m\boldsymbol{v}_{SC,i} + M\boldsymbol{v}_{p,i} = m\boldsymbol{v}_{SC,f} + M\boldsymbol{v}_{p,f}, \tag{2.35}$$

where $\boldsymbol{v}_{SC,i}$, $\boldsymbol{v}_{p,i}$ denote the initial velocity vectors of spacecraft and planet and $\boldsymbol{v}_{SC,f}$, $\boldsymbol{v}_{p,f}$ the final ones. Rearranged, the equation reads as follows:

$$\boldsymbol{v}_{p,f} - \boldsymbol{v}_{p,i} = \frac{m}{M}\left(\boldsymbol{v}_{SC,f} - \boldsymbol{v}_{SC,i}\right), \tag{2.36}$$

showing that the increase of the spacecraft velocity yields only a very small planet velocity change because of the large difference of their masses, which is neglected in the calculations [21].
Considering the energy conservation, the perspective of observing the gravity assist is important. In the planetocentric frame, the velocity of the spacecraft increases when approaching the planet due to its gravitational acceleration and decreases due to the same effect during departure. Meaning, the magnitude of the velocity vectors far distant from the planet, $v_{\infty,i} \equiv v_{SC,i}$ and $v_{\infty,f} \equiv v_{SC,f}$, are equal, and the orbital energy stays constant [21].
The velocity of the spacecraft in the heliocentric frame composes of the planetocentric spacecraft velocity and the velocity of the planet. Regarding the velocity before and after the encounter and assuming the gravity assist is an instantaneous event in comparison to the whole trajectory, the relations read as follows:

$$\boldsymbol{v}_{h,i} = \boldsymbol{v}_{\infty,i} + \boldsymbol{v}_p, \tag{2.37}$$

$$\boldsymbol{v}_{h,f} = \boldsymbol{v}_{\infty,f} + \boldsymbol{v}_p. \tag{2.38}$$

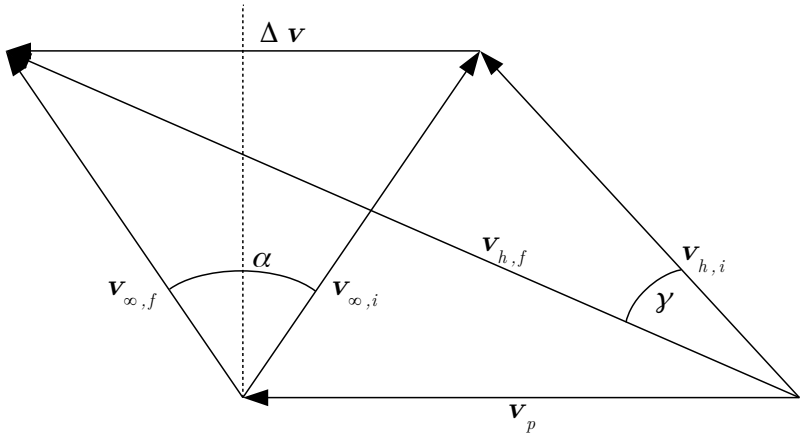

Figure 2.5: *Simplified diagram of a gravity assist*

These equations can be visualised with vectors as depicted in Figure 2.5. In doing so, it becomes apparent that the rotation of the velocity vector in the planetocentric frame leads to a change of the velocity magnitude in the heliocentric frame. The magnitude of the vectors is depicted by the length of the arrows. Using the geometry of the velocity vectors in Figure 2.5 one can derive a simplified equation to approximate a theoretical velocity change achieved by the gravity assist. The angle α, describing the rotation from the incoming to the outgoing velocity vector can be calculated with the eccentricity of the Keplerian hyperbola the spacecraft flies around the planet [15, p. 186]:

$$\alpha = 2 \arcsin\left(\frac{1}{e}\right). \tag{2.39}$$

This angle is called deflection angle and is the double of the angle of the asymptotes β as pictured in Figure 2.6. With α and the Euclidean norm of the asymptotic velocity of the spacecraft $v_{\infty,i}$ the velocity change can be approximated as follows: [9, p. 132]

$$\Delta v = 2 v_{\infty,i} \sin\left(\frac{\alpha}{2}\right). \tag{2.40}$$

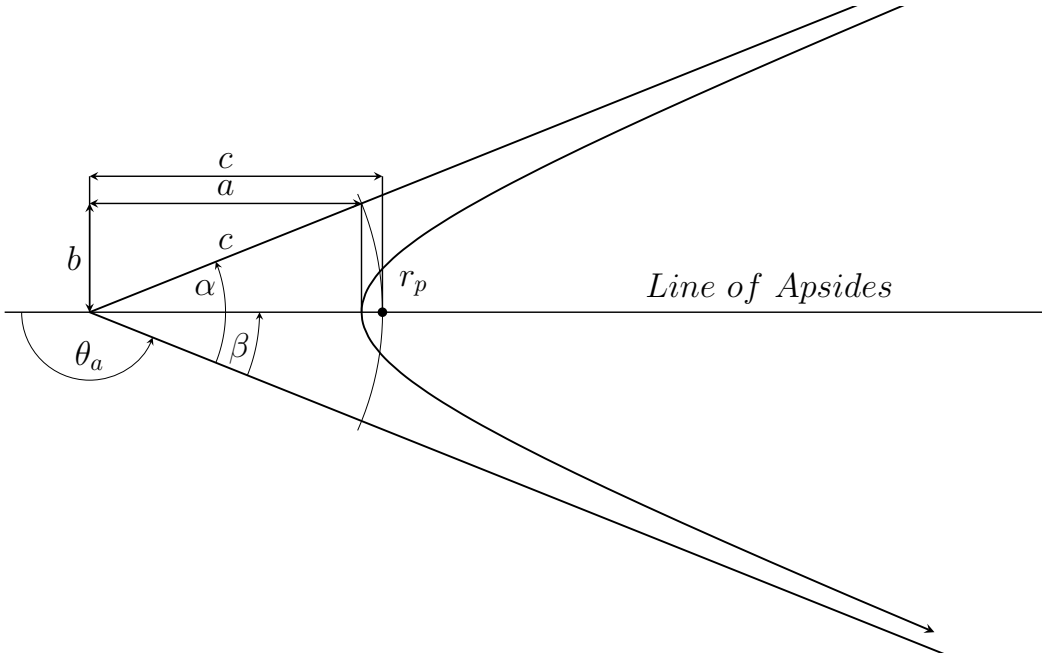

Figure 2.6: *Geometry and elements of a hyperbola based on [8, Fig. 3.10]*

2.3 Coordinate Systems and Their Frames

The position and motion of natural and artificial celestial bodies can be described if there is a system of coordinate axes that are assumed to be fixed in space or whose time variation is precisely known [22, p. I-3].
These axes are referred to as a celestial reference system, which needs to be conventionally defined to ensure comparability of results. To access the system, one needs coordinates of a set of fiducial objects, which is referred to as a celestial reference frame [22, p. I-3].
Due to the fact that the description of spacecraft motion can be done with respect to different celestial bodies, the calculation of perturbations might use a different reference point than the description of spacecraft motion. Thus, all calculations need to be consistent and combinable, the commonly used reference frames and the transformation between them are described in this chapter.
The International Astronomical Union (IAU) is in charge of the definition and maintenance of celestial reference systems. In 1991 the IAU decided to use distant extragalactic objects as the basis of its new reference system. The system's directions were chosen to be fixed with respect to the set of selected objects. The advantage of extragalactic objects as references is that their motion cannot be detected by even the most precise present techniques because of their distance. This is made possible by Very Long Baseline radio Interferometry (VLBI). VLBI measures directions of a distant radio source (e.g. quasars, galactic nuclei) through the difference in arrival time at two distant antennas. A more detailed description of how VLBI is used in global astrometry can be found in the International Earth Rotation and Reference Systems Service (IERS) Technical Note 23 [22].

2.3.1 International Celestial Reference System

With the 1991 recommendation of the IAU the definition of the celestial reference frame was changed from a dynamical definition to a kinematic one. This leads to coordinate axes being fixed with respect to the distant radio sources, instead of adopting privileged axis in the dynamics of Earth's motion in space. Because its orientation is fixed, it is called an inertial frame. To ensure continuity, the previous conventions of the directions due to the mean equator and equinox at the epoch J2000.0 were retained. [22, p. IV-13] The J2000.0 is a standard epoch for the comparison of astronomical data and corresponds to 2451545.0 as a Julian Date or the calender date January 1. 2000 12:00 TT (Terrestrial Time).

The International Celestial Reference System (ICRS) was defined by the IERS and is for example used for the Jet Propulsion Laboratory (JPL) Ephemeris calculation [22, p. I-4]. Its origin is located at the barycentre of the solar system (SSB). The principal plane was defined close to the mean equator at J2000.0 through the IAU conventional precession and nutation. Those two models are error-prone but studies have shown that the ICRS celestial pole has an offset from the mean pole at J2000.0 smaller than 20 mas. Additionally, the IAU recommended that the orientation of new systems should match previous ones. In this case, this is the Fifth Fundamental Catalogue (FK5) in which the pole uncertainty is estimated at 50 milliarcseconds. Therefore, the ICRS is consistent with the FK5 within the uncertainties of the FK5. [22, p. IV-14]
The same recommendation was made for the direction of the right ascension. Its origin was defined close to the dynamical equinox at J2000.0 within the uncertainties of the FK5's right ascension [22, p. IV-14].
The International Celestial Reference Frame (ICRF) is the realization of the ICRS. In accordance to the above stated definitions of the origin O, principal plane and right ascension, the ICRF is oriented as follows:

O	located at SSB
x	in the mean equator plane in direction of the right ascension at J2000.0
z	perpendicular to the mean equator plane in direction of the mean pole at J2000.0
y	builds a right-hand system with x and z-axes

2.3.2 Geocentric Celestial Reference System

The Geocentric Celestial Reference System (GCRS) is the Earth-centred equivalence of the ICRS. It is defined in a way that the transformation between the ICRS and GCRS contains no rotation. This means its orientation is the same as the orientation of the ICRS [23, p. 176]. But due to its position at Earth's centre of mass the transformation has a changing translational component. The realization of this system is called Geocentric Celestial Reference Frame (GCRF) and is defined as follows:

O	located at Earth's CoM
x	in the mean equator plane in direction of the right ascension at J2000.0
z	perpendicular to the mean equator plane in direction of the mean pole at J2000.0

y	builds a right-hand system with x and z-axes

The common name for Earth-centred inertial frames like the GCRS is ECI (Earth-centred, inertial) and they are for example used for the description of satellite orbits.

2.3.3 International Terrestrial Reference System

The International Terrestrial Reference System (ITRS) is the Earth-centred Earth-fixed standard solution for a wide range of applications (geodesy, geophysics, navigation, etc.) [24, p.4]. The realization of this system is called International Terrestrial Reference Frame (ICRF) and it is defined in a way that its origin has no translational or rotational motion with respect to the mean Earth's centre of mass . For this frame several realizations exist, as it is frequently updated. The origin and orientation are always defined at a current epoch and so that there are no change rates with respect to previous realizations [25, p. 12]. According to Boucher [26, 24], the ITRF is defined as follows.

O	located at Earth's CoM
x	in the equator plane in direction of the prime meridian (Greewich meridian)
z	in direction of the celestial pole
y	builds a right-hand system with x and z-axes

Frames like the ITRF are commonly called ECEF (Earth-centred, Earth-fixed) and for example are used in the HPS for the calculation of the gravitational acceleration due to the spherical harmonics Earth potential field as well as the perturbation due to albedo and infrared radiation pressure.

2.3.4 Heliocentric Ecliptic Inertial Frame

In the Astronomical Almanac [27, p. 24ff.] the Heliocentric Ecliptic Inertial Frame (HCI) is defined. Different from the ICRS it is not located at the SSB and its principal plane is not the equatorial plane. Instead, it is located at the centre of the Sun, whose distance to the SSB is very small compared to the mean Earth-Sun distance, and the principal plane is the ecliptic. The ecliptic is the orbital plane of Earth in the solar system and has an angular offset from the equatorial plane called obliquity. The primary axis from which angular coordinates are measured points in direction of the vernal equinox. This is the direction of the Sun from Earth when the Sun lies exactly in the intersection line of ecliptic and equatorial plane.

As the equator, ecliptic and equinox are not inertial but change due to precession and nutation effects, a reference epoch has to be specified to define the orientation [27, p. 25]. Taking the epoch J2000.0 for example, the x-axis of the HCI and ICRF are parallel and the HCI is defined as follows:

O	located at the Sun's CoM
x	in the ecliptic plane in direction of the vernal equinox at J2000.0
z	perpendicular to the ecliptic at J2000.0
y	builds a right-hand system with x and z-axes

With respect to the epoch the HCI is then assumed to be inertial. Even though the definition is several decades old and through VLBI the IERS is able to define systems more precisely, the HCI is still used to describe planetary ephemeris or interplanetary-spacecraft trajectories. The ecliptic is used as the reference plane because most planets only have a slightly inclined orbital plane with respect to to the ecliptic. [28, p. 105ff.]

2.3.5 Coordinate Transformation

This section focuses on the three coordinate transformations needed in the simulation of interplanetary-spacecraft trajectories. The first is the transformation between the ICRF and the HCI. Depending on the method of ephemeris calculation, the planetary positions need to be transformed from the equatorial to the ecliptic plane to calculate the third-body perturbations. Second, the transformation between the HCI and ECI is often used to express the spacecraft's position with respect to Earth for the calculation of Earth's gravitational acceleration and perturbations due to Earth's environment. The third transformation is between the ECI and ECEF, needed for calculations in which the orientation of Earth is important.
The three transformations need a rotational correction if the frames do not have the same orientation and/or a translational correction if the origin of the frames is not at the same position. In the following, the methods of coordinate transformation are explained for one direction only, as the opposite transformation can be achieved by simple inversion of the method, e.g. using the transpose of a rotation matrix [29, p. 5].
At First, the transformation between two frames at different positions but same orientation is described. One frame is assumed to be inertially fixed in space and the other one is moving relatively to the fixed frame. This is a basic representation of a planet moving around the SSB. The geometric relations are depicted in Figure 2.7.

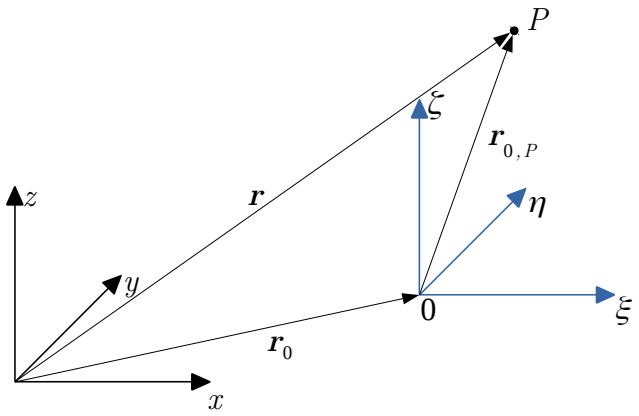

Figure 2.7: *Coordinate frame translation*

The x, y, z-frame is fixed and the ξ, η, ζ-frame is moving translational with respect to the fixed frame. The following formulations are according to Gross et al. [30, p. 277ff.].
The position vector $\boldsymbol{r}$ of point P can be expressed as

$$\boldsymbol{r} = \boldsymbol{r}_0 + \boldsymbol{r}_{0P}, \tag{2.41}$$

where $\boldsymbol{r}_0$ is the position vector of the moving frame with respect to the inertial frame and $\boldsymbol{r}_{0P}$ the position vector of P in the moving frame. $\boldsymbol{r}_{0P}$ which can be expressed in Cartesian form as follows:

$$\boldsymbol{r}_{0P} = \xi \boldsymbol{e}_\xi + \eta \boldsymbol{e}_\eta + \zeta \boldsymbol{e}_\zeta. \tag{2.42}$$

$\boldsymbol{e}_i$ denote the basis vectors of the frame. To express the velocity of point P, Eq. (2.41) is differentiated with respect to time, which is denoted with a dot:

$$\dot{\boldsymbol{r}} = \dot{\boldsymbol{r}}_0 + \dot{\boldsymbol{r}}_{0P}, \tag{2.43}$$

$$\dot{\boldsymbol{r}}_{0P} = \dot{\xi} \boldsymbol{e}_\xi + \dot{\eta} \boldsymbol{e}_\eta + \dot{\zeta} \boldsymbol{e}_\zeta. \tag{2.44}$$

The basis vectors of the moving frame stay constant, as the frame is not rotating. Otherwise, Eq. (2.44) would need to be extended by $\dot{\boldsymbol{e}}_i$ terms. For the definition of the acceleration acting on P in the inertial frame, Eq. (2.43) is differentiated again with respect to time:

$$\ddot{\boldsymbol{r}} = \ddot{\boldsymbol{r}}_0 + \ddot{\boldsymbol{r}}_{0P}, \tag{2.45}$$

$$\ddot{\boldsymbol{r}}_{0P} = \ddot{\xi} \boldsymbol{e}_\xi + \ddot{\eta} \boldsymbol{e}_\eta + \ddot{\zeta} \boldsymbol{e}_\zeta. \tag{2.46}$$

Equations (2.41),(2.43) and (2.45) show that for a transformation from x, y, z to ξ, η, ζ-frame, the position, velocity and acceleration of the moving frame

needs to be known and simply subtracted from the inertial values of point P. Coming back to the numerical simulation of a spacecraft's trajectory, this transformation can be done at specific points in time for which $\boldsymbol{r}_0$, $\dot{\boldsymbol{r}}_0$ and/or $\ddot{\boldsymbol{r}}_0$ of the ξ, η, ζ-frame, meaning for example the ECI or simply Earth, are known.

The second case describes two coordinate frames which have the same origin, but not the same orientation. In this example, two frames with the same principal plane are assumed. Therefore, the transformation can be described by a single rotation. A more complex relative orientation of two frames can be described by a series of rotations.
A rotation around the z-axis by the angle θ is pictured in Figure 2.8, the rotated frame is labelled with primed signs. The position of point P can be described in both reference frames, using $\boldsymbol{r}$ or $\boldsymbol{r}'$ respectively.

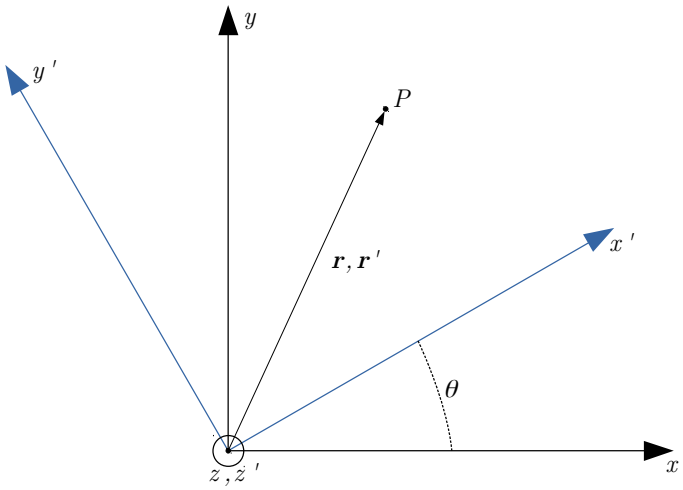

Figure 2.8: *Coordinate frame rotation*

If the position of P is known in the x, y, z-frame but needs to expressed in the primed frame, one method is the multiplication of $\boldsymbol{r}$ with a rotation matrix $\mathbf{R}$ [29, p. 4f.]. This matrix is of size $n \times n$, with n=3 being the size of the vector in three-dimensional space. The angle θ, counted in the mathematically positive sense, describes the rotation of the two frames around one axis. This can be one of the basis axes of one frame or an arbitrary axis defined by any number of rotations around the basis axes [31]. For the basic cases

of rotations around basis axes, the matrices are defined as follows:

$$\mathbf{R}_x = \begin{bmatrix} 1 & 0 & 0 \\ 0 & \cos(\theta) & \sin(\theta) \\ 0 & -\sin(\theta) & \cos(\theta) \end{bmatrix}, \tag{2.47}$$

$$\mathbf{R}_y = \begin{bmatrix} \cos(\theta) & 0 & -\sin(\theta) \\ 0 & 1 & 0 \\ \sin(\theta) & 0 & \cos(\theta) \end{bmatrix}, \tag{2.48}$$

$$\mathbf{R}_z = \begin{bmatrix} \cos(\theta) & \sin(\theta) & 0 \\ -\sin(\theta) & \cos(\theta) & 0 \\ 0 & 0 & 1 \end{bmatrix}. \tag{2.49}$$

Considering the case depicted in Figure 2.8, the coordinate transformation can be written as:

$$\boldsymbol{r}' = \mathbf{R}_z \boldsymbol{r}, \tag{2.50}$$

and its inversion can be calculated with the transposed rotation matrix,

$$\boldsymbol{r} = \mathbf{R}_z^T \boldsymbol{r}'. \tag{2.51}$$

To avoid misunderstanding, the three rotation angles around different axes are called ϕ, θ and ψ. Each rotation can be described by a single rotation matrix. Through multiplication of the matrices the combination of multiple rotations can again be expressed by a single matrix:

$$\mathbf{R}_{x,y,z}(\phi, \theta, \psi) = \mathbf{R}_x(\phi)\, \mathbf{R}_y(\theta)\, \mathbf{R}_z(\psi). \tag{2.52}$$

It is important to note that matrix multiplications are not commutative and need to be done in particular sequences [29, p. 9f.].
For the transformation of velocity and acceleration it is again important to know if one frame has a changing orientation with respect to the other or not. Meaning, if the primed frame has a rotational velocity vector $\boldsymbol{\omega} \neq 0$ or the rotational angle between both frames is constant.
According to the product rule, the derivative with respect to time of Eq. (2.50) is

$$\dot{\boldsymbol{r}}' = \mathbf{R}_z \dot{\boldsymbol{r}} + \dot{\mathbf{R}}_z \boldsymbol{r}. \tag{2.53}$$

Following Gross et al. [30, p. 279] for the kinematics of relative motion, the time derivative of the vector $\boldsymbol{r}'$ in a rotating frame can also be expressed as:

$$\dot{\boldsymbol{r}}' = \frac{\mathrm{d}\boldsymbol{r}'}{\mathrm{d}t} + \boldsymbol{\omega} \times \boldsymbol{r}', \tag{2.54}$$

where the first term can be expressed in the same form as $\dot{\boldsymbol{r}}_{0P}$ in Eq. (2.44) and $\boldsymbol{\omega}$ describes the temporal change of the basis vectors ($\boldsymbol{e}_\xi$, $\boldsymbol{e}_\eta$ and $\boldsymbol{e}_\zeta$):

$$\xi\dot{\boldsymbol{e}}_\xi + \eta\dot{\boldsymbol{e}}_\eta + \zeta\dot{\boldsymbol{e}}_\zeta = \boldsymbol{\omega} \times (\xi\boldsymbol{e}_\xi + \eta\boldsymbol{e}_\eta + \zeta\boldsymbol{e}_\zeta) = \boldsymbol{\omega} \times \boldsymbol{r}'. \tag{2.55}$$

Substituting $\boldsymbol{r}'$ on the right side of Eq. (2.54) with $\mathbf{R}_z\boldsymbol{r}$ yields

$$\dot{\boldsymbol{r}}' = \mathbf{R}_z\dot{\boldsymbol{r}} + \mathbf{R}_z\left(\boldsymbol{\omega} \times \boldsymbol{r}\right). \tag{2.56}$$

According to Zhao [32] any vector $\boldsymbol{\omega} \in \Re^3$ can be expressed with a skew-symmetric operator to convert a cross product of two vectors into a matrix-vector multiplication:

$$[\omega]_\times \equiv \begin{bmatrix} 0 & -\omega_z & \omega_y \\ \omega_z & 0 & -\omega_x \\ -\omega_y & \omega_1 & 0 \end{bmatrix} \in \Re^{3\times 3}. \tag{2.57}$$

Additionally, the time derivative of a rotation matrix can be expressed by

$$\dot{\mathbf{R}}_z = \mathbf{R}_z\left[\omega\right]_\times, \tag{2.58}$$

which yields that Eq. (2.54) is equal to Eq. (2.53). By knowing the rotational velocity vector, the time derivative of the rotation matrix can be calculated. In the numerical simulation tool HPS the derivative is calculated in a different manner. The derivative at time t is calculated as the difference of the rotation matrices at the times $t - \Delta t$ and $t + \Delta t$ divided by the time interval:

$$\dot{\mathbf{R}}\left(t\right) = \frac{\mathbf{R}\left(t + \Delta t\right) - \mathbf{R}\left(t - \Delta t\right)}{2\Delta t}. \tag{2.59}$$

The following coordinate transformations can be performed by a combination of the above described methods.

2.3.5.1 ICRF - HCI

The transformation between the ICRF and the HCI is done with both the translational and rotational transformation described above. As stated in Sections 2.3.1 and 2.3.4 the origin of the first is at the SSB whereas the second is located at the centre of the Sun. Their principal plane differs as well because the ICRF is located in the equatorial plane of J2000.0 and the HCI lies in the ecliptic of the same epoch.
In the trajectory simulations performed in this thesis, the trajectory is described in the HCI but the JPL ephemeris are generated in the ICRF [33]. For the calculation of the third-body perturbations the position of the planets

need to be transformed to the HCI frame. The first step is the translational correction by subtracting the Sun's position in the ICRF from the position of planet i:

$$\boldsymbol{r}_i^{S,equ} = \boldsymbol{r}_i^{ICRF} - \boldsymbol{r}_{Sun}^{ICRF}. \tag{2.60}$$

After the translational correction the position of planet i is expressed with respect to the Sun and equatorial plane. This vector needs to be rotated into the ecliptic. The angle between those two planes is changing over time as stated in Section 2.3.4 and can be expressed as a function of time [28, p. 15]:

$$\varepsilon = 23.4392911^\circ - 46.8150''T - 0.00059''T^2 + 0.001813''T^3. \tag{2.61}$$

This relation is expressed with respect to the epoch of J2000.0 and T describes the time in Julian centuries since this epoch,

$$T = \frac{JD - 2451545}{36525}, \tag{2.62}$$

where JD is a date in Julian days, 2451545 is the Julian date of J2000.0 and 36525 is the number of days in a Julian century. Independent of the simulation duration, the obliquity of ecliptic and equatorial plane can be taken as 23.4392911° because both frames are defined at J2000.0 and assumed inertial. The x-axes of both frames are parallel, therefore the rotation matrix can be expressed as,

$$\mathbf{R}_x(\varepsilon) = \begin{bmatrix} 1 & 0 & 0 \\ 0 & \cos(\varepsilon) & \sin(\varepsilon) \\ 0 & -\sin(\varepsilon) & \cos(\varepsilon) \end{bmatrix}, \tag{2.63}$$

and describes the rotation from equatorial plane to ecliptic [28, p. 14]:

$$\boldsymbol{r}_i^{HCI} = \mathbf{R}_x(\varepsilon)\, \boldsymbol{r}_i^{S,equ}. \tag{2.64}$$

2.3.5.2 HCI - ECI

This transformation incorporates the same procedures as the one just described in Section 2.3.5.1. The translational correction moves the point of reference from the centre of the Sun to the centre of Earth and the rotational correction is the inverse rotation mentioned above. This transformation is used to calculate the position of the spacecraft with respect to Earth for the gravitational acceleration of Earth, and post-simulation analysis. For the analysis, not only the position vector but also the SC's velocity with respect to Earth is of interest. Therefore, the transformation of position and velocity

is described.
First, the translational correction of position and velocity in the ecliptic plane,

$$\boldsymbol{r}_{SC}^{E,ecl} = \boldsymbol{r}_{SC}^{HCI} - \boldsymbol{r}_{Earth}^{HCI}, \tag{2.65}$$

where the difference of the SC's and Earth's position vector in the heliocentric frame yields the position of the SC with respect to Earth and to the ecliptic plane. The same calculation for the velocity reads as follows:

$$\boldsymbol{v}_{SC}^{E,ecl} = \boldsymbol{v}_{SC}^{HCI} - \boldsymbol{v}_{Earth}^{HCI}. \tag{2.66}$$

Then, the rotation to the equatorial plane is done with the transpose of Eq. (2.63):

$$\mathbf{R}_x^T(\varepsilon) = \begin{bmatrix} 1 & 0 & 0 \\ 0 & \cos(\varepsilon) & -\sin(\varepsilon) \\ 0 & \sin(\varepsilon) & \cos(\varepsilon) \end{bmatrix}, \tag{2.67}$$

$$\boldsymbol{r}_{SC}^{ECI} = \mathbf{R}_x^T(\varepsilon)\, \boldsymbol{r}_{SC}^{E,ecl}. \tag{2.68}$$

The rotational transformation of the velocity vector reads as follows:

$$\boldsymbol{v}_{SC}^{ECI} = \mathbf{R}_x^T(\varepsilon)\, \boldsymbol{v}_{SC}^{E,ecl}, \tag{2.69}$$

which is derived from Eq. (2.53), with the velocity and position vectors $\boldsymbol{v}_{SC}^{E,ecl}$, $\boldsymbol{r}_{SC}^{E,ecl}$, the rotation matrix $\mathbf{R}_x^T(\varepsilon)$ and its time derivative $\dot{\mathbf{R}}_x^T(\varepsilon)$. The latter is equal to zero as the two frames are assumed inertial. Also the frames are defined at the epoch J2000.0 and therefore the same value of obliquity as in Section 2.3.5.1 can be used for $\mathbf{R}_x^T(\varepsilon)$.

2.3.5.3 ECI - ECEF

The transformation between the ECEF or ITRF and the ECI or GCRS is the most complex one. Their origin is at the same position at Earth's centre of mass, but their orientation changes constantly. In the IERS Convention 2010 [23] the relation between both frames is described as the superposition of the following motions, which can be expressed as time dependent rotation matrices:

$\mathbf{W}(t)$	Polar motion of Celestial Intermediate Pole (CIP)
$\mathbf{R}(t)$	Rotation of Earth around the axis of CIP
$\mathbf{Q}(t)$	Celestial motion of the CIP due to precession and nutation

Each rotation matrix is the combination of a series of rotations about the axes x, y and z of the corresponding intermediate frames:

$$\begin{aligned} \mathbf{W}(t) &= \mathbf{R}_z(-s')\,\mathbf{R}_y(x_p)\,\mathbf{R}_x(y_p), \\ \mathbf{R}(t) &= \mathbf{R}_z(ERA), \\ \mathbf{Q}(t) &= \mathbf{R}_z(-E)\,\mathbf{R}_y(-d)\,\mathbf{R}_z(E)\,\mathbf{R}(s). \end{aligned} \tag{2.70}$$

The description of the meaning and complex calculations of the six parameters are beyond the scope of this thesis and can be looked up in the IERS Convention 2010 [23, p. 43-78]. Combining the three rotation matrices yields the transformation from ECI to ECEF as follows:

$$\begin{aligned} \boldsymbol{r}_{SC}^{ECEF} &= \mathbf{Q}(t)\,\mathbf{R}(t)\,\mathbf{W}(t)\,\boldsymbol{r}_{SC}^{ECI}, \\ \boldsymbol{r}_{SC}^{ECEF} &= \mathbf{T}(t)\,\boldsymbol{r}_{SC}^{ECI}. \end{aligned} \tag{2.71}$$

As the ECEF is not an inertial frame and the transformation changes with time, the transformation for the velocity of the spacecraft incorporates the complete Eq. (2.53):

$$\boldsymbol{v}_{SC}^{ECEF} = \mathbf{T}(t)\,\boldsymbol{v}_{SC}^{ECI} + \dot{\mathbf{T}}(t)\,\boldsymbol{r}_{SC}^{ECI}. \tag{2.72}$$

A particularity is the rotation of an acceleration vector. The spherical harmonics Earth potential field model needs the position of the spacecraft not only with respect to the centre of Earth but with respect to a particular orientation of Earth, therefore the gravitational acceleration is calculated in the ECEF. The numerical integration however works with states in the ECI or HCI, which leads to the necessity of the transformation of acceleration vectors. For this, one needs to understand that there are two different type of vectors [34, p. 18]. The position vector is a bound vector because it describes a physical property that is dependent on a specific point in space and a relocation would alter its impact. A free vector is a vector which can be relocated, as long as its magnitude, orientation and sense of direction stay the same, without changing its impact. The velocity vector is a free vector. Similar to position or force, the acceleration is a bound vector. So instead of differentiating Eq. (2.53) with respect to time, one can use the same transformation as for the position vector. For the transformation from ECEF to ECI it reads as follows:

$$\boldsymbol{a}^{ECI} = \mathbf{T}^T(t)\,\boldsymbol{a}^{ECEF}. \tag{2.73}$$

Chapter 3

State of the Art

Gravity assists are used since as early as 1959, when the Russian probe Luna 3 used this kind of manoeuvre to take pictures of the far side of the Moon [35]. The physics behind this technique were explained in the previous chapter. Beyond that, an unknown effect causes a different trajectory for Earth-gravity assist than predicted. An overview of the scientific research regarding this Flyby Anomaly is given to classify this master thesis with the subject matter. Then, the current state of the art of gravity-assist and interplanetary-mission simulation is outlined.

3.1 Research of the Flyby Anomaly

A few month after the Near Earth Asteroid Rendezvous (NEAR) spacecraft's encounter with Earth in 1998, Antreasian and Guinn [2] published the first paper about an anomalous velocity change in the ranging and tracking data. They point out that the detected discrepancy of incoming and outgoing velocity of the spacecraft could point to a trajectory modelling error, an unknown perturbation or a non-fulfilment of Newtonian gravity. In their paper they concentrate on the gravity field of Earth as a possible source for the anomaly of the Galileo and NEAR spacecrafts. More precisely, possible errors in the spherical harmonic representation, as the effect through Earth's oblateness is orders of magnitude greater than every non-gravitational acceleration. The use of the most recent Joint Gravity Model (JGM-3) [17] with order and degree of 30 could not account for the observed frequency shifts. Also, including hypothetical values for the J, C and S terms of up to order and degree 10 for the estimated gravity field could produce results that explain the frequency shift.
In association with the reconstruction of the spacecraft Juno's Earth-gravity

assist (EGA), Thompson et al. [36] found a truncation of Earth's gravity model to be able to produce similar velocity results to the observed anomaly. Higher order/degree fields (100x100, 50x50, 20x20) were compared to the standard field used for launch operations of 10x10. This resulted in the discovery of a perturbation of several mm/s when using a 50x50 field, as well as the sensitivity of the trajectory to fields higher than 100x100 [36]. This endorses the work of Antreasian and Guinn and illustrates the importance of using a high order gravity field in the orbit propagation. Regarding the mentioned lessons learned, the HPS is a well suited tool for the analysis of the space-environmental influences on interplanetary trajectories. A spherical harmonics model of up to order and degree 360 including multiple tide models is incorporated in the HPS, as already described in Section 2.1.1.1.
In 2006, Lämmerzahl et al. [16] published a paper discussing a collection of unexplained phenomena within the Solar system. At that time, additionally to Galileo's two and NEAR's single flyby, five more gravity assists at Earth were tracked. Trajectory data for three spacecraft were available and for two, Cassini and Rosetta, an anomaly was detected. They argue that the small number of reliable and precise data sets is too low to draw any conclusion on a cause. Instead, they give a first order estimate of the impact of various environmental effects. Due to the order of magnitude of the perturbing acceleration, Lämmerzahl et al. rule out the atmosphere, ocean- and solid-Earth tides, charging of the spacecraft, magnetic torques, Earth's albedo as well as solar winds as single sources of the anomaly. It should be noted that they regard every perturbation individually and calculate with representative but notional values for mass, area and velocity. [16]
Jouannic et al. [37] investigated the topic by adapting the empirical formula of Anderson [1] based on correlations of the anomaly and flyby parameters. Additionally, it has to be mentioned that three dimensional models of spacecraft were used in the orbit propagation.
Jouannic et al. try to compute a velocity difference at perigee Δv_p of similar value to the observed anomaly with the help of National Aeronautics and Space Administration's (NASA) GEODYN II software and investigate the sensitivity of the problem to different parameters. The velocity difference at perigee is of interest, as the anomaly can be described through an impulsive manoeuvre near perigee, where for example NEAR and Galileo could not be tracked [2]. To obtain the difference in the velocity at perigee, two spacecraft states are propagated. One from the entry in the Sphere of Influence forward in time towards perigee and one from exit of the SoI backward in time towards perigee. The calculated velocity difference is not necessarily identical to the observed value, but through repeated orbit propagation with slightly changed trajectory and model parameters, a sensitivity to those parameters

can be calculated. The following parameters were varied: spacecraft attitude, spacecraft-drag coefficient (C_D), solar-radiation-pressure-scaling coefficient (C_R) and material specular and diffuse reflectivity coefficient (ρ_s, ρ_d). The C_R coefficient allows to adjust the acceleration due to the radiation pressure in case of modelling errors of mass, surface area, etc.
For the calculation of the atmospheric-drag and radiation-pressure accelerations, a three-dimensional spacecraft model can be used in the GEODYN software. This gives more accurate results, than calculating with notional values of areas or mass. The spacecraft is 3D-modelled in a simplified way with a number of two-dimensional panels. Specular and diffuse reflectivity coefficient are assigned to every panel particular to its material. A sensitivity analysis for every parameter was conducted, yielding the necessary change of the parameter to account for the observed anomaly. Regarding this study, atmospheric drag and planetary radiation pressure were discarded because of the low sensitivity (high variation of the coefficient necessary) and an overall small impact (minor acceleration) on the trajectory, respectively. However, Jouannic et al. detected a high sensitivity with respect to the solar radiation pressure which shows that a small modelling error of a few percent could account for the observed anomaly. Especially variations (inside a small range of 10^{-4} to $4 \cdot 10^{-2}$) of the reflectivity coefficients, which are not known at the time of flyby but only estimated, can account for the anomalous velocity change. [37]

3.2 Simulation of Interplanetary Trajectories and Gravity Assists

In this section, the methods used in other simulation tools for the propagation of interplanetary trajectories and calculation of gravity assists are outlines. A summary of tools used by space agencies and recommendations found in literature is presented. These tools numerically integrate the equations of motion to generate the flight path of a spacecraft.
Scientists at NASA have developed several simulation tools over the years. Many were developed for mission design and early stage trajectory calculation. This includes finding possible launch dates as well as optimizing fuel consumption and flight time [38]. One of these tools is the General Mission Analysis Tool (GMAT), which has many of the dynamics modelling in common with the other tools described in this section. The dynamics of all tools include the following terms [38, 39, 40]:

- n-body point mass gravity
- non-spherical Earth potential field
- atmospheric drag
- solar radiation pressure
- relativistic corrections

It is important to note that the GMAT also incorporates models for satellite thrust and the relativistic correction terms can be used if the integration is computed in reference frames located at celestial-body centres. An exception is the centre of the Sun. For heliocentric trajectories the relativistic correction is omitted from the calculation [38, p. 94].
For the determination of the influences on trajectories and comparison of the results to past flown missions, optimization is of little interest. Therefore, the optimization possibilities are neglected here and only two additional orbit determination tools are examined for the classification of the HPS adaptions.
NASA's Double-Precision Orbit Determination Program (DPODP) is around since the 1960's and was the benchmark for orbit determination tools most of this time. DPODP uses several acceleration terms to numerically integrate the spacecraft ephemeris with double precision [39, p. 1]. Double precision is a floating point format defined by the Institute of Electrical and Electronics Engineers (IEEE) and is able to represent numbers using 8 bytes of storage. 52 bits are used to store 16 significant decimal digits, which defines the precision of the stored number. The exponent of the number is stored in 11 bits making it possible to store numbers between 2^{-1022} and 2^{1023} in binary representation. At last, one bit is used for the sign storage. [41] Additionally to the terms above, the equations of motion are extended by motor burns and other small forces originating in the spacecraft, such as attitude control and gas leaks [39, p. 30ff.]. The centre of integration can be located in the centre of mass of the Sun, the nine planets or the moon. It can be defined at one position for the whole calculation duration or it can be switched if the spacecraft enters the Sphere of Influence of a celestial body [39, p. 30].
The software used by Jouannic et al. [37] is called GEODYN. Also developed at NASA, GEODYN is a set of software tools able to determine orbits around Earth based on initial parameters and to compute theoretical tracking data using geodetic parameters based on the orbit [40]. The equations of motion can only be integrated in geocentric rectangular reference frames and include tidal potential, Earth radiation and thermal drag effect on Laser Geodynamics Satellite (LAGEOS) in addition to the previously named terms [42, p. 119ff.].
Kemble [15] describes the physics and special techniques of interplanetary missions and gravity assists as well as its optimization demand and use in

missions to planets. He describes three different approaches for modelling gravity-assist manoeuvres. The most accurate is identified as the numerical integration of the three-body problem. The spacecraft states are analysed at simulation start and end position, where the gravitational influence of the gravity-assist body is negligible, to calculate the effect of the manoeuvre [15, p. 219f.].
The other two are versions of patched conics method which derive the entry states relative to the gravity-assist body from the previous conic-section trajectory. With the period of the hyperbola calculated from orbital parameters the states at exit can be calculated. The exit and entry states are then evaluated to calculate the velocity change. This method is a good approximation in which errors arise from the assumption of conic-section trajectories and negligence of perturbations. [15, p. 220f.] The second conic method calculates the gravity assist under assumption of an instantaneous event as the instantaneous change in direction and velocity through hyperbolic asymptotic velocities [15, p. 221f.].
If planetary encounters are included in interplanetary-trajectory design their duration is often assumed negligible in comparison to the whole mission duration. This is done in combination with the optimization problem of finding suitable trajectories to reduce computational cost and enable optimization [43, 44, 45]. Therefore, gravity-assist evaluations are reduced to its geometrical and theoretical description.
As stated before, the calculation of gravity assists and the associated interplanetary trajectories are best done by numerical integration according to Kemble [15]. In the beginning of this section the options provided by established simulation tools were reported. The HPS can be lined up with these tools, as it includes most of the dynamics models and centre of integration options. A more detailed overview of its capabilities is given in the next chapter.

Chapter 4

High Performance Satellite Dynamics Simulator

The High Performance Satellite Dynamics Simulator is a simulation tool using the MATLAB and Simulink user interface for the modelling and analysis of scientific missions in Earth orbits. All functions are stored in bibliography files and can be integrated in Simulink to build a simulation model. The main function is the *Dynamics Core*, which is coded in C/C++, compiled to a .mex file and can be utilized by Simulink function blocks. The *Dynamics Core* computes the dynamics of a satellite orbiting Earth and can be extended with several other functions in a Simulink model. For example, with an attitude controller or external perturbations. For the setup of simulations a MATLAB file with initial parameters must be defined. [6]
This chapter focuses on the abilities of the HPS, especially on the particularities concerning the dynamics and perturbation models described in Chapter 2, like extensions to the spherical harmonics potential field and the incorporation of a finite-element model.

4.1 Dynamics

In Section 2.1.1.1 two descriptions of Earth's potential field are characterized. One is spherical symmetric and one is dependent on both longitude and latitude. The first is a simplification, can be calculated up to degree six and therefore needs less computational power than the latter, which can be calculated up to order and degree 360.
The HPS is a simulation tool to support modelling and data analysis of scientific missions [6]. These scientific missions are exclusively in Earth orbits and therefore the equations of motion are integrated in an Earth-centred inertial

reference frame, the GCRF (ECI).
In addition to the ECI in Section 2.3.2, a second Earth-centred reference frame is described in Section 2.3.3, the ECEF. The position of the satellite in the ECI is used for the spherical symmetric potential field as well as the acceleration due to other celestial bodies calculated with Eq. (2.20). Every body in the following list can be individually selected depending on the necessity for the simulation:

- the Sun
- Mercury
- Venus
- Mars
- Jupiter
- Saturn
- Uranus
- Neptune
- Pluto
- the Moon

Due to the dependency on latitude and longitude of the second description of the potential field, the position in the ECEF is needed for the calculation. According to Eq. 2.10, the potential is described as the sum over degree and order containing sine/cosine terms, Legendre polynomials $\bar{P}_{lm}$ and Stokes' coefficients $\bar{C}_{lm}$, $\bar{S}_{lm}$. The spherical harmonic coefficients are determined from satellite data only or a combination of satellite, terrestrial and marine measurements and define static models of Earth's potential field. An overview of available models and corresponding data is available at the ICGEM website [10].

4.1.1 Earth Tides

In addition to the static components of the potential field, temporal factors can be included in the HPS as well. These effects are solid-Earth tides, ocean tides and solid-Earth and ocean-pole tides induced by the Sun and the Moon [23, p.79 ff.]. The gravitational influence of the two bodies leads to an elastic deformation of Earth, whose amplitude and phase can be measured. The deformation is governed by complex and little known laws because of Earth's physical properties [46]. The Coriolis force, caused by Earth's ellipticity and rotation, yields tidal deformations called solid-Earth tides. The ocean tides describe the variation in the potential field due to tidal waves of the oceans caused by the influence of the Sun and the Moon. The ocean tide models include tidal waves with different periods, from some hours (quarter-diurnal wave) to several years (long period waves). The pole tides are caused by the centrifugal effect of the polar motion of Earth. [23, p. 79ff.]
In contrast to the coefficients of the static model of Earth's potential field the terms describing the tides are time dependent due to the varying rela-

tive positions of the Sun, Earth and the Moon, the rotation of Earth, its ellipticity and liquid core. For convenience the influence of the tides is modelled as variations of the tide-free static geopotential coefficients C_{lm}, S_{lm} [23, p. 79ff.].
Based on the model, the tides complement the static geopotential up to varying order and degree. The solid-Earth tides can be calculated with a minimum of order two and a maximum of four. Additionally, it can be selected between an elastic and an anelastic model. The latter includes anelastic behaviour of Earth's crust in the computation of the coefficient variations, which introduces imaginary parts [23, p. 79ff]. For the ocean and pole tides the order can be chosen arbitrarily. Due to the fact that the effect of the tides is orders of magnitude smaller than the static geopotential, choosing an order greater than the static order has negligible impact and should be avoided to save computational resources. For example, the coefficient $C_{20,stat}$, which has a value of -0.484·10^{-3}, is varied by the permanent tidal deformation as follows [47]:

$$C_{20} = C_{20,stat} - 4.173 \cdot 10^{-9}. \tag{4.1}$$

In the HPS the Stokes's coefficients used in the calculation of Earth's gravitational acceleration are calculated according to:

$$\begin{aligned} C_{lm} &= C_{lm,stat} + \Delta C_{lm,sEt} + \Delta C_{lm,ot} + \Delta C_{lm,pt}, \\ S_{lm} &= S_{lm,stat} + \Delta S_{lm,sEt} + \Delta S_{lm,ot} + \Delta S_{lm,pt}. \end{aligned} \tag{4.2}$$

Whereas static coefficients $C_{lm,stat}$ are taken from model files provided by the ICGEM, the Δ terms have to be calculated from parameters describing the different tide models. A detailed description of the calculations can be found in the IERS Technical Note 36 [23].
The tidal effects are orders of magnitude smaller than the static geopotential and therefore need to be evaluated if the inclusion in the simulation of interplanetary trajectories is required or not. The impact on the simulated trajectories is described and evaluated in Chapter 7.

4.2 Perturbation Models

The theory behind the non-gravitational perturbations is listed in Chapter 2. The focus in this section lies on the implementation of those models in the HPS, for which the utilization of a 3D FE model is of importance.

4.2.1 3D Finite Element Model

Using an FE program (e.g. Analysis System (ANSYS)) the geometry of any spacecraft can be generated with arbitrary precision in a global coordinate system. For this master thesis a model of Rosetta is used in a simplified manner containing the structures of the bus, two solar panels and the high-gain antenna (HGA), as these are the most prominent structures of the spacecraft. Smaller parts like the beams connecting the solar arrays to the bus are omitted which can be seen in Figure 4.1. The axes in the lower right corner represent the orientation of Ansys' global frame and indicate the orientation of the FE model.

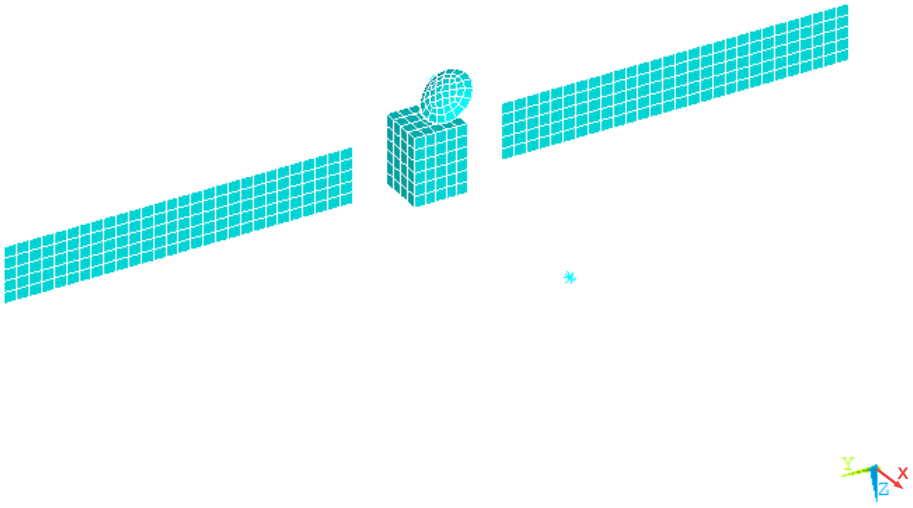

Figure 4.1: *Finite Element model of Rosetta*

After construction of the spacecraft geometry the different bodies are meshed by means of finite elements. The elements are of both volume and surface type, but for the HPS the surface elements representing the exterior surfaces of the spacecraft are critical. Each exterior surface is partitioned in a certain number of quadrangular elements. The number of elements is defined by the desired element size. Each quadrangular shell element is defined by four nodes, one at each corner of the element as pictured in Figure 4.2, and has a unique identification number (ID). The orientation of the element, namely the orientation of its normal vector $\boldsymbol{n}$ is defined by the crossproduct of the vectors between three nodes, $\overline{ij}$ and $\overline{ik}$, where i, j and k are also unique

identification numbers. [48] For the preprocessing in the HPS the normal vector of every element has to point outwards [47].

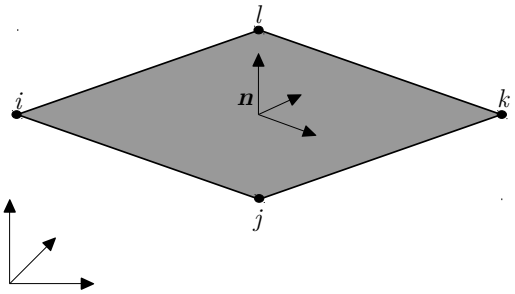

Figure 4.2: *Definition of shell element*

By defining materials in the FE tool and assigning them to the elements, the elements are able to represent the physical behaviour of the spacecraft parts. Customary material properties are the density or mechanical properties like the Young modulus. The mechanical properties of every element make it possible to calculate the CoM of the satellite model. The position of the CoM is used as the origin of the body-fixed frame. Additionally, for the analysis of the non-gravitational perturbations the radiation surface properties are important as they define how incoming radiation affects the spacecraft. Therefore, dedicated absorption, reflection and emission coefficients are assigned to every surface element. The coefficients for the Rosetta model used in this master thesis are listed in Table 4.1.

Table 4.1: *Surface radiation properties absorptivity, emission and reflectivity for the infrared and visible electromagnetic range based on [8, p. 386, 49].*

Part	**Visible**			**Infrared**		
	α / ε	ρ_s	ρ_d	α / ε	ρ_s	ρ_d
bus	0.86	0.14	0.00	0.93	0.07	0.00
solar panel	0.65	0.05	0.30	0.81	0.03	0.16
high gain antenna	0.80	0.20	0.00	0.80	0.20	0.00

According to Kirchoff's law [8, p. 381] the emission and absorption ability is equal at a given wavelength λ:

$$\alpha(\lambda) = \varepsilon(\lambda). \tag{4.3}$$

Therefore, emissivity and absorption coefficients are given in the same column for one range of the electromagnetic spectrum. Nevertheless, the emissivity and absorptivity varies dependent on the wavelength. The wavelength of maximum radiance of a body depends on its temperature and is defined by Wien's displacement law. The higher the temperature of the radiating body, the shorter the wavelength at maximum radiance as pictured in Figure 4.3 [50, p. 256].

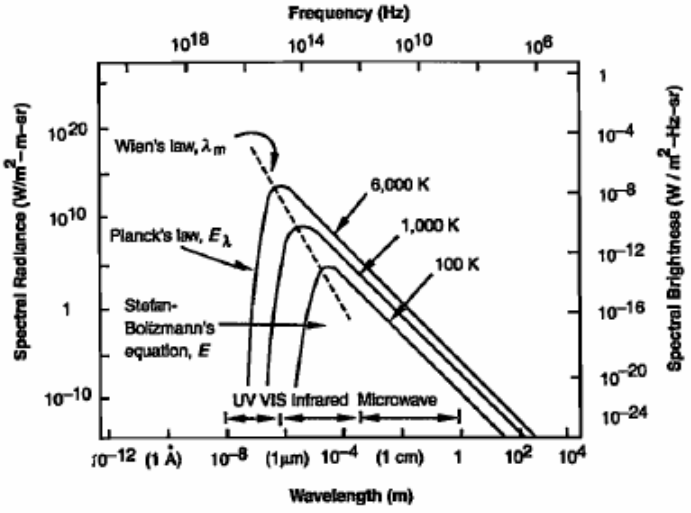

Figure 4.3: *The black body radiation curve [50, p. 256]*

Considering the different radiation sources, it yields that depending on their temperature the incident radiation on the spacecraft is in different wavelength domains. For the Sun, most of its radiation is in the visible range of the electro-magnetic spectrum which yields that albedo radiation is in the same range, as it is simply reflected at Earth's surface. According to its name, Earth infrared radiation is in the infrared domain due to Earth's low temperature. Therefore, the radiation surface properties have to be defined in two ranges, leading to the generation of two data files. One holds the properties for the visible domain and is used for the calculation of solar radiation pressure and Earth albedo. The second holds infrared coefficients and is used in the Earth-infrared and spacecraft-thermal-radiation-pressure calculations.
This concludes the definition of the spacecraft in the FE tool and the important information needed by the HPS are exported as text files. One file containing nodal information, one for the elements and two for the surface

properties. According to the HPS Design Document [6] the tables contain the data provided in Tables 4.2 to 4.4.

Table 4.2: *Contents of element table*

Column	Content
1	element ID
2	element area
3	x-coordinate of the centre point in global coordinate system
4	y-coordinate of the centre point in global coordinate system
5	z-coordinate of the centre point in global coordinate system
6	node ID 1
7	node ID 2
8	node ID 3
9	node ID 4

Table 4.3: *Contents of node table*

Column	Content
1	x-coordinate in global coordinate system
2	y-coordinate in global coordinate system
3	z-coordinate in global coordinate system

Table 4.4: *Contents of radiation surface coefficient tables*

Column	Content
1	absorption coefficient
2	emission coefficient
3	specular reflectivity coefficient
4	diffuse reflectivity coefficient

4.2.2 Preprocessing

The four tables, the position of the model's barycentre in the global coordinate system and information about an incident vector $\boldsymbol{e}_{in}^{b}$, by means of polar coordinates (θ, φ), are used in a preprocessing step in the HPS. The

preprocessing is done to create look-up tables containing reference area, separate tables for each Cartesian component of a normalized force, normalized torque and pressure-point vectors for all polar coordinate combinations. The polar coordinates, which can be defined in arbitrary resolution for θ from 0 to π and φ from 0 to 2π, are stored in text files as well. Defined in the prior mentioned range and in the satellite body frame according to Figure 4.4 every direction can be represented.

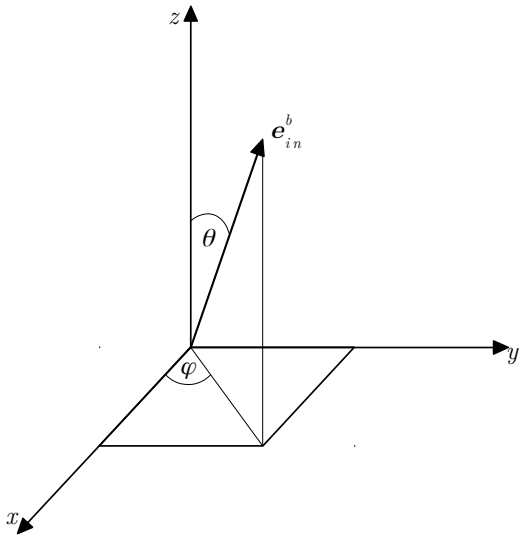

Figure 4.4: *Definition of polar angle θ and azimuth angle φ in the body-fixed frame.*

The reference area is computed as the exposed area projected perpendicular to the incident vector $\boldsymbol{e}^b_{in}$. For this, the normal vector of every element is compared to the incident vector. If the angle between both is greater than 90° it means that the element is on the backside, seen from the perturbation source, and does not contribute to the perturbation. In a second step, it is determined if a potentially exposed element is shadowed by another element. The mathematical description of the procedure exceeds the scope of this thesis and can be found in the HPS Design Document [6]. The reference area is calculated as follows, with n being the number of exposed and non-shadowed surface elements of the spacecraft model [6, p. 223]:

$$A_{ref} = \sum_{i=1}^{n} |A_i \cdot \boldsymbol{n}^b_i \cdot \boldsymbol{e}^b_{in}|. \tag{4.4}$$

Then, the pressure point of a force acting on the exposed surface can be calculated with the position of each incident element $\boldsymbol{r}_i^b$ in the body-fixed frame:

$$\boldsymbol{r}_l^b = \sum_{i=1}^{n} \frac{A_{ref,i}\boldsymbol{r}_i^b}{A_{ref}}. \tag{4.5}$$

The normalized force vector $\boldsymbol{f}_i^b$ in the body-fixed frame can be calculated for every incident element i depending on the radiation surface properties as follows [6, p. 231]:

$$\boldsymbol{f}_i^b = -A_i \left[(1-\rho_s)\, \boldsymbol{e}_{in}^b + 2\left(\rho_s \cos(\alpha) + \frac{1}{3}\rho_d\right) \boldsymbol{n}_i^b \right] \cos(\alpha)\, f_{sh,i}. \tag{4.6}$$

Here, ρ_s and ρ_d describe the specular and diffuse reflection coefficients, the incident vector $\boldsymbol{e}_{in}^b$ characterizes the unit position vector of the perturbation source with respect to the spacecraft in the body-fixed frame and $\boldsymbol{n}_i$ is the normal vector of element i. The angle between both vectors is denoted with α and A_i stands for the element size of element i, which is taken from the element table. $f_{sh,i}$ is a binary factor indicating if an element i is shadowed by another element or not. By adding all normalized element force vectors the normalized force vector acting on the spacecraft is calculated:

$$\boldsymbol{f}^b = \sum_{i=1}^{N} \boldsymbol{f}_i^b. \tag{4.7}$$

Here, N denoted the total number of elements of the spacecraft model. Eq. (4.6) and (4.7) are computed for every combination of θ and φ and stored in three text files; one for each Cartesian coordinate. Through cross multiplication of the normalized force vector and the position vector of element i in the body-fixed frame, the normalized torque vector due to a perturbation can be calculated:

$$\boldsymbol{t}^b = \sum_{i=1}^{N} \boldsymbol{r}_i^b \times \boldsymbol{f}_i^b. \tag{4.8}$$

The preprocessing algorithm yields a precise indication of the perturbation magnitude depending on the attitude of the spacecraft. The effect of different attitudes on the influence of the perturbations on the trajectory is described in detail in Chapter 7.
All non-gravitational perturbations described in the following sections are calculated in the body-fixed frame located at the spacecraft's centre of mass.

In the Simulink models of the HPS all perturbations are calculated as force terms and passed to the dynamics core. There, the vectors are divided by the spacecraft mass and transformed to an inertial frame used for the numerical integration of the equations of motion.

4.2.3 Atmospheric Drag

The atmospheric drag uses a fairly simple computation scheme. The normalized relative velocity vector $\hat{\boldsymbol{v}}_{rel}^{b}$ represented in the body-fixed frame is used as the incident vector for this perturbation and defines the reference area A_{ref}. According to the polar and azimuth representation of $\hat{\boldsymbol{v}}_{rel}^{b}$ the dedicated reference area is selected from the look-up table and inserted in Eq. (2.22). The remaining variables are defined according to the description in Section 2.1.2.2.

4.2.4 Solar Radiation Pressure

For the calculation of acceleration due to the solar radiation pressure, the look-up tables with normalized force components are essential. By multiplying the total normalized force vector $\boldsymbol{f}^{b}$ with the solar radiation pressure the total force vector is computed:

$$\boldsymbol{f}_{SRP}^{b} = p_{SR}\boldsymbol{f}^{b}. \tag{4.9}$$

By expanding Eq. (4.9) with the eclipse condition I and the spacecraft mass m, the acceleration due to the solar radiation pressure is calculated according to Eq. (2.25):

$$\boldsymbol{a}_{SRP}^{b} = \frac{I\boldsymbol{f}_{SRP}^{b}}{m}. \tag{4.10}$$

The radiation pressure coefficient C_R in Eq. (2.25) is calculated in Eq. (4.6) by the terms in the square brackets.

4.2.5 Earth Albedo and Infrared

The calculation of the acceleration due to Earth albedo and infrared utilizes the following algorithm. Look-up tables for the normalized force components calculated with Eq. (4.6) can be used here as well. The difference is that the incident vector $\boldsymbol{e}_{in}^{b}$ is here taken as the unit vector from Earth-surface segment $\mathrm{d}A_j$ to spacecraft-surface element A_i. In Eq. (2.29) the total flux of segment $\mathrm{d}A_j$ due to Earth albedo and infrared and intersected by a surface

of area A_c is defined. When the flux is not projected onto an interception area, Eq. (2.29) changes in the following way:

$$\mathrm{d}\Phi_{tot,j} = \left(\rho S \cos\left(\theta_S\right) + \varepsilon M_B\right) \frac{1}{\pi r^2} \mathrm{d}A_j. \tag{4.11}$$

The HPS calculates the albedo power radiated per segment $\mathrm{d}A$ according to its term

$$\mathrm{d}\Phi_{Alb,j} = \rho S \cos\left(\theta_S\right) \frac{1}{\pi r^2} \mathrm{d}A_j, \tag{4.12}$$

taking the reflection coefficient ρ from the CERES data tables for every segment $\mathrm{d}A_j$. The IR power is not calculated by its term

$$\mathrm{d}\Phi_{IR,j} = \varepsilon M_B \frac{1}{\pi r^2} \mathrm{d}A_j, \tag{4.13}$$

but is more directly provided by CERES in tables of the power per unit area $\mathrm{d}q_{IR,j}$ for every segment $\mathrm{d}A_j$ [18]. Therefore, the power per unit area only has to be multiplied by the area $\mathrm{d}A_j$:

$$\mathrm{d}\Phi_{IR,j} = \mathrm{d}q_{IR,j} \mathrm{d}A_j. \tag{4.14}$$

The total acceleration can then be computed by combining Eq. (4.11) divided by the speed of light c and Eq. (4.6) and summing over both the number of Earth segments M in the field of view of the spacecraft and all elements N of the spacecraft:

$$\boldsymbol{f}^b_{Alb,IR} = \sum_{j=1}^{M} \sum_{i=1}^{N} \frac{\mathrm{d}\Phi_{tot,j}}{c} \boldsymbol{f}^b_{i,j}. \tag{4.15}$$

As the angle between incident vector and element normal vector is regarded in the normalized force preprocessing calculations, only elements whose normal vector and LoS vector from spacecraft to segment $\mathrm{d}A_j$ span a angle smaller than 90° and are not shadowed add a part to the total force. Through the division by the spacecraft mass m, the acceleration acting on the spacecraft in the body-fixed frame is obtained.

4.2.6 Thermal Radiation Pressure

As stated in Section 2.1.2.5, the acceleration due to the thermal radiation of the spacecraft is dependent on the surface temperature that results from incoming and self-generated heat. Assuming, that the spacecraft does not

generate heat, solar radiation, Earth albedo and infrared are the remaining heat sources. The thermal radiation pressure algorithm also uses look-up table generated in the preprocessing step. A three-dimensional table holding the factor Λ_i is applied to the incident solar radiation flux to convert the scalar value to a vector containing the absorbed flux for each illuminated element. Λ_i describes the absorption coefficient based on incident vector, normal vector and shadowing condition for every element i:

$$\Lambda_i = \alpha_i f_{sh,i} \boldsymbol{e}_{in}^b \boldsymbol{n}_i^b. \tag{4.16}$$

The albedo and infrared flux is already being computed per incident element in the albedo and IR function.
Regarding Eq. (2.33) the acceleration is governed by the surface temperature according to the Stefan-Boltzmann law. The temperature of the surface can be calculated by different models [18]. For the simulations in this master thesis, a static description was chosen.
In the static model an instantaneous heating/cooling and no heat conduction through the material is assumed. Therefore, the radiated power per element is equal to the absorbed radiation:

$$Q_{out,i} = \Lambda_i Q_{in,i}. \tag{4.17}$$

According to Eq. (2.32), the surface temperature is equal to:

$$T_i = \left(\frac{Q_{out,i}}{\varepsilon_i \sigma} \right)^{\frac{1}{4}}. \tag{4.18}$$

The surface temperature of the element i is inserted in Eq. (2.33) and by summing over all elements N the total acceleration is computed:

$$\boldsymbol{a}_{TRP} = \sum_{i=1}^{N} \boldsymbol{a}_{TRP,i}. \tag{4.19}$$

4.3 Setup

For the realisation of a simulation with the HPS one has to build a model in Simulink and define the simulation parameters in the *initial_parameters.m* MATLAB file. An example model including atmospheric drag and an attitude controller can be seen in Figure A.1.
The central block *Dynamics Core* is the main function of the HPS. In this block, the gravitational acceleration due to the celestial bodies is calculated

and the spacecraft states are numerically integrated. Depending on the other blocks in the model, *Drag* and *Satellite Attitude Control*, the perturbation and control torques and forces are added to the states for the integration.
The simulation parameters from *initial_parameters.m* can be allocated in three groups. The *core parameters* define which option for mandatory functions and which additional optional functions are used during the simulation. Belonging in this group are the parameter listed in Table A.1, which is located in the Appendix due to its extensive size.
The second group defines initial parameters of the trajectory. Its members can be found in Table 4.5. The parameter *frame* defines if the initial position and velocity vector are given in the ECI or ECEF frame. Depending on this a transformation to the ECI is performed because the integration frame is always the inertial ECI. The parameter *states* includes initial values for the rotation velocity, attitude, velocity and position. If the term states or initial states is used in this master thesis at later points, only velocity and position are regarded. The initial rotational velocity and the attitude are omitted as they are not relevant for the described calculations or evaluations.

Table 4.5: *Elements of initial parameters*

Parameter	**Value**
frame	ECI ECEF
states	rotational velocity $\boldsymbol{\omega}_b$ attitude $\boldsymbol{q}_b$ velocity $\boldsymbol{v}_{SC}$ position $\boldsymbol{r}_{SC}$

The last group contains further spacecraft parameters and file paths as well as variables that are needed for the calculations outside of the *Dynamics Core*. Depending on the additional functions that are included in the Simulink model, the parameters of this group vary. In Table 4.6 example parameters for the model in Figure A.1 are given.

Table 4.6: *Elements of additional parameters*

Parameter	**Value**
initial external torques	in inertial frame in orbit frame in mechanical frame
initial external torques	in inertial frame in orbit frame in mechanical frame
spacecraft-mass properties	mass inertia tensor position of mechanical with respect to the body-fixed frame
target attitude	quaternion defined by flight path angle
attitude controller	control parameter $\boldsymbol{C}$ control parameter $\boldsymbol{K}$
Earth rotation	vector $\boldsymbol{\omega}_E$
drag coefficient	C_D
look-up tables	angles θ and φ pressure point reference area
atmosphere	model coefficients

In the following chapter, the customization of the HPS is explained. Afterwards, the changes to the simulation tool are evaluated with a series of a simulations. Based on the results, further adaptations to the code are made and it is decided if the modifications are working correctly or not. The evaluation process is pictured in Figure 4.5.

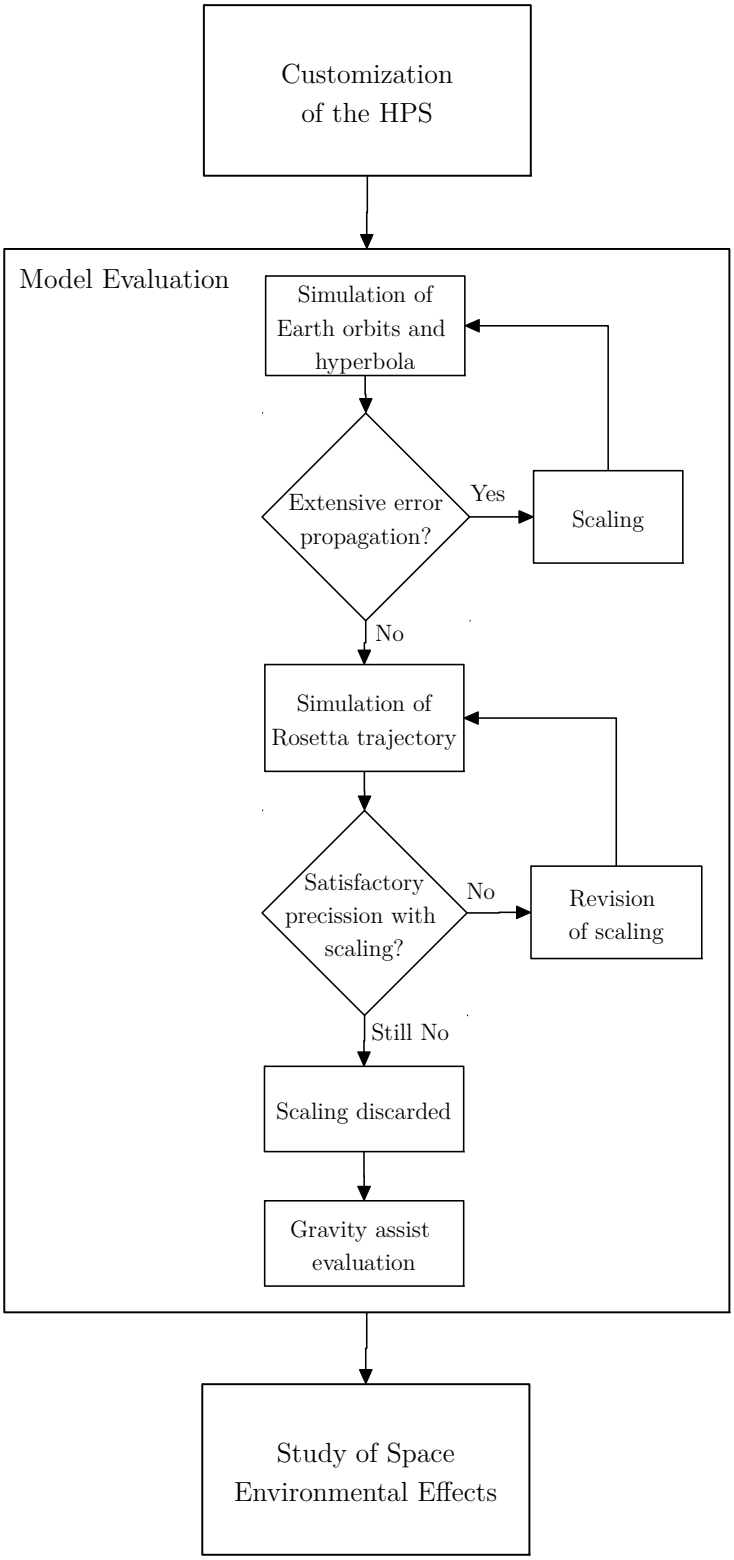

Figure 4.5: *The procedure of the evaluation of the HPS modifications. This is done after the customization and before the actual study.*

Chapter 5

Customization of the HPS

In this chapter, the changes made to the HPS source code are described in the way of how the code was adapted to enable the simulation of interplanetary trajectories.

5.1 Option for Interplanetary Trajectories

As stated by Kemble [15, p. 219f.] a gravity assist or any other interplanetary trajectory is most accurately simulated in a heliocentric system by integrating the equations of motion of the three-body system (see Eq. (2.14)). This leads to the necessity of introducing a third celestial coordinate frame in which spacecraft states can be defined and calculated. In addition to the Earth-centred ECI and ECEF, the Sun-centred HCI is chosen. To enable the HCI as a frame for the initial spacecraft-position and velocity vectors, the author added a third option for the initial parameter *frame*. Furthermore, a new initial parameter was defined which is called *mission*. This parameter defines the type of mission to be simulated as either planetocentric (1) or heliocentric (2). According to *mission* the integration frame is either the ECI or HCI, respectively. The determination process of the necessary coordinate transformations depending on *frame* and *mission* is depicted in Figure 5.1. Without the definition of a reference frame, the input for the initial states has no physical meaning. In Figure 5.1 references to the corresponding sections for the transformations in Chapter 2 are made.

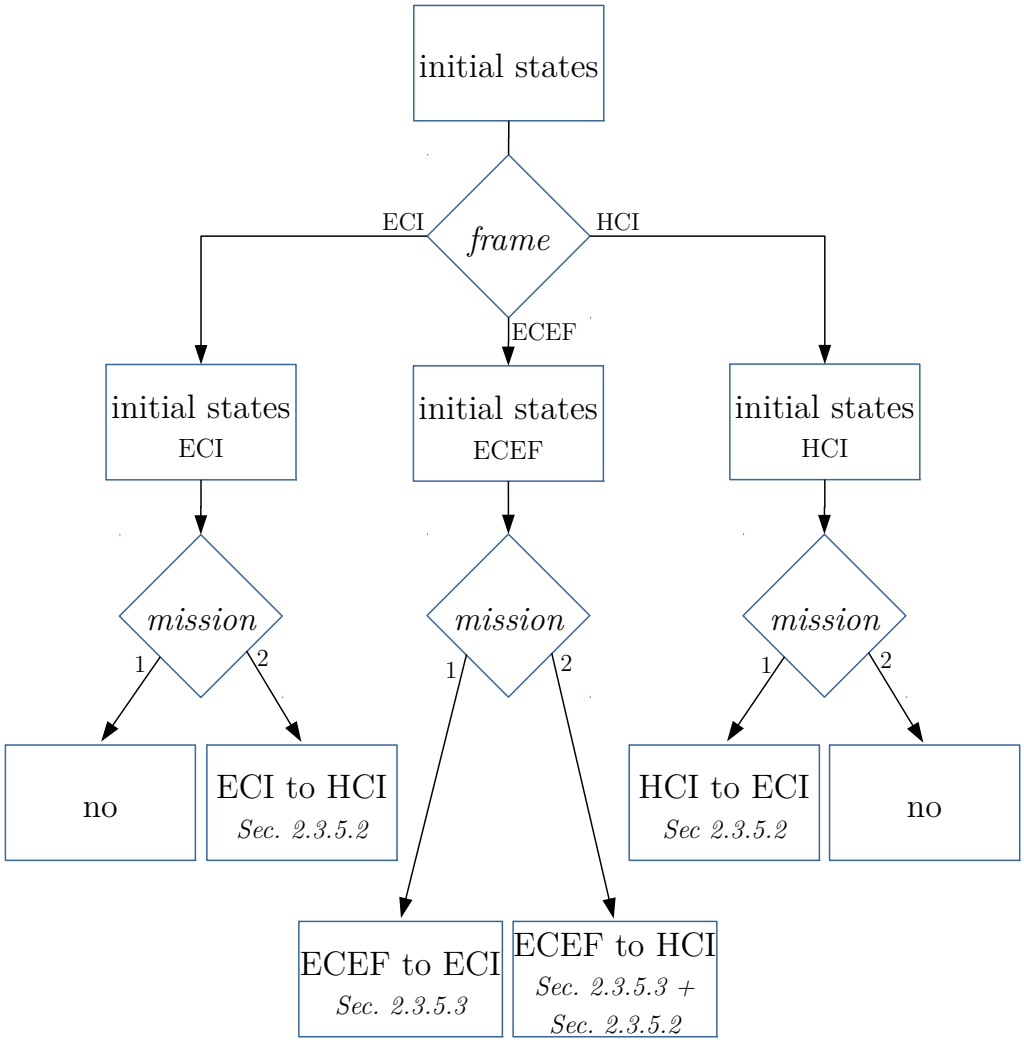

Figure 5.1: *Determination process of necessary coordinate transformations based on initial parameters*

5.2 Earth Ephemeris

These coordinate transformations introduce the aspect that now the origin of the frame may change its position. The velocity and position of Earth are needed for the transformations and have to be calculated as part of the ephemeris routine of the HPS. In Table A.1, four different ephemeris models are listed: the analytical Montenbruck method and three different models from JPL. The three JPL models are calculated with the same method, only the underlying parameters are based on different observation data and orbit

determination models [33]. In the analytical Montenbruck model the position and velocity of all major celestial bodies are calculated either in the ECI or the HCI. Only the position is defined as an output of this function. Therefore, only the addition of the velocity to the output was done by the author.
The JPL Development/Lunar Ephemeris (DE) provide numerically integrated position and velocity of all major bodies as well as the solar-system and Earth-Moon barycentres [33]. The models are available for download at a NASA server, including binary data files containing Chebychev polynomial coefficients for all three Cartesian components of the position vector and necessary subroutines. Chebychev polynomials are used for the approximation of polynomial functions due to its fast convergence and high accuracy. There are several kinds of Chebychev polynomials, but only the first kind, $T_n(s)$, is used here [51]:

$$T_n(\cos(\theta)) = \cos(n\theta) \qquad \text{for} \qquad s = \cos(\theta). \tag{5.1}$$

An important property of the polynomials is the recursive relationship. At a particular point a polynomial can be expressed by its neighbouring polynomials as follows [51]:

$$T_{n+1}(s) = 2sT_n(s) - T_{n-1}(s), \tag{5.2}$$

which yields the first three polynomials in combination with Eq. (5.1):

$$\begin{aligned} T_0(s) &= 1, \\ T_1(s) &= s, \\ T_2(s) &= 2s^2 - 1. \end{aligned} \tag{5.3}$$

In the case of the planetary ephemeris, the equations of motion are approximated with the Chebychev coefficients in 32-day-long segments and depending on the body further divided into intervals. The coefficients can be converted to rectangular position and velocity vectors. However, in the HPS only position vectors are generated from the coefficients and therefore the introduction of the velocity conversion process by the author was necessary. The application of Chebychev polynomials for the approximation of a function $f_i(s)$ reads as follows [51]:

$$f_i(s) \approx P_{i,N}(s) = \sum_{n=0}^{N} C_{i,n} T_n(s). \tag{5.4}$$

Here, $C_{i,n}$ stands for a Chebychev coefficient provided in the JPL DE file and N denotes the number of Chebychev coefficients, leading to the necessity of computing just as many polynomials $T_n(s)$. The function $f_i(s)$, defined by the coefficients in the JPL DE file, describes one cartesian component i of the orbital position of a body depending on s. Consequently, the approximation has to be done individually for i equal to x, y and z to generate the position vector. The variable s in Eq. (5.4) is the date of evaluation in a subinterval of the 32-day segment as a number between -1 and 1:

$$s = \frac{2\left(JD - JD_{start}\right)}{t_{int}} - 1. \tag{5.5}$$

JD is the time at which the ephemeris is calculated and JD_{start} the start date of the interval, both in Julian days. The duration in days which the intervalls spans is denoted with t_{int}.
For the calculation of the velocity the function $f(s)$ has to be derived with respect to s:

$$f_i'(s) \approx P_{i,N}'(s) = \sum_{n=0}^{N} C_{i,n} T_n'(s). \tag{5.6}$$

This equation uses the derivatives of the Chebychev polynomials, which are calculated with from of Eq. (5.2) as follows:

$$T_{n+1}'(s) = 2T_n(s) + 2sT_n'(s) - T_{n-1}'(s). \tag{5.7}$$

The first three derivatives are:

$$\begin{aligned} T_0'(s) &= 0, \\ T_1'(s) &= 1, \\ T_2'(s) &= 4s. \end{aligned} \tag{5.8}$$

One important circumstance about the JPL ephemeris has to be noted. The unit of the received velocity vector is kilometre per interval duration in days and has to be transformed to metre per second for further use.
The code for the implementation of the velocity calculation of the planets is based on the example found at [52]. Due to the source being a private website, the results were compared on a sample basis to the ephemeris generated at the JPL Horizons website [53]. The results of Earth's position and velocity vary by a maximum of 0.35 m and 22.8 m/s from the Horizons data. For the position, the deviation can be expressed as $2 \cdot 10^{-8}$ % of the distance of Earth and the Sun. And also the velocity differs no more than 0.08 % from the Horizons-Earth's velocity, which was both ruled acceptable by the author.

5.3 Gravitational Accelerations

The main purpose of the HPS is the simulation of Earth orbits, as stated before. This means that Earth is the central body for all simulations and the gravitational potential of Earth is the most influential acceleration acting on the spacecraft. During an interplanetary trajectory the spacecraft is on an orbit around the Sun instead. Therefore, the gravitational potential of the Sun is most important and always needs to be calculated. For this reason, if *mission* is set to 2 (interplanetary) in the *initial_parameters.m* file the option for the acceleration on the spacecraft due to the Sun is turned on and cannot be deselected.

5.3.1 Earth

In this master thesis, interplanetary trajectories coming close to Earth are simulated. Instead of changing Earth's acceleration to a perturbation, for which it can be decided if it is calculated or not, the acceleration is always computed as well. Here, an inquiry is included in the code by the author, which sets the gravity field model to the simple one (see Eq. (2.12)) if the spacecraft is outside of Earth's Sphere of Influence. This is done because the more precise model of the inhomogeneous potential field does not have a significant impact at the distance of the SoI and the Sun has a greater influence on the spacecraft. A comparison between the accelerations due to the Sun and Earth over the distance to Earth is shown in Figure 5.2. The depicted trajectory is an example hyperbola around Earth with a periapsis at 5000 km altitude over Earth's surface. It can be seen that for the most part of the trajectory the Sun exerts a higher acceleration on the spacecraft. Only at distances below ca. $2.5 \cdot 10^5$ km (roughly 2/3 of the Earth-Moon distance) Earth's influence is higher. Outside the Sphere of Influence the magnitude of Earth's acceleration is of order 10^{-4} m/s^2 and one order of magnitude smaller than the Sun's acceleration.
The precision loss due to the usage of the simple model is therefore insignificant. Additionally, it also decreases the computational effort and simulation time. Inside the SoI, the user can decide which model is applied according to the options in Table A.1.
The spacecraft states are of heliocentric nature in an interplanetary-trajectory simulation but the *GravityField* function needs the spacecraft position in a planetocentric coordinate frame for the Earth-gravity calculation. Therefore, the author added coordinate transformations according to Section 2.3.5.2 and 2.3.5.3. Consequently, the heliocentric position and velocity vectors are transformed to ECI or ECEF at every time step this acceleration is calcu-

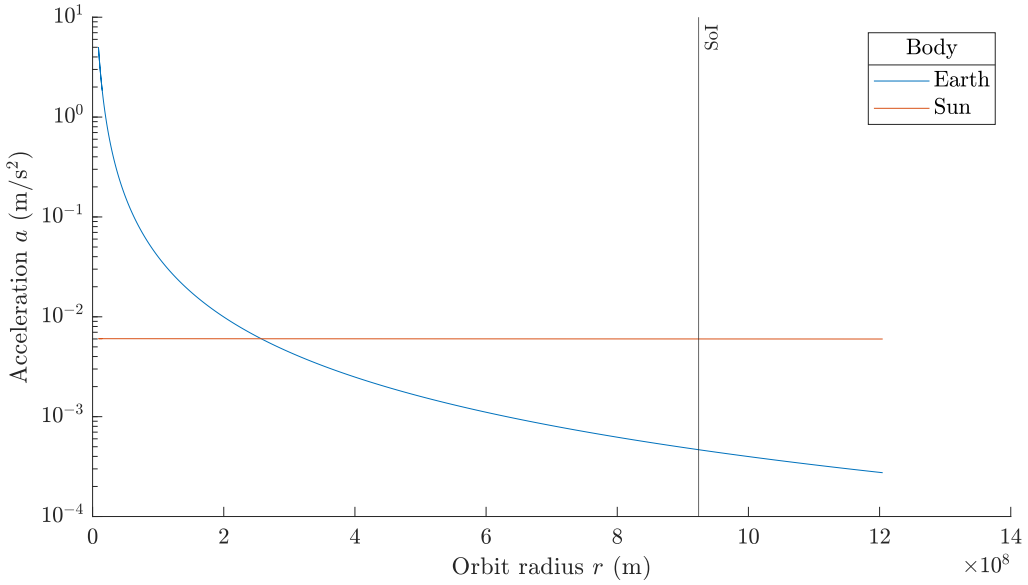

Figure 5.2: *Acceleration caused by Earth and the Sun during a hyperbola around Earth plotted over the distance to Earth.*

lated. The received acceleration vector is then represented in the equatorial plane. The orientation for a heliocentric integration has to be corrected with respect to the ecliptic plane with the rotation around the aligned x-axis of both systems described in Section 2.3.5.2, as depicted in Figure 5.3, so that the acceleration vector points to the origin of the frame in both representations:

$$\boldsymbol{a}_E^{ECI} = \mathbf{T}^T(t)\,\boldsymbol{a}_E^{ECEF} \quad \text{(optional; only if SHM)}, \tag{5.9}$$

$$\boldsymbol{a}_E^{E,ecl} = \mathbf{R}_x \boldsymbol{a}_E^{ECI}. \tag{5.10}$$

The second frame in Figure 5.3 is denoted *ecliptic* instead of HCI because its origin is still at Earth's centre of mass. As the acceleration vector originates in the spacecraft and points towards the gravitational body, the point of origin of the coordinate frame is not important. Only the orientation of the frames has to be regarded and therefore, no translational transformation for the acceleration vector has to be done between the ECI and HCI.

5.3.2 Third Bodies

The third-body perturbations are directly calculated in the HCI. For this, Eq. (2.20) is used with the heliocentric positions of both the spacecraft and the third body. In the n-body system with the Sun as the central body, the

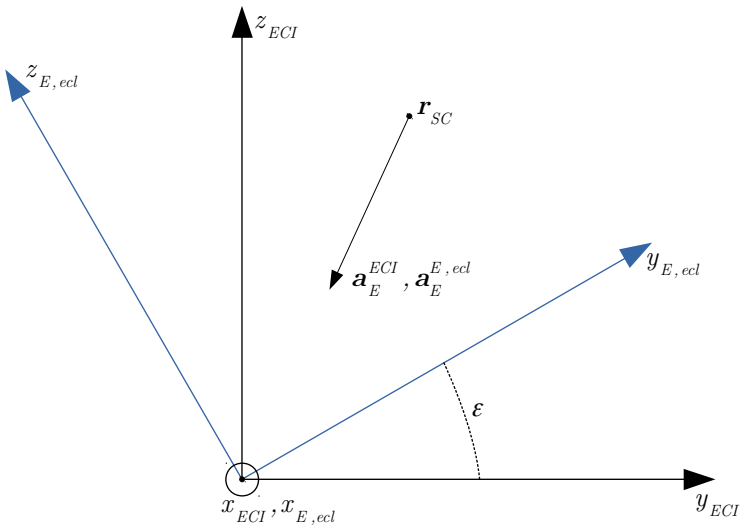

Figure 5.3: *The orientation of the acceleration vector in the ECI and ecliptic frame.*

perturbation due to Earth would also be calculated with Eq. (2.20). But due to the structure of the HPS and the more precise calculation of Earth's gravity, the terms added to the Earth gravity model to compose the complete three-body model are a variation of Eq. (2.20):

$$\boldsymbol{p}_{3rd} = -\mu_S \frac{\boldsymbol{r}_{SC}^{HCI}}{r_{SC}^{HCI\,3}} - \mu_E \frac{\boldsymbol{r}_E^{HCI}}{r_E^{HCI\,3}}. \tag{5.11}$$

The second term in this equation together with the acceleration calculated from the gravity field of Earth make up the perturbation term due to Earth according to Eq. (2.20).

5.4 Additional Outputs

For the validation of the implemented code and the analysis of simulated trajectories, additional outputs were defined. Firstly, the velocity vector of the Sun in the ECI was added to the ephemeris output. If this vector and the position of the Sun from the ephemeris are multiplied with -1, they represent the Earth states in a heliocentric equatorial frame. This was necessary for the evaluation of the ephemeris calculation with the Chebychev polynomials. Second, a dedicated output for the spacecraft states in the ECI was defined. In the HPS the spacecraft states are output to the MATLAB interface in the frame of integration. Which means that for interplanetary missions only

heliocentric spacecraft states would be accessible for further analyses. By adding an output with ECI states, the coordinate transformation feature of the code can be utilized and does not have to be done again in the MATLAB interface.
At last, the third-body perturbation vectors are defined as an output to analyse the impact of each selectable body on the trajectory. The frame in which the accelerations are described is dependent on the mission. For a planetocentric mission the frame is the ECI and for a interplanetary mission the frame is the HCI.
The ECI states and accelerations are incorporated as new parameters in the *core parameters* group of the *initial_parameters.m* file. Therefore, the user can decide if the output is necessary or desired.

Chapter 6

Model Evaluation

In this chapter, the evaluation of the customization of the HPS is covered. Through the analysis of the following simulations it is evaluated if the integration of the three-body model provides plausible results and if special techniques like the gravity assist can be accurately reproduced. Due to the obtained results improvements to the code and simulation setup are proposed.

6.1 Earth Orbit

To check if the integration in the heliocentric frame produces plausible results, exemplary Earth orbits are simulated with the adapted HPS, called New HPS (NHPS), in both heliocentric and planetocentric setups. The planetocentric setup in the NHPS is equal to the original HPS, therefore an evaluation of the new simulation routine can be performed. The main difference between the two simulations is the consideration of Earth's orbit around the Sun. In the HPS a two-body model is used to describe the orbit of the spacecraft, whereas in the NHPS the complete three-body model. The analyses are conducted to examine if the NHPS can calculate the orbit around a moving Earth with satisfactory accuracy with respect to the orbit obtained from the HPS.
In Figure 6.1 one exemplary orbit is pictured. The orbit is a low-Earth orbit (LEO) with the parameters listed in Table 6.1 and simulated for one revolution around Earth. The left figure shows the top-view of the orbit with the line of sight in negative z-direction. On the right side, a side view of the orbit is pictured with the LoS in negative x-direction.
Additionally to the orbit defined in Table 6.1, orbits with differing inclination and eccentricity are simulated to analyse their effect on the difference between both simulations. Even though the orbit plots in Figure 6.1 align really well

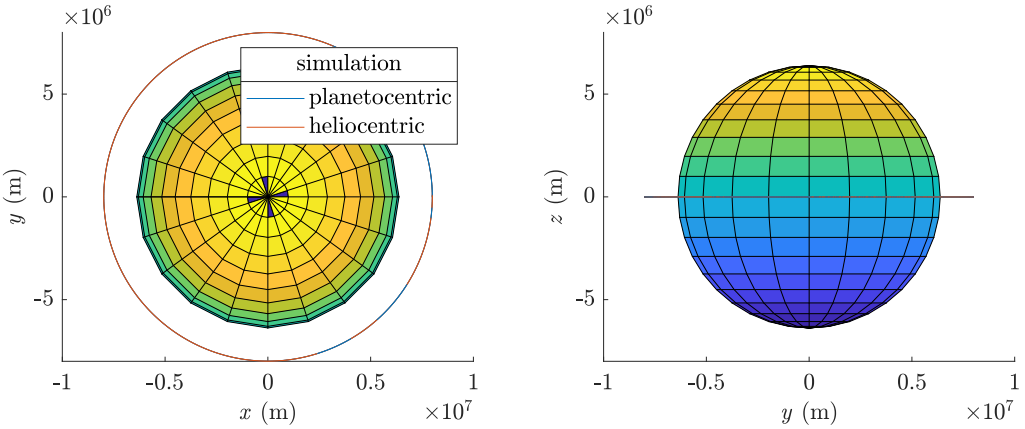

(a) *LoS along -z-axis* **(b)** *LoS along -x-axis*

Figure 6.1: *Plot of an example orbit around Earth. Once simulated in the planetocentric and once in the heliocentric frame.*

and no difference is visible, the position difference is in the kilometre range. The position difference is calculated as follows and its progression over the simulation duration is pictured in Figure 6.2:

$$\begin{aligned} \Delta \boldsymbol{r}\,(t) &= \boldsymbol{r}^{ECI}_{NHPS}\,(t) - \boldsymbol{r}^{ECI}_{HPS}\,(t)\,, \\ \Delta r\,(t) &= |\Delta \boldsymbol{r}\,(t)\,| = \sqrt{\Delta x\,(t)^2 + \Delta y\,(t)^2 + \Delta z\,(t)^2}. \end{aligned} \tag{6.1}$$

Here, $\boldsymbol{r}^{ECI}_{NHPS}\,(t)$ and $\boldsymbol{r}^{ECI}_{HPS}\,(t)$ represent the ECI-spacecraft position at time t from the NHPS and HPS simulation, respectively. The superscript is dropped because the difference is analysed only in the ECI. The progression shows that the difference is not periodically and increases the longer the orbit is simulated. It is also visible that the major position difference is in the xy-plane as these components have greater values than the z-direction.

The maximum position difference occurs at the last time step of the simulation and has a value of 1036.6 m. For the orbits with different eccentricity and inclinations the maximum varies about $\pm$ 600 m (see Table 6.2). The simulation with increasing eccentricity were conducted for the orbit with 20° inclination because for this inclination the highest position difference for $e = 0$ is detected. With higher eccentricity the difference of the NHPS and HPS simulations increases as well. For an eccentricity of 0.1 the difference increases by about 50 %. Expressed as a relative value related to the euclidean norm of the position vector ($\approx a$) the maximum Δr is 0.02 %.

Table 6.1: *Definition of Low-Earth orbit and initial SC position in terms of Keplerian elements.*

Element	Value
eccentricity e	0
semi-major axis a	8000000 m
inclination i	0°
longitude of ascending node Ω	0°
argument of periapsis ω	0°
true anomaly ν	0°

6.1.1 Evaluation

Increasing the inclination revealed a dependency of the difference between both simulations on the inclination of the orbit. Based on the results a variation of sine or cosine dependency is plausible. Due to the shape of Earth and the mass accumulation around the equator the difference increases at first because an increasing acceleration in z-direction follows the higher inclination. At some point the difference decreases again because the increase of the z-direction acceleration is countered by a decrease in the acceleration in x and y-direction.
The influence of the eccentricity cannot be analysed precisely because the simulation time increases for orbits with higher eccentricity due to the increasing orbital period. The higher difference could therefore be a result of the longer simulation time instead of the increasing eccentricity.
According to the results of these analyses, the simulation scheme of the NHPS can be approved for Earth orbits according to the negligible 0.02 % difference. The influence of the motion of Earth, which is not considered in the two-body model of the HPS, is correctly described by the NHPS and the orbits simulated with both tools match adequately. Nevertheless, due to the progression of the difference during one orbit and its increase in simulations of orbits with higher eccentricity, the difference in simulations of high-eccentric-hyperbolic orbits ($e > 1$) with long simulation times of more than one day is predicted to be too large. It is thought to improve the HPS simulation scheme with the function presented in the following section.

Table 6.2: *Maximum position difference after one revolution for various orbit simulations.*

Orbit	**max. Δr(m)**
$i = 0\,^\circ, e = 0$	1036.6
$i = 20\,^\circ, e = 0$	1045.4
$i = 20\,^\circ, e = 0.01$	1087.9
$i = 20\,^\circ, e = 0.02$	1135.8
$i = 20\,^\circ, e = 0.05$	1289.4
$i = 20\,^\circ, e = 0.1$	1605.8
$i = 45\,^\circ, e = 0$	1039.2
$i = 60\,^\circ, e = 0$	1026.5

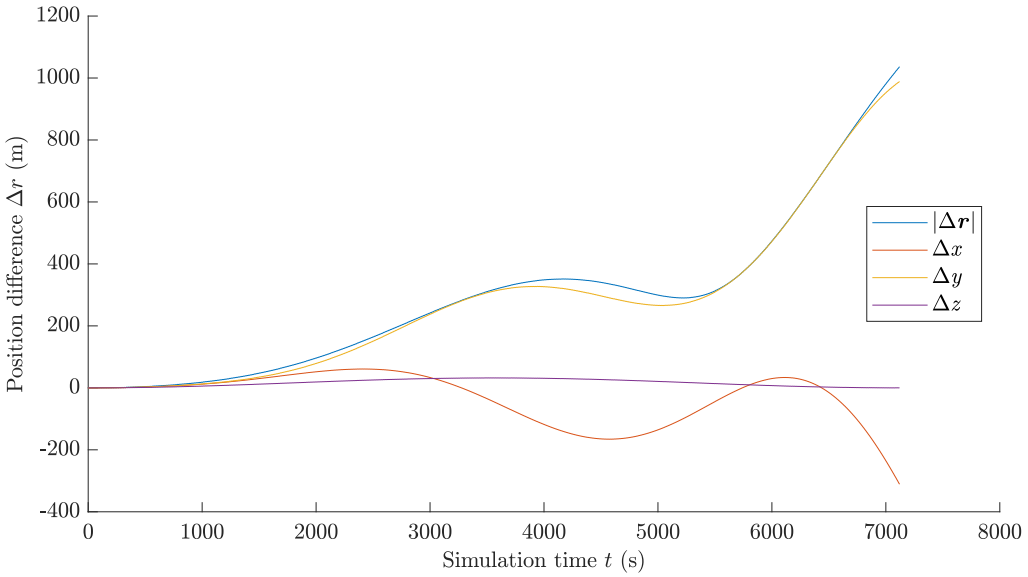

Figure 6.2: *The position difference of the heliocentric to the planetocentric simulation of an Earth orbit plotted over time. Dedicated graphs for each vector component and the euclidean vector norm are pictured.*

6.2 Scaling

In floating point arithmetic errors are inevitable. A real number cannot be exactly represented by a finite number of bits. Therefore, every number is approximately represented in binary system. Another rounding error is introduced by arithmetic computations. [54] Due to this effect, numerical errors introduced by multiplications, divisions, additions or subtractions of very different (OoM difference) or similar numbers can propagate rapidly. This is identified as the main cause of the position difference between the NHPS and HPS simulation in the way the difference progresses.
During one integration loop Earth's position with respect to the Sun and the spacecraft position with respect to Earth are added and subtracted from each other. The order of magnitude these numbers differ can be higher than 10^{11} if one component of the spacecraft-position vector is in the sub-metre range. Also in the integration scheme the heliocentric position is multiplied with numbers as small as 0.01. To reduce the order of magnitude the numbers differ a scaling algorithm was developed, which is described in this section.
The implementation of the scaling function is done with an additional initial parameter. The parameter *scale* is added to the *core parameters* with two options. If 0 is selected the simulation stays unscaled, with 1 the scaling is activated. Similar to the selection of the more complex gravity model, the scaling is also implemented only inside the Sphere of Influence.
To decrease the difference, the size of the solar system is scaled with a factor to the base ten. Mostly, this method is applied to the Earth-state vectors but also to the acceleration vectors due to the celestial bodies as later described in this section. By scaling the Earth-position vector and keeping the original SC position with respect to Earth, the former and the latter have the same order of magnitude. The velocity vector of Earth is scaled with the same factor according to the linear dependency between the two physical properties.
To determine the value of the scale factor the Earth-Sun and spacecraft-Earth distances are compared. If the exponent of the two values is not equal, the scale factor is defined by the difference of the two exponents:

$$\begin{aligned} E_{exp} &= \lfloor \log_{10}\left(r_E^{HCI}\right) \rfloor, \\ SC_{exp} &= \lfloor \log_{10}\left(r_{SC}^{ECI}\right) \rfloor, \end{aligned} \tag{6.2}$$

$$f_{s1} = 1 \cdot 10^{E_{exp} - SC_{exp}}. \tag{6.3}$$

The exponent of both distances is extracted by the floor function of the logarithmic representation of the respective distances. The floor function rounds a real value x to the greatest integer smaller than or equal to x. If the exponents E_{exp} and SC_{exp} are found to be 11 and 8, respectively the scale factor f_{s1} calculates to 1000. The scale factor is then applied to the Earth-position and velocity vector:

$$\begin{aligned} \boldsymbol{r}_{E,s}^{HCI} &= \frac{\boldsymbol{r}_{E}^{HCI}}{f_{s1}}, \\ \boldsymbol{v}_{E,s}^{HCI} &= \frac{\boldsymbol{v}_{E}^{HCI}}{f_{s1}}. \end{aligned} \tag{6.4}$$

With these scaled vectors the scaled heliocentric spacecraft states are calculated, which are then used for the integration of the trajectory:

$$\begin{aligned} \boldsymbol{r}_{SC,s}^{HCI} &= \boldsymbol{r}_{SC}^{E,ecl} + \boldsymbol{r}_{E,s}^{HCI}, \\ \boldsymbol{v}_{SC,s}^{HCI} &= \boldsymbol{v}_{SC}^{E,ecl} + \boldsymbol{v}_{E,s}^{HCI}. \end{aligned} \tag{6.5}$$

The superscript E, ecl denotes the position and velocity vectors in an auxiliary frame which is located at the centre of Earth and its xy-plane is in the ecliptic. By simple subtraction of the scaled Earth position and rotation to a desription with respect to the equatorial plane (according to Section 2.3.5.2), the unscaled ECI-spacecraft position necessary for the Earth-gravity calculation is obtained. For the calculation of the third-body accelerations the heliocentric position is needed (see Eq. (2.20)). The scaled vector cannot be used because it is composed of a scaled and an unscaled part and this inconsistency would lead to wrong results. Therefore the unscaled position vector is reconstruced as follows:

$$\boldsymbol{r}_{SC}^{HCI} = \boldsymbol{r}_{SC,s}^{HCI} - \boldsymbol{r}_{E,s}^{HCI} + \boldsymbol{r}_{E}^{HCI}. \tag{6.6}$$

For the integration, the acceleration needs to be in the same state as the velocity. Earth's part of the velocity vector is scaled with f_{s1}, therefore the third-body acceleration needs to be scaled as well:

$$\boldsymbol{p}_{3rd,s} = \frac{\boldsymbol{p}_{3rd}}{f_{s1}}. \tag{6.7}$$

The velocity of the spacecraft around Earth is unscaled therefore the Earth-gravity vector is not scaled. The sum of the scaled and unscaled accelerations reads as follows:

$$\boldsymbol{a}_{tot} = \boldsymbol{a}_{E} + \sum_{i=1}^{n} \boldsymbol{p}_{3rd,s}. \tag{6.8}$$

After the integration, the new position vector is split into an Earth-centred-spacecraft and a heliocentric-Earth position. These two vectors are compared to calculate a new scale factor according to Eq. (6.2) and (6.3). If the new scale factor f_{s2} is not equal to f_{s1} the Earth states are scaled with the new scale factor according to Eq. (6.4) and the heliocentric spacecraft-position and velocity vectors are rescaled as follows:

$$\begin{aligned} \boldsymbol{r}_{SC,s}^{HCI} &= \boldsymbol{r}_{SC,s}^{HCI} - \boldsymbol{r}_{E,s1}^{HCI} + \boldsymbol{r}_{E,s2}^{HCI}, \\ \boldsymbol{v}_{SC,s}^{HCI} &= \boldsymbol{v}_{SC,s}^{HCI} - \boldsymbol{v}_{E,s1}^{HCI} + \boldsymbol{v}_{E,s2}^{HCI}. \end{aligned} \tag{6.9}$$

The potentially rescaled spacecraft states are used in the next integration loop and the scaling algorithm is performed at every simulation time step. The example orbits from Table 6.1 are simulated again with the scale option turned on. It can be seen in Table 6.3 that the position difference could be reduced by five OoM. As a result of the scaling the maximum relative-position difference could be reduced to $2{\cdot}10^{-7}\,\%$. The progression of the difference is pictured in Figure 6.3 and it can be seen that it has the same shape as for the unscaled simulation.

Table 6.3: *Maximum position difference after one revolution for various scaled orbit simulations.*

Orbit	**max. Δr (m)**
$i = 0\,^\circ, e = 0$	$1.04{\cdot}10^{-2}$
$i = 20\,^\circ, e = 0$	$1.05{\cdot}10^{-2}$
$i = 20\,^\circ, e = 0.01$	$1.09{\cdot}10^{-2}$
$i = 20\,^\circ, e = 0.02$	$1.14{\cdot}10^{-2}$
$i = 20\,^\circ, e = 0.05$	$1.29{\cdot}10^{-2}$
$i = 20\,^\circ, e = 0.1$	$1.6{\cdot}10^{-2}$
$i = 45\,^\circ, e = 0$	$1.04{\cdot}10^{-2}$
$i = 60\,^\circ, e = 0$	$1.03{\cdot}10^{-2}$

Additionally to the Earth orbits, an exemplary interplanetary trajectory is compared in unscaled and scaled state. The orbit-defining Kepler elements are listed in Table 6.4. In Figure 6.5 the trajectories of both the scaled and unscaled simulations are plotted. Without scaling, the trajectory simulated with the NHPS turns in negative z-direction and separates visibly from the HPS simulation. The difference increases in negative direction for all three vector components after the periapsis. The scaled simulation does not display

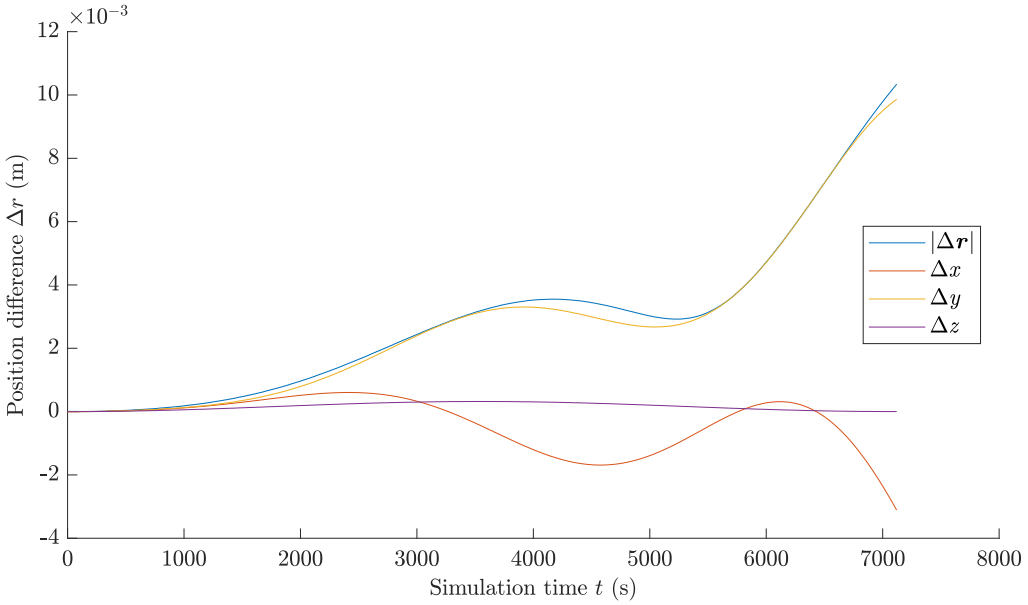

Figure 6.3: *The position difference of the scaled heliocentric to the planetocentric simulation of an Earth orbit plotted over time. Dedicated graphs for each vector component and the euclidean vector norm are pictured.*

this behaviour and the difference is reduced from $5.16{\cdot}10^6$ m to $2.86{\cdot}10^3$ m. Expressed as percentages of the spacecraft-Earth distance the differences read as 0.9 % and $5.0{\cdot}10^{-4}$ %. Comparing the progression of both differences (see Figure 6.4) the spacecraft still turns in negative z-direction in the scaled NHPS simulation but to a lesser degree. Due to the scaling the difference in the x and y-direction is increasing in the positive direction. Overall the difference is reduced by three orders of magnitude. The maximum difference is again obtained at the last time step.

6.2.1 Evaluation

The similarity of Figure 6.3 to Figure 6.2 and the reduction of the position difference from kilometre to centimetre range indicates that the scaling works and the source of the differences between the NHPS and HPS simulation is of numerical nature. The behaviour of the difference depending on the inclination and eccentricity is also the same in the scaled simulations as in the unscaled simulations. The difference for the hyperbolic orbit is as expected visibly larger than for the closed orbit simulations. The trajectory is turned out of plane due to the gravity assist, which is not the case for the planetocentric simulation. A trajectory in the equatorial plane experiences

Table 6.4: *Definition of hyperbola and initial SC position in terms of Keplerian elements.*

Element	Value
eccentricity e	1.3
semi-major axis a	-2.793·10^7 m
inclination i	0°
longitude of ascending node Ω	0°
argument of periapsis ω	0°
true anomaly ν	-138°

no significant acceleration out of plane in the z-direction. In the scaled simulation this behaviour is three orders of magnitude smaller, in a range which could be explained by the irregular mass distribution of Earth and its description by the spherical harmonics Earth potential field but can not be proven in this thesis. The analyses of the scaling procedure for both planetary and interplanetary trajectory suggest no error in the scaling as the precision for both types of trajectories is improved.

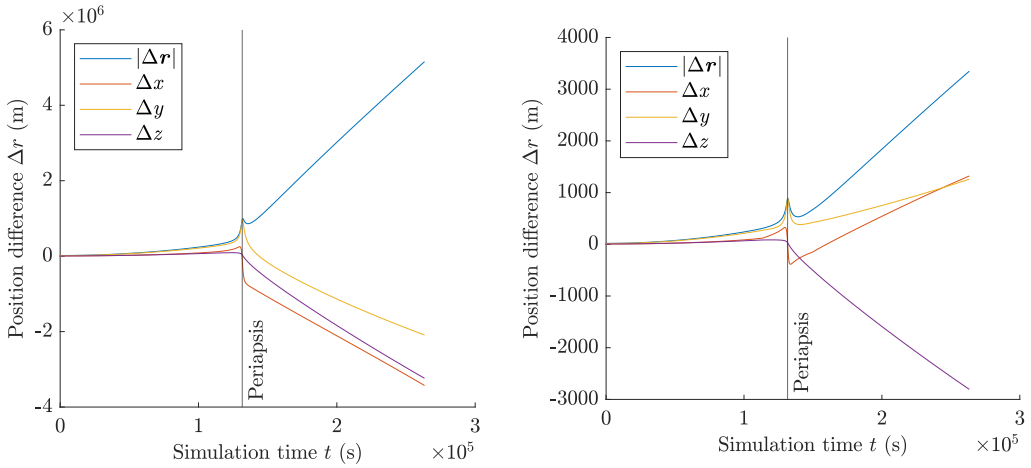

(a) *Unscaled simulation*

(b) *Unscaled simulation*

Figure 6.4: *The position difference of the planetocentric and heliocentric simulation of a hyperbola plotted over time. Dedicated graphs for each vector component and the euclidean vector norm are pictured.*

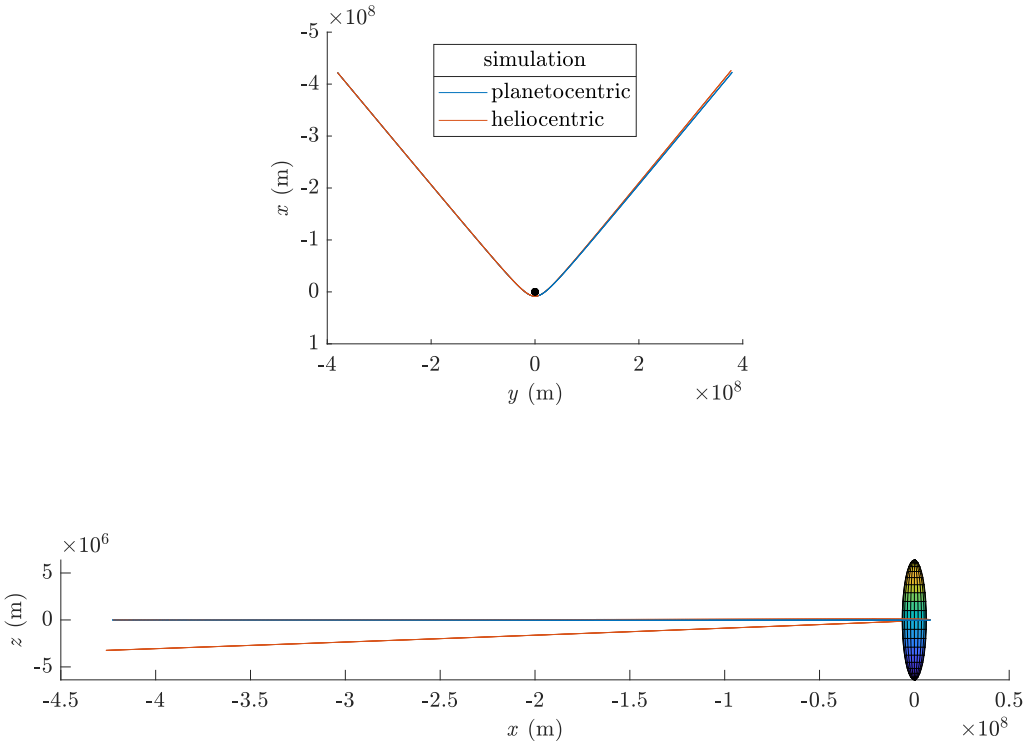

(a) *Trajectory of unscaled simulation. Top: LoS along z-axis, bottom: LoS along y-axis*

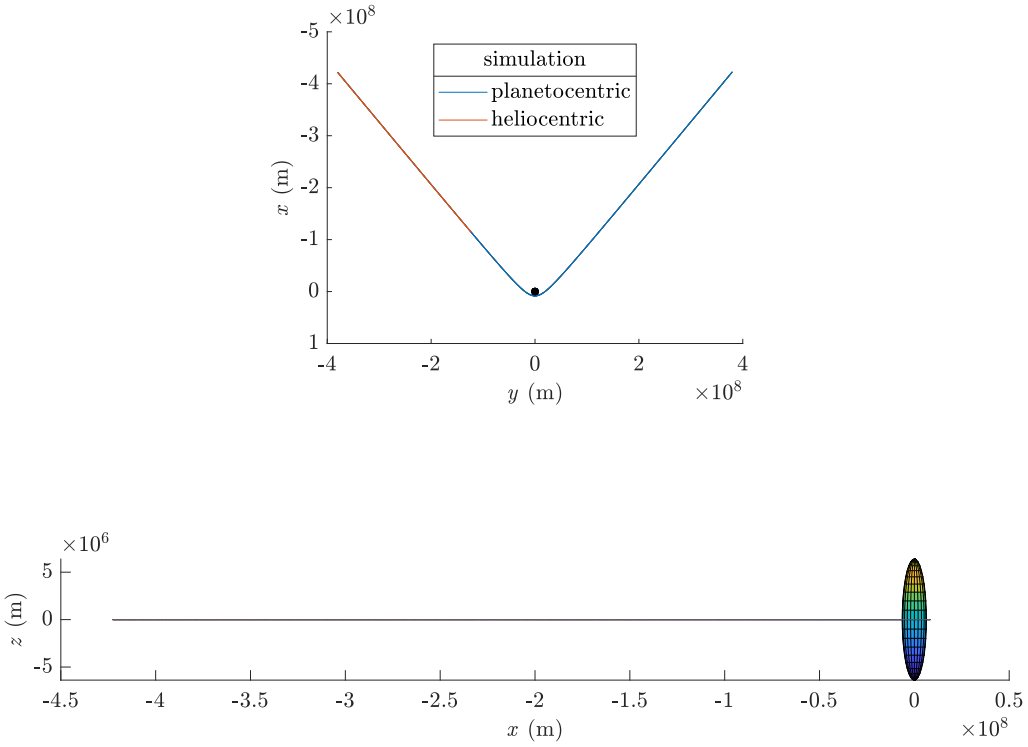

(b) *Trajectory of scaled simulation. Top: LoS along z-axis, bottom: LoS along y-axis*

Figure 6.5: *Plots of an example hyperbola around Earth. Each plot includes simulations in the planetocentric and heliocentric frame.*

6.2.2 Revision of Scaling

In a preliminary simulation for the reproduction of the first Rosetta gravity assist, it became apparent that the scaling procedure might be faulty. Unfortunately, this simulation was not done in the course of the model evaluation as the conducted validation simulations were assumed satisfactory. The scaling produces better results in terms of the difference to a HPS simulation for Earth orbits as well as hyperbolas. In the preliminary simulation of the Rosetta trajectory it was again compared how the scaling procedure affects the simulation results. Both simulations were matched against the actual Rosetta trajectory which is obtained from the JPL Horizons website [53] as tables for the position and velocity vector in both the ECI and HCI.
In Figure 6.6, the difference in position of the unscaled and scaled simulation with respect to the actual Rosetta trajectory is pictured. The dip in the difference plot of the scaled simulation is a result of the calculation of the difference and the way the difference is plotted. The position difference is calculated as follows:

$$\begin{aligned} \Delta \boldsymbol{r}\left(t\right) &= \boldsymbol{r}_{NHPS}^{ECI}\left(t\right) - \boldsymbol{r}_{Rosetta}^{ECI}\left(t\right), \\ \Delta r\left(t\right) &= \left|\Delta \boldsymbol{r}\left(t\right)\right| = \sqrt{\Delta x\left(t\right)^2 + \Delta y\left(t\right)^2 + \Delta z\left(t\right)^2}. \end{aligned} \tag{6.10}$$

The euclidean norm Δr is always a positive number, but the vector $\Delta \boldsymbol{r}$ is changing directions shortly after the entry in the SoI. The two trajectories cross each other, therefore the difference decreases at first and then increases in the opposite direction. The scaling leads to a significant change in the direction of the simulated trajectory. Not only is the maximum distance to the actual Rosetta position one OoM higher than without scaling, but also in the opposite direction in the ECI.
The three trajectories are pictured in Figure 6.7. The simulations start in the north-west corner of the figure, intercept Earth and are deflected more than 90°. At the end of the trajectories, the difference is clearly visible and it can bee seen that the unscaled and scaled simulation end on opposite sides of the actual Rosetta trajectory.
The objective of the scaling is to reduce the size of the solar system to decrease differences in equation terms and variables. For this, the heliocentric position and velocity of all planets are scaled but the planetocentric spacecraft states are left untouched. In combination, this yields a scaled and unscaled part of all three heliocentric spacecraft vectors - position, velocity and acceleration.
A review of the scaling process showed that the simple division of the third body perturbations in Eq. (6.7) contains an error because this scaled perturbation describes the acceleration for both scaled heliocentric planet and

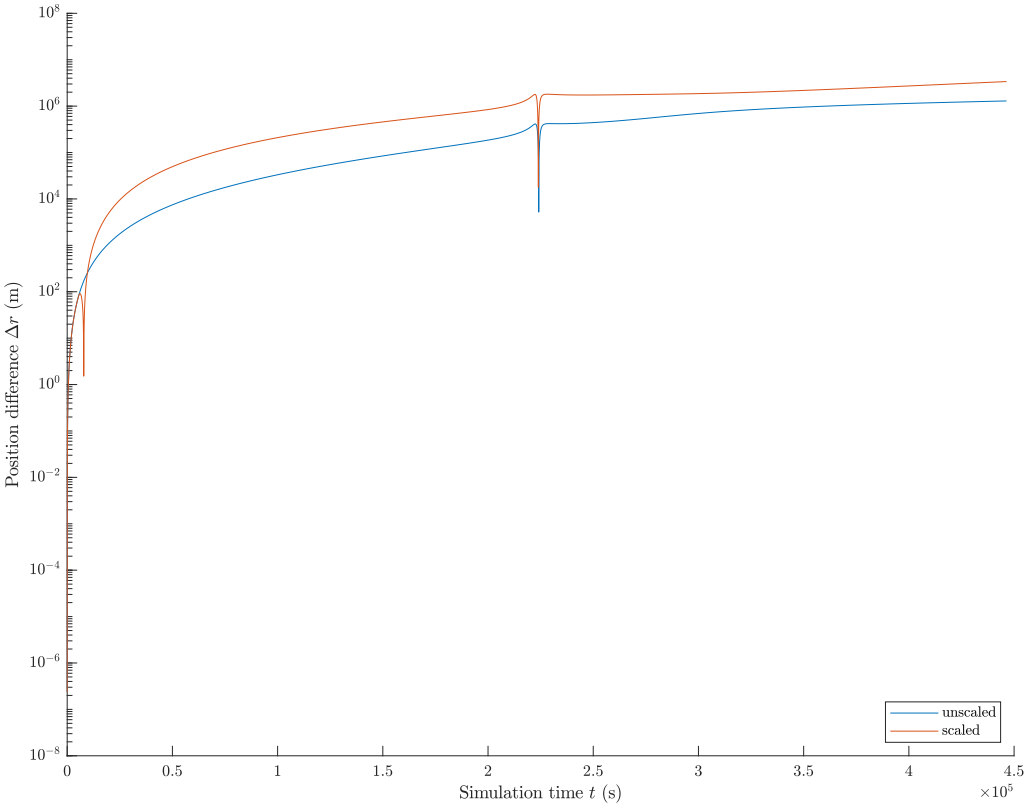

Figure 6.6: *Logarithmic plot of the position difference of an unscaled and scaled simulation to the actual Rosetta trajectory.*

scaled planetocentric spacecraft position. In an attempt to correct the scaling Eq. (2.20) is adapted in the following way:

$$\boldsymbol{p}_{3rd,s} = \mu_{3rd} \left(\frac{\left(\boldsymbol{r}_{3rd}^{HCI} - \boldsymbol{r}_{E}^{HCI}\right) \cdot \sqrt{f_{s1}} - \boldsymbol{r}_{SC}^{E,ecl}}{\left(r_{3rd}^{HCI\,3} - r_{E}^{HCI\,3}\right) \cdot \sqrt{f_{s1}}^{3} - r_{SC}^{E,ecl\,3}} - \frac{\boldsymbol{r}_{3rd}^{HCI} \cdot \sqrt{f_{s1}}}{r_{3rd}^{HCI\,3} \cdot \sqrt{f_{s1}}^{3}} \right). \tag{6.11}$$

Here, $\boldsymbol{r}_{3rd}^{HCI}$ and $\boldsymbol{r}_{E}^{HCI}$ denote the heliocentric position of the third body and Earth, respectively. $\boldsymbol{r}_{SC}^{E,ecl}$ describes the planetocentric ecliptic spacecraft position and μ_{3rd} the gravitational parameter of the third body.
The acceleration has an inverse dependency on r^2, therefore the scale factor is not applied by division but multiplied as its square root. Increasing the position with factor $\sqrt{f_{s1}}$ yields a decrease of acceleration with factor f_{s1}.
The evaluation of the new scaling routine confirms the impact of the scaling on Earth orbits. The new results for the orbits vary from the results

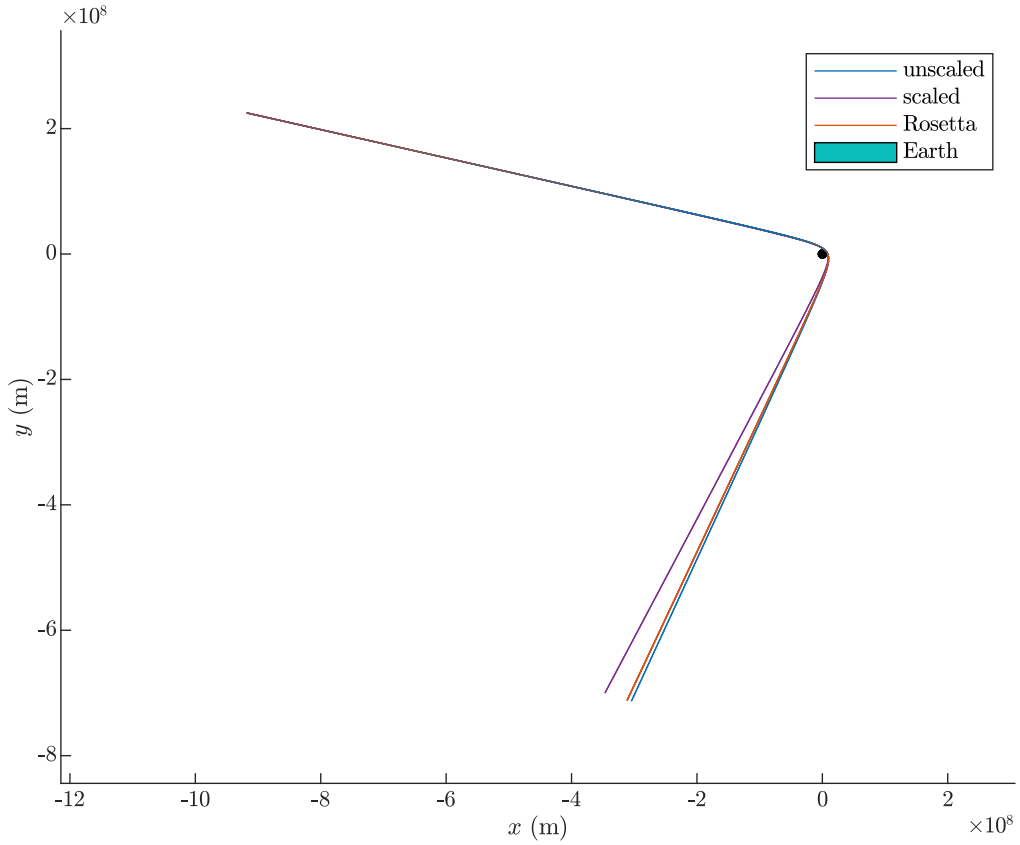

Figure 6.7: *Planetocentric trajectory of unscaled and scaled simulation and the actual Rosetta trajectory. LoS in -z-direction*

in Table 6.3 by just some millimetres. For the interplanetary trajectory in Table 6.4 the behaviour is similar and the result varies by some ten metres. Unfortunately, the same behaviour as pictured in Figure 6.6 can still be seen with the new scaling routine as well. The revision of the scaling has no beneficiary impact on the Rosetta simulations and the function is assumed to be faulty. Due to the time when this error was spotted, no further investigations into the cause and possible corrections were possible. In all further simulations of interplanetary trajectories the scaling option is deselected.

6.3 Gravity Assist

The analyses of the simulations described in Section 6.1 and 6.2 were done to evaluate the achievable precision of the NHPS by benchmarking the results

with the HPS simulations. This is done in the ECI because the HPS is limited to this frame, but due to this limitation the benchmarking gives no assertion about the performance of the NHPS in the heliocentric ecliptic frame. This master thesis focuses on gravity assists and their orbit-energy-altering effect is only existing in the heliocentric observation (regard Section 2.2). Therefore, a study is conducted in which it is assessed how well the NHPS can model the energy change of a gravity assist.
The study comprises of simulations of gravity-assist trajectories around Earth in the HCI. For these simulations, the velocity changes are calculated and compared to the analytical solution obtained from Eq. (2.40). Again using Kepler elements to define the trajectory, initial position and velocity, the simulations are setup in the NHPS with the complete three-body model. The elements for four exemplary trajectories are listed in Table 6.5.

Table 6.5: *Definition of example hyperbolas in terms of Keplerian elements.*

Element	**Value**			
eccentricity e	1.21	1.31	1.41	1.51
periapsis altitude h_p	$2.0{\cdot}10^6$ m			
inclination i	0°			
longitude of ascending node Ω	0°			
argument of periapsis ω	0°			
true anomaly of asymptote ν_∞	145.73°	193.76°	135.17°	131.47°

The true anomaly of the asymptote and the eccentricity are related as follows:

$$\nu_\infty = \cos^{-1}\left(-\frac{1}{e}\right). \tag{6.12}$$

Instead of the semi-major axis, the periapsis altitude is used for the definition of the hyperpolas, as this ensures that the periapsis is at the same distance from Earth for all four trajectories. The semi-major axis can be calculated with the periapsis radius and the eccentricity as follows:

$$a = \frac{r_p}{1-e}, \tag{6.13}$$

with Earth's radius and periapsis altitude:

$$r_p = h_p + R_E. \tag{6.14}$$

The definition of the initial position for the simulation requires a value for the true anomaly smaller than the asymptotic one. The true anomaly of the asymptote can be converted to a position vector, but the orbit radius of this position is infinitely large and cannot be used for numerical calulations. By using a negated and offset value of the true anomaly of the asymptote, an initial position closer than infinity is defined:

$$\nu = -\nu_\infty + \delta, \tag{6.15}$$

where δ denotes the offset. The simulation duration is defined by the double of the time from the initial position to the periapsis, which can be calculated with the Kepler equation and the hyperbolic eccentric anomaly F [8, p. 66, 12, p. 129]:

$$\tanh\left(\frac{F}{2}\right) = \sqrt{\frac{e-1}{e+1}}\tan\left(\frac{\nu}{2}\right), \tag{6.16}$$

$$M = e\sinh\left(F\right) - F, \tag{6.17}$$

$$t = M\sqrt{\frac{\mu}{a^3}}. \tag{6.18}$$

In Eq. (6.17) and (6.18), M denotes the mean anomaly and in Eq. (6.16) ν represents the true anomaly which is offset from the asymptotic value. For every hyperbola four different offsets are used to analyse the influence of the simulation time on the gravity-assist results. The true anomalies depending on the eccentricity and the offset are listed in Table 6.6 and the shapes of the trajectories are depicted in Figure 6.8. The dashed circle represents the dimension of the Sphere of Influence.

Table 6.6: *True anomaly ν in degree of the initial position for all simulations.*

e \ δ (°)	1.5	2.5	3.5	4.5
1.21	-144	-143	-142	-141
1.31	-138	-137	-136	-135
1.41	-133	-132	-131	-130
1.51	-129	-128	-127	-126

It can be seen that the higher the eccentricity and the higher the offset from the asymptotic true anomaly, the closer the initial position is to Earth

(marked by ×). Consequently, this leads to a shorter simulation duration. This is not only due to the lower distance to Earth of the initial and final position but it is also caused by the relation of the semi-major axis a to the escape velocity v_∞ [8, p. 69]:

$$v_\infty = \sqrt{\frac{\mu_E}{a}}. \tag{6.19}$$

The semi-major axis of the hyperbola decreases with increasing eccentricity e (see Eq. (6.13)), which further leads to the increase of the escape velocity.

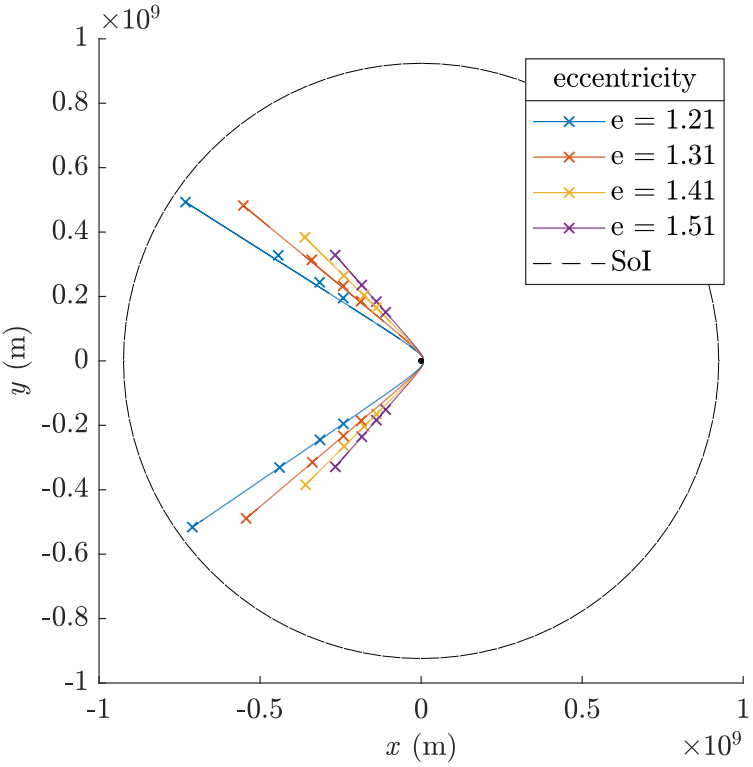

Figure 6.8: *Planetocentric view of hyperbolas around Earth. Markings with × describe initial and final position. LoS along z-axis*

For the comparison of the simulation's Δv to the theoretical value, Eq. (2.40) is used. For the theoretical Δv the deflection angle α is calculated with Eq. (2.39) and the eccentricity of the respective hyperbola. The escape velocity v_∞ is also calculated with geometrical values according to Eq. (6.19). The simulation Δv is not calculated with theoretical values but with the initial velocity with respect to Earth and the actual deflection angle. This

angle α_{sim} corresponds to the angle between the initial and the final velocity vector in the ECI and the values for the simulations are listed in Table 6.7:

$$\alpha_{sim} = \cos^{-1}\left(\frac{\boldsymbol{v}_i^{ECI} \cdot \boldsymbol{v}_f^{ECI}}{v_i^{ECI} v_f^{ECI}}\right). \tag{6.20}$$

Table 6.7: *Values of deflection angle α of simulated gravity assists with different offsets δ and the theoretical benchmark.*

e	α (°)				
	simulation (with δ (°))				theoretical
	1.5	2.5	3.5	4.5	
1.21	113.3	111.7	111.3	111.1	111.5
1.31	100.3	99.6	99.3	99.2	99.5
1.41	90.5	90.2	90.1	89.9	90.3
1.51	82.9	82.8	82.7	82.5	82.9

The results of the velocity change calculations are listed in Table 6.8 and the differences between both types are plotted in Figure 6.9 over the offset from the true anomaly of the asymptote.

Table 6.8: *Values of velocity change Δv of simulated gravity assists with different offsets δ and the theoretical benchmark.*

e	Δv (m/s)				
	simulation (with δ (°))				theoretical
	1.5	2.5	3.5	4.5	
1.21	5516.0	5600.7	5719.6	5843.3	5224.5
1.31	6109.6	6199.5	6309.0	6420.5	5863.1
1.41	6510.4	6607.6	6708.8	6809.2	6264.6
1.51	6771.3	6863.6	6955.9	7046.5	6524.2

It can be seen in the table that the velocity change increases for higher offsets. This occurs for each eccentricity. Depending on the eccentricity, the Δv changes as well: the higher the eccentricity the higher the velocity change.

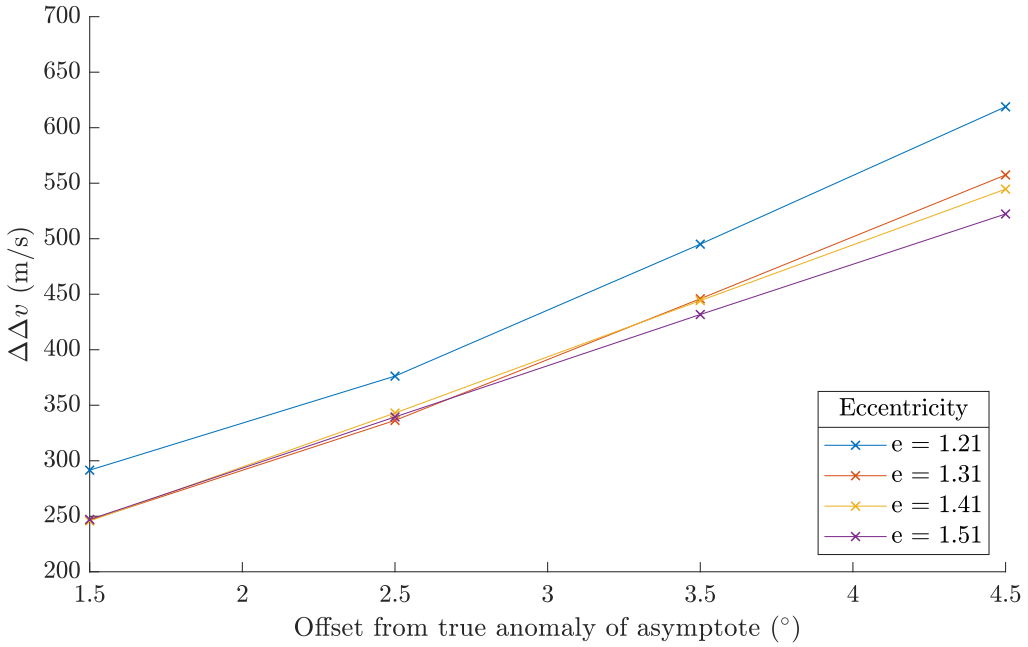

Figure 6.9: *Difference between the theoretical and simulation Δv plotted over the offset from the true anomaly of the asymptote.*

Figure 6.9 shows that the difference in the velocity change ($\Delta\Delta v$) increases with the offset. For the highest offset the $\Delta\Delta v$ also increases with decreasing eccentricity of the hyperbola. This phenomenon is not recurrent for the smaller offsets, where the $\Delta\Delta v$ has no clear dependency on the eccentricity. The smallest difference between the theoretical and simulation value of the velocity change is achieved for the trajectory with eccentricity of 1.41 and an offset of 1.5°. The highest value is received for $e = 1.21$ and $\delta = 4.5°$.

6.3.1 Evaluation

The dependency of the velocity change on the eccentricity detected in Table 6.8 can also be described as a dependency on the deflection angle α based on Eq. (2.39). The velocity change for trajectories with a periapsis altitude of 2000 km is plotted in Figure 6.10 depending on the deflection angle α. The maximum is located at α equal to 60°. Regarding the values of the deflection angles of the simulated gravity assists in Table 6.7, which are all over 60° and decrease with increasing eccentricity, the results of the velocity change can be verified. In the table with the deflection angles the simulation values greater than the theoretical values attract attention. On a hyperbola the

angle between velocity vectors closer to Earth than infinity cannot be larger than the true anomaly of the asymptote. The higher values indicate a divergence from a hyperbola in the simulations. In Figure 6.8, the plot of the hyperbola with an eccentricity of 1.21° (blue) shows that the trajectory with $\delta = 1.5°$ is more deflected than the simulations with higher offsets. This is also evident in Table 6.7. It is highly likely that the higher deflection angle is caused by the acceleration of the Sun. The greatest divergence from a hyperbola is apparent for the trajectory which is simulated the longest and for shorter trajectories the difference is smaller. Due to the Sun's acceleration the trajectory diverges from a Keplerian orbit.

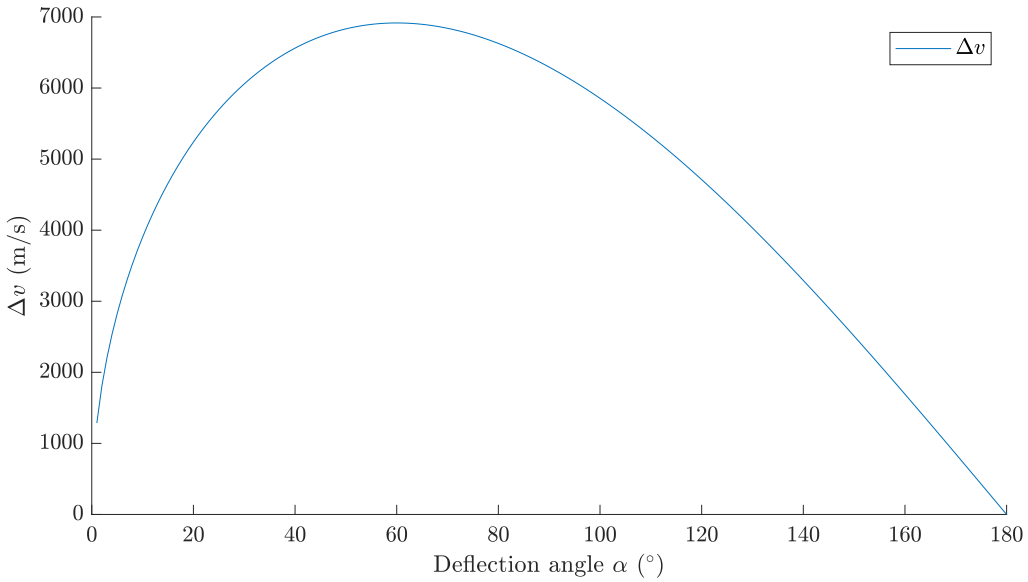

Figure 6.10: *The velocity change Δv for Earth-gravity assists with a periapsis altitude of 2000 km plotted over the deflection angle α.*

Due to the gravity well of Earth, the velocity in the infinity, v_∞, is the smallest during the whole trajectory. The initial velocities of the simulations are at positions closer to Earth than v_∞, therefore the velocity is higher than the escape velocity - between 140 and 415 m/s higher. This deviation in addition to the different deflection angles are the reasons for the difference of simulation and theoretical values calculated with the same equation. The maximum difference for the simulation of a hyperbola with $e = 1.21$ and offset of 4.5° is about 12 %. The differences for simulations with an offset of 1.5° are not higher than 5.6 %.
Kemble [15, p. 219f.] states that the modelling of a gravity assist is most precise if the trajectory is simulated from a position at or outside the Sphere of

Influence to a final position also at or outside the Sphere of Influence. In Figure 6.8 it can be seen that every simulation was simulated between positions inside the Sphere of Influence. This is due to the shape of the exemplary hyperbolas. Kemble's recommendation can be interpreted as: the farther away the initial and final positions are from Earth, the more precise are the simulations. This could not be validated in this analysis. Kemble chooses the SoI as the position of evaluation because it can be estimated as infinity with respect to Earth due to its dimension. The gravitational influence of Earth at the SoI is negligible [15, p. 219f.] and it is assumed that the escape velocity is reached. The difference between the final and initial heliocentric velocity at the SoI qualifies the gravity assist as precise as possible.
Through the adaptation of the HPS it is not known if the simulation of a gravity assist is performed correctly by the NHPS. The only possibility to evaluate the NHPS in this case is the comparison to the theoretical value from Eq. (2.40) because no results from other simulation tool are available. The theoretical Δv is calculated under the assumption of a Keplerian hyperbola, which omitts important effects altering the trajectory of a spacecraft. Therefore, the value the simulation results are compared with is not the most precise result for the calculation of a gravity assist.
The simulations show that the simulation results of each hyperbola match the theoretical Δv better, the closer the initial states are to the infinity values. The combination of the obtained results and the recommendation of Kemble leads to the acceptance of the NHPS ability to model gravity assists. In later simulations the initial position and simulation duration are chosen so that Kemble's recommendation is fulfilled.

Chapter 7

Study of Space-Environmental Effects

In this chapter, the NHPS is used to study the effects of the space environment on an interplanetary trajectory. These effects include the gravitational acceleration due to higher precision Earth-gravity models and additional celestial bodies as well as non-gravitational accelerations. The perturbations include atmospheric drag, solar-radiation pressure, Earth albedo and infrared influence and thermal-radiation pressure. The focus lies on the effects of the non-gravitational perturbations depending on different spacecraft attitudes. An analysis of the influence of the variation of the radiation surface properties exceeds the scope of the master thesis, but it has to be noted that distinct properties for the visible and infrared range of the electromagnetic spectrum are defined.
For an optimal simulation of the non-gravitational perturbations the foundation of the simulation in terms of the truncation of Earth's gravity field and other gravitational influences has to be defined first. Starting with the gravitational model of Earth it is determined how a higher order and degree of the spherical harmonics Earth potential field affects the trajectory and at which order a truncation of the field is determined acceptable in terms of precision. Second, the influence of Earth tides is examined and it is evaluated if they should be considered in later simulations. For the third-body perturbations the procedure is the same: Is it necessary to include all major bodies in the solar system or is the influence negligible for some? Then, the non-gravitational perturbations in combination with different spacecraft attitudes are investigated.
These studies are not performed with exemplary trajectories but with initial spacecraft states of Rosetta. It is examined how precisely the first Earth-gravity assist of Rosetta in March 2005 can be reproduced. Based on a

possible use of the NHPS for a further study of the Flyby Anomaly, the threshold if a environmental effect is considered in simulations is linked to the Flyby Anomaly. It is set to ten percent of the necessary Δv_p at pericentre which is necessary to match the pre- and post-encounter measurements. Anderson et al. [55] state this velocity change with $\Delta v_p = 0.67\,\mathrm{mm/s}$ for the first Rosetta-gravity assist.
The reference for all simulations to define the gravitational foundation is the complete three-body model (C3BM), which is used to integrate Rosetta's heliocentric initial states for a duration of 124 hours. The results of those simulations are then used as the baseline for the analyses of the non-gravitational perturbations.
The initial states represented in the ECI for the date 02.03.2005 8:00 TDB (Barycentric Dynamical Time) are listed in Table 7.1. In compliance with Kemble [15, p. 219f.], the initial and final position lie just outside of the Sphere of Influence ($r_{SC}^{ECI} > 0.924 \cdot 10^9\,\mathrm{m}$). An illustration of the simulated C3BM reference and Rosetta's trajectory can be found in Figure 6.7 and the progression of the position difference is pictured in Figure 7.1. The trajectories slowly diverge until the periapsis, then the divergence increases notably. The difference in the xy-plane is significantly higher than in z-direction.

$\boldsymbol{r}_{SC}^{ECI}$ (m)	$\boldsymbol{v}_{SC}^{ECI}$ (m/s)
$\begin{pmatrix} -9.176 \\ 2.25 \\ 0.451 \end{pmatrix} \cdot 10^8$	$\begin{pmatrix} 3.875 \\ -0.875 \\ -0.139 \end{pmatrix} \cdot 10^3$

Table 7.1: *Initial states in the ECI for all simulations of the Rosetta trajectory. Obtained from JPL Horizons website [53] for the date 02.03.2005 8:00 TDB*

All comparisons of the position and velocity in the following analyses use the calculations stated below if not stated differently. The position difference is calculated between one simulation and the reference with the complete three-body model as follows:

$$\begin{aligned} \Delta \boldsymbol{r}\,(t) &= \boldsymbol{r}_{sim}^{ECI}\,(t) - \boldsymbol{r}_{C3BM}^{ECI}\,(t)\,, \\ \Delta r\,(t) &= |\Delta \boldsymbol{r}\,(t)\,| = \sqrt{\Delta x\,(t)^2 + \Delta y\,(t)^2 + \Delta z\,(t)^2}. \end{aligned} \tag{7.1}$$

$\Delta r\,(t)$ decribes the distance between the spacecraft from two simulations at the time t. The velocity difference is calculated between one simulation and the reference as follows:

$$\begin{aligned} v_{sim}^{ECI}\,(t) &= |\boldsymbol{v}_{sim}^{ECI}\,(t)\,|, \\ v_{C3BM}^{ECI}\,(t) &= |\boldsymbol{v}_{C3BM}^{ECI}\,(t)\,|, \\ \Delta v\,(t) &= v_{sim}^{ECI}\,(t) - v_{C3BM}^{ECI}\,(t)\,. \end{aligned} \tag{7.2}$$

$\Delta v\,(t)$ describes the difference in the velocity of both simulations with respect to Earth at the time t.

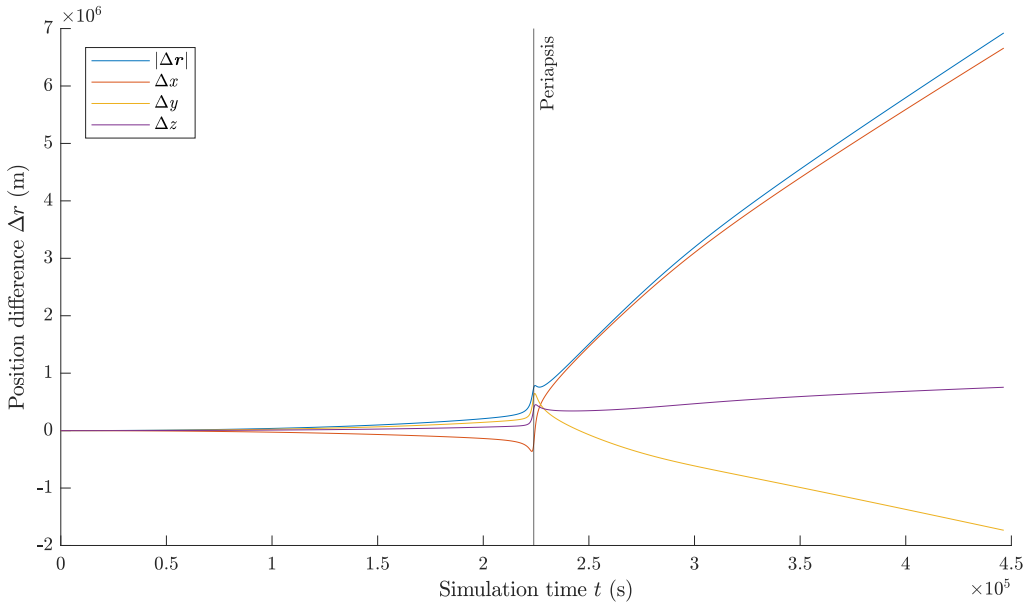

Figure 7.1: *The position difference of the C3BM to the Rosetta trajectory plotted over time. Dedicated graphs for each vector component and the euclidean vector norm are pictured.*

7.1 Order of Spherical Harmonics Earth Potential Field

With the initial position and velocity vector listed in Table 7.1, simulations with increasing order and degree of the spherical harmonics Earth potential field are conducted. According to Thompson et al. [36] the Juno Flyby showed a sensitivity to potential fields of order and degree as high as 100x100.

Therefore, a sensibility analysis for the Rosetta trajectory is performed. In total five simulations are run with order and degree of 6, 16, 26, 36 and 46. The position and velocity differences of the second up to the last simulation are compared to the results of the previous simulation. Meaning simulation with $O16$ is compared to $O6$, $O26$ to $O16$ and so forth. Through this, the impact of a higher order field on the trajectory can be determined. The criterion which order gravity field is used for further simulations is the Flyby Anomaly observed for the first Rosetta gravity assist as stated above. The first simulation for which the higher order yields a maximum velocity difference smaller than $0.0067\,\mathrm{mm/s} \equiv 6.7 \cdot 10^{-5}\,\mathrm{m/s}$ is assumed sufficiently precise.
In Figure 7.2, the velocity difference between two consecutive simulations is plotted in a logarithmic scale over the simulation time. The time axis starts around 55.5 hours because the higher order model does not affect the trajectory from the beginning of the simulation. The distance of the spacecraft to

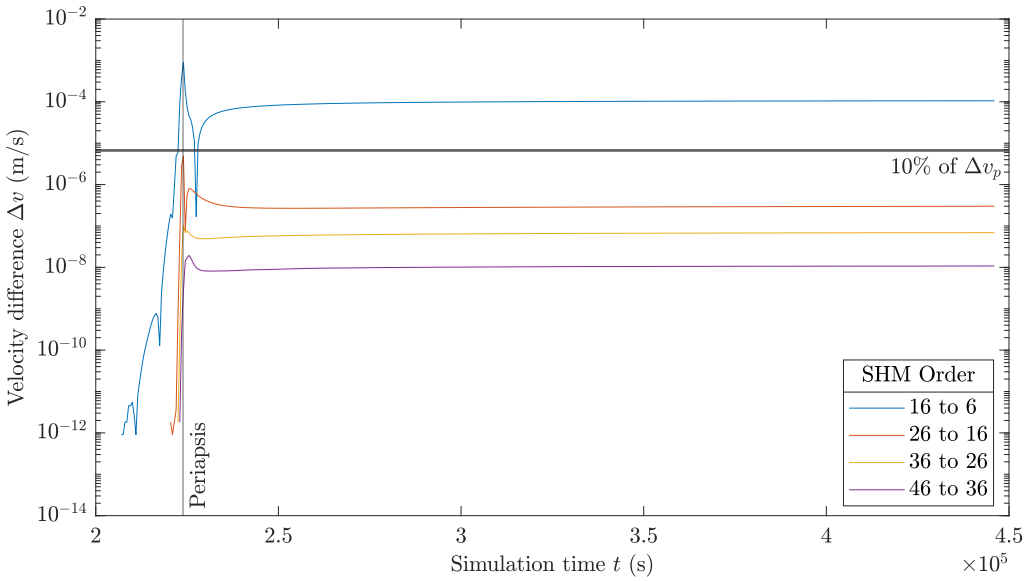

Figure 7.2: *The velocity difference of consecutive simulations plotted over time.*

Earth is too high for the higher order filed to have an impact. The higher the order the later the first difference occurs for the simulations and the smaller the overall difference. The periapsis of the first trajectory is marked in the plot and aligns with the other trajectories to the second. It can be seen that the difference is at a maximum at or close to the periapsis for every comparison. Because of the logarithmic scale, negative values cannot be displayed

and the difference is plotted as the absolute value. This means every local minimum in the plots is a zero crossing and the difference changes its sign. The red plot is the first in which the difference between two simulations is below the threshold of $6.7{\cdot}10^{-5}$ m/s.
The position difference is also plotted in logarithmic scale and over the simulation time. The differences can be seen in Figure 7.3. The behaviour of the plots at the local minima is equal to the explained one for the velocity plot and their maximum is always at the last simulation time step due to the propagation of differences after the gravity assist when Earth's influence gradually decreases. It can be seen that the influence of higher order models gets smaller the higher the order is. For the first comparison the maximum position difference is 22.6 m whereas for the last it is only 2 mm.

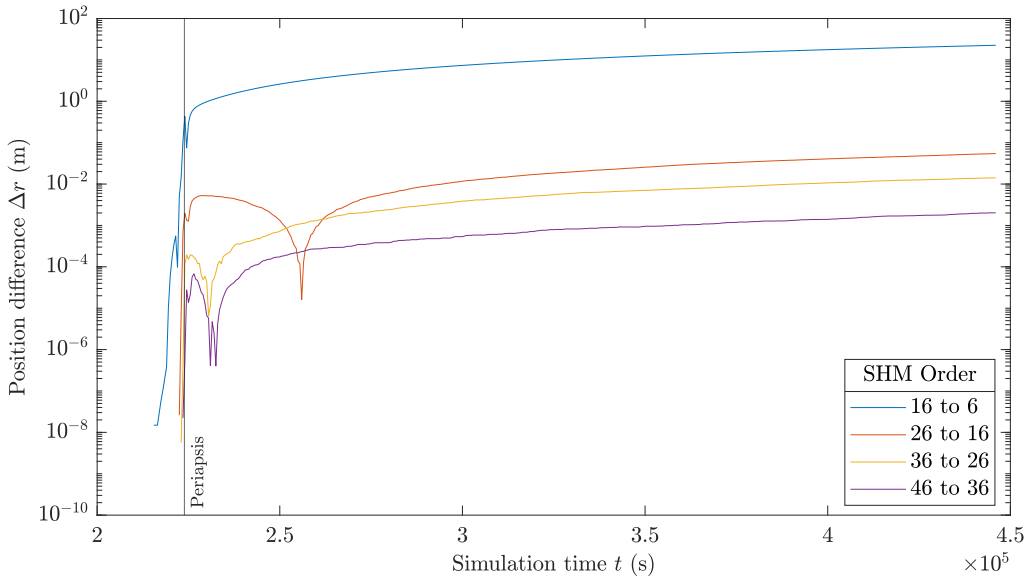

Figure 7.3: *The position difference of consecutive simulations plotted over time.*

7.1.1 Discussion

The analysis of the gravity field order is conducted to evaluate its influence on the Rosetta trajectory. As stated before Thompson et al. [36] found a non-negligible dependency for orders up to 100. This leads to a significantly higher computational effort which had to be justified for this master thesis. The outcome of this analysis is that the use of the spherical harmonics Earth potential field of order 26 provides sufficiently precise results. The maximum

velocity difference to order 16 is $7.2{\cdot}10^{-6}$ m/s at two minutes before the periapsis and yields a position precision in the single digit centimetre range. Higher orders do not justify the higher computational effort with regard to the additional precision, as the differences are well below the set threshold of a tenth of the Flyby Anomaly of Rosetta.

7.2 Earth Tides

The HPS is capable of including four different tide models in the calculation of Earth's gravitational acceleration (see Section 4.1.1). Based on the findings of the potential field order analysis the influences of the tide models are examined. Four simulations are run, in which the the single effect of one tide model is included. The ocean and pole tide model order are set equal to the static order and the solid-Earth tide is set to its maximum of four for both the elastic and anelastic case. The results of the four simulations are then compared to the reference C3BM with spherical harmonics Earth potential field of order 26.
Again, the threshold for the decision if the tide models need to be included in further simulations is ten percent of the Flyby Anomaly at the pericentre. The influence of the models on the velocity is pictured in Figure 7.4.

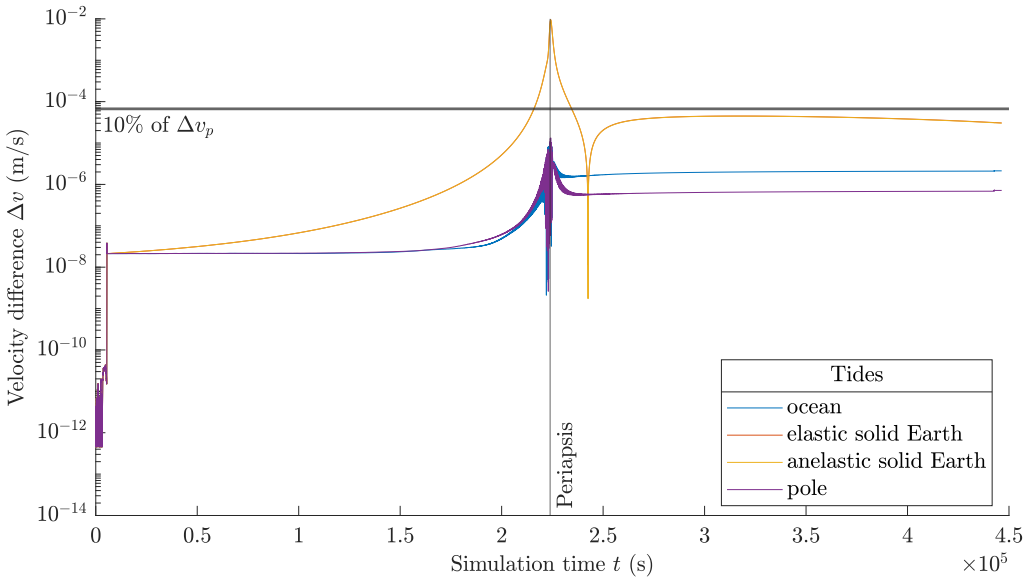

Figure 7.4: *The velocity difference due to different tide models plotted over time. The difference is calculated to the reference simulation with only the C3BM*

It can be seen in the velocity plots that there is a jump close to the beginning of the simulation. This happens at the point of entry in the Sphere of Influence at which the gravity model is switched from simple to spherical harmonic. In the simple gravity model the tides are neglected and only calculated after the switch to the more precise spherical harmonics model. Only three plots are visible in this figure because the plots of the elastic and anelastic solid-Earth tide align nearly perfectly. Because of the logarithmic scaling only absolute values of the velocity differences are plotted. This means that every local minimum is again the point of a zero crossing and the change of the difference sign.
In Figure 7.5, the difference between the two solid-Earth tide models is magnified for the decision between the elastic and anelastic solid-Earth tide model. The difference of the two models has a maximum of $1.34{\cdot}10^{-5}\,\mathrm{m/s}$ shortly before the pericentre of the trajectory.

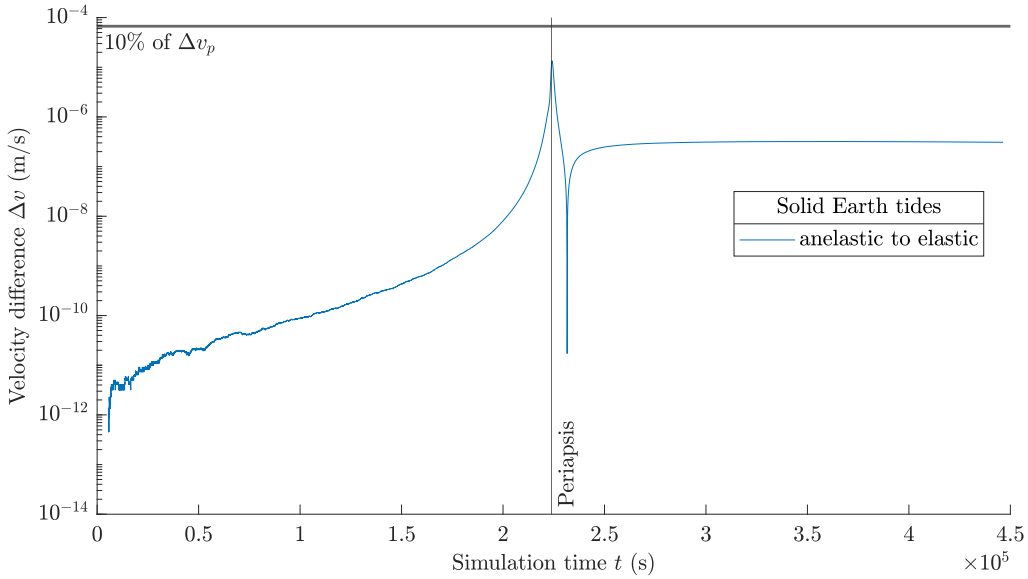

Figure 7.5: *The velocity difference between the anelastic and elastic solid-Earth-tide model plotted over time.*

7.2.1 Discussion

From Figure 7.4 can be concluded that the influence of both the ocean and pole tides can be neglected as they affect the trajectory well below the threshold of $6.7{\cdot}10^{-5}\,\mathrm{m/s}$. This leaves the elastic and anelastic solid-Earth tide, which cannot be calculated simultaneously but are different options for one

tidal effect. Figure 7.5 shows that the maximum difference from the anelastic to the elastic tide is only 20 % of the threshold. Therefore, the elastic description is precise enough for further analyses. The result of the tide analysis is that the elastic solid-Earth tide is the only tide model which has an effect on the simulation large enough that it needs to be considered in further studies. The maximum position difference of the elastic solid-Earth tide is at ca. 3200 m whereas the ocean and pole tides only alter the position in the centimetre and single digit metre range.

7.3 Third-Body Perturbation

After defining the extent to which Earth's gravitational acceleration has to be modelled in the study of the non-gravitational perturbations, the focus is changed to the other major bodies in the solar system. All HPS applicable bodies are listed in the beginning of Section 4.1. The setup for the analysis of the third-body perturbations is as follows. Ten simulations are run with the NHPS. The first is the reference with the C3BM. In the subsequent nine simulations one additional body is included in the simulation. To reduce the computational time, the results of the tide analysis are omitted under the assumption that a maximum position deviation of ca. 3200 m does not noticeably affect the influence of the third bodies due to their much higher distance and not alter the selection of the further considered bodies.

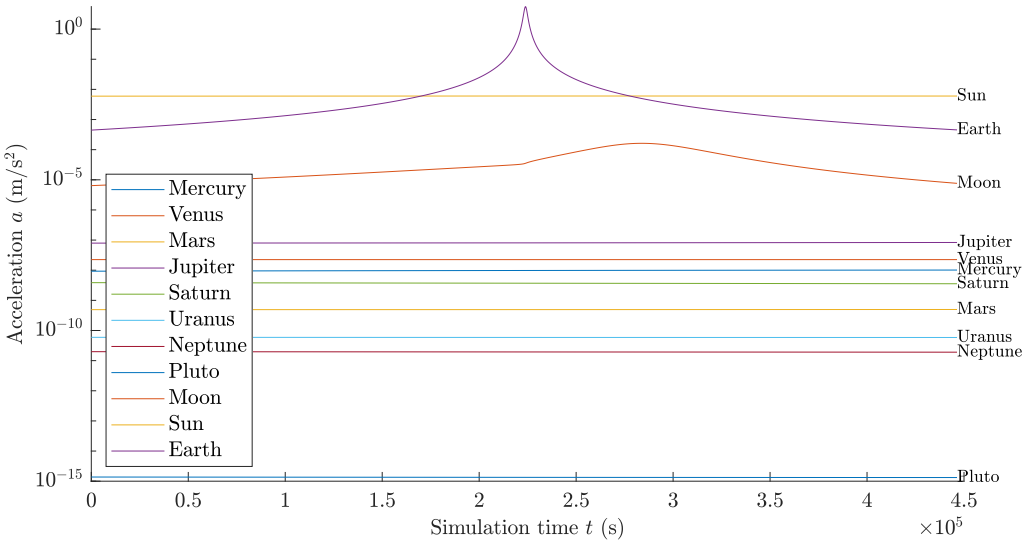

Figure 7.6: *The acceleration magnitude due to all major celestial bodies plotted over time.*

The simulations show that the different bodies influence the trajectory as little as 0.01 m and as high as 6850 km. The velocity influence ranges from $8.89{\cdot}10^{-8}$ m/s to 156.12 m/s with each being the maximum value of the respective simulation. Both properties can be ascribed to the magnitude of the acceleration due to the different bodies. Figure 7.6 pictures the acceleration exerted by the Sun and Earth from the reference run and all third-body perturbations. Prominent is the trend of the accelerations due to Earth and the Moon. They are the only two accelerations which change noticeably over the course of the trajectory. This is not surprising considering that Earth is the Flyby body. Rosetta approaches Earth to as near as 2000 km altitude and the Moon is the next closest body at ca. 380000 km. Therefore, the distance to these two bodies change significantly which yields the increasing and decreasing accelerations. The trend of the remaining accelerations supports the assumption of omitting the tides, as the accelerations remain nearly constant over the time the spacecraft travels around 14 million kilometres.

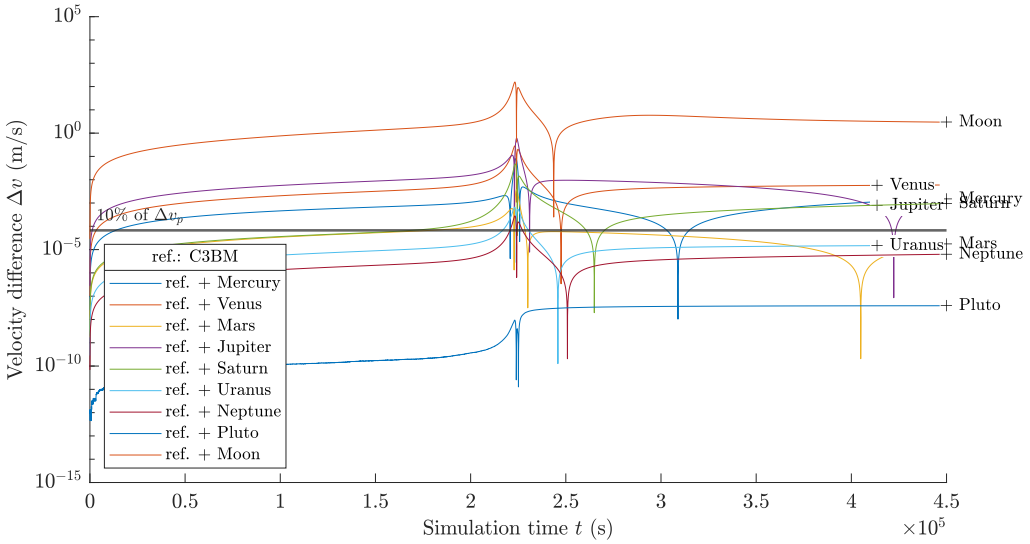

Figure 7.7: *The velocity difference due to the third-body perturbations of all major celestial bodies plotted over time. The difference is calculated to the reference simulation with only the C3BM.*

The influence of the third bodies in terms of the velocity is pictured in Figure 7.7. Due to the highly different results, the absolute values of velocity differences are again plotted in a logarithmic scale. The horizontal line describes the threshold of $6.7{\cdot}10^{-5}$ m/s, which is not surpassed by only one body. The velocity difference due to the gravitational acceleration due to Pluto is below the threshold at all times. The difference due to Mars, Uranus and Neptune

are below the threshold for the most time as well, but their maxima, which are close to the periapsis, are above $6.7{\cdot}10^{-5}\,\mathrm{m/s}$. The order in which the accelerations are pictured in Figure 7.6 is mirrored in the plots for the velocity differences. The Moon has the biggest influence on the velocity, Pluto the smallest and bodies that are close together in the acceleration plots have similar effects on the velocity. In the position plots, the acceleration order can be mostly found again, with the exception that Neptune and Uranus as well as Mercury and Venus switched places.

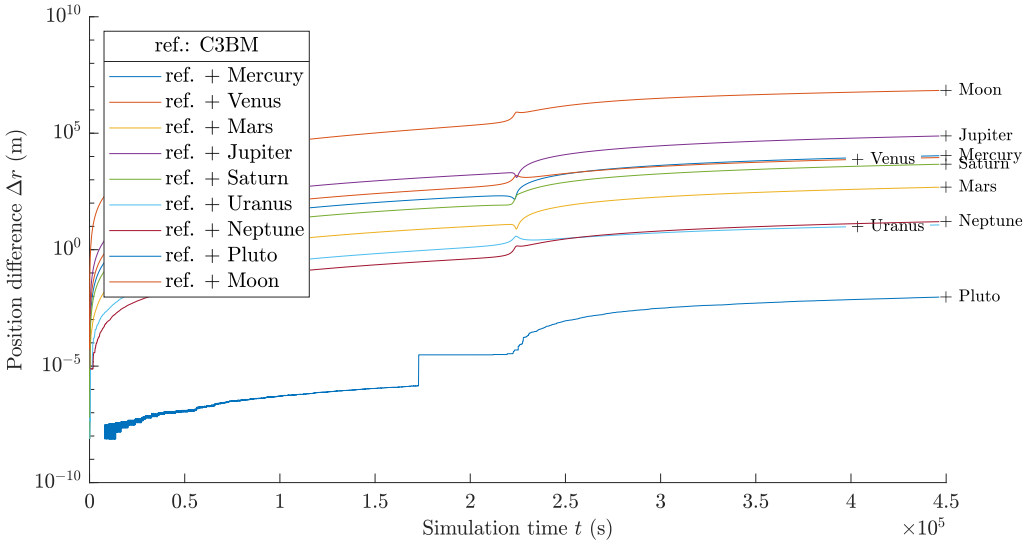

Figure 7.8: *The position difference due to the third-body perturbations of all major celestial bodies plotted over time. The difference is calculated to the reference simulation with only the C3BM.*

It has to be noted that absolute values of the euclidean vector norm of the respective vectors are pictured in all three figures. Therefore no statement about the direction of the position difference is made. The sign of the velocity difference can also not be obtained from the plots. Depending on the position of the third body the velocity is increasing or decreasing. Only sign changes can be spotted in Figure 7.7 at positions of local minima in each graph.

7.3.1 Discussion

Based on Figure 7.7 only Pluto is deemed to have an negligible effect on the trajectory and is disregarded for further simulations. Mars, Uranus and Neptune are included in further simulations even though the velocity difference is below the threshold for the majority of the simulations. The combination of a four to five orders of magnitude higher acceleration than for Pluto and their maximum being above the threshold leads to the conclusion that these bodies need to be considered to achieve satisfactory precision.
The direction of the influence is obviously distinct for the different bodies due to their relative positions to the spacecraft. The combination of all third bodies in a simulation will most likely result in different results than the simple addition of the position differences of the single bodies. Due to the different directions, the accelerations exerted by the bodies on the spacecraft cancel each other to some small degree.
With this analysis all gravitational sources are defined for the analysis of the non-gravitational perturbations. It is concluded that the static geopotential field of order/degree 26 and the elastic solid-Earth-tide model describe the gravitational influence of Earth well within the precision of the detected Flyby Anomaly of the first Rosetta-gravity assist. Additionally, the third body perturbations of the following bodies are used to extend the complete three-body model to an n-Body model with $n = 11$:

- Mercury
- Venus
- Mars
- Jupiter
- Saturn
- Uranus
- Neptune
- Moon

7.4 Non-Gravitational Perturbation

All gravitational influences are calculated inside the *Dynamics Core* of the NHPS. For the calculation of the non-gravitational perturbations the Simulink model has to be extended similar to the description in Section 4.3. An overview and detailed pictures of the model are given in the Appendix in Figures B.1 to B.3. The non-gravitational perturbations include solar and thermal radiation pressure, Earth albedo and infrared as well as atmospheric drag. The thermal radiation pressure is only calculated with the solar radiation due to a peculiarity in the Simulink functions. In theory, the albedo and infrared radiation also have a share in the thermal radiation pressure. As stated in the theoretical background (Section 2.1.2.4), the incident power on every visible element is calculated as the sum of the radiation of every Earth

surface segment in the field of view. The division of the spacecraft surface in almost 1000 elements and the segmentation of Earth's surface leads to a large amount of computations for every time step, which exceeded the computational capabilities of the used machine.
The analysis of the non-gravitational perturbations is split into two parts. First, every perturbation is included individually in the Simulink model and simulations are run for four different attitudes. The effects of each perturbation in combination with the attitudes is evaluated with respect to the baseline n-Body model. Second, all perturbations are included simultaneously and the precision to the actual Rosetta trajectory is evaluated. Additionally, it is attempted to detect possible reasons for the remaining difference.

7.4.1 Attitude Options

The perturbations are analysed for four different spacecraft attitudes to learn more about the influence of the attitude in the simulation of interplanetary trajectories. The first attitude is called Nadir pointing. In this setup one axis of the spacecraft's body-fixed coordinate frame is always pointing to Earth. In Figure 4.1, the x, y and z-axes of the mechanical frame are depicted. The mechanical and body-fixed frame have the same orientation and according to Figure 4.1, the x-axis is perpendicular to the solar arrays. To choose an attitude with a plausible use case, it is decided to point the x-axis of the body-fixed frame to Earth at all times. By pointing the high-gain antenna (HGA) towards Earth, communication can be established. The second attitude is labelled constant flight path angle (cFPA) in the Simulink model, which is misleading. The flight path angle is the angle between the local horizontal direction $\boldsymbol{n}_h$ (perpendicular to the position vector $\boldsymbol{r}$) and the velocity vector $\boldsymbol{v}$, which varies for all non circular orbits [9, p. 56]. Figure 7.9 depicts the geometry for an elliptical orbit with F and F' being the focal points of the ellipse.

Consequently, during the hyperbola Rosetta describes around Earth, the flight path angle is not constant as well. However, by definition of the attitude the angle between the body-fixed axes and a specific vector is kept constant. The vector chosen as the guideline is the relative velocity vector of the spacecraft to the atmosphere (see Eq. (2.23)). To maximize the drag perturbation, the attitude is chosen that the largest possible cross-section area is perpendicular to the relative velocity vector. According to Figure 4.1,

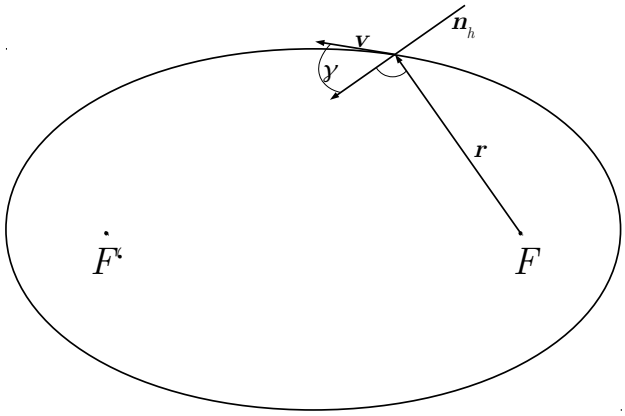

Figure 7.9: *The flight path angle in an elliptical orbit.*

the definition of the alignment is as follows:

$$\begin{aligned}
\boldsymbol{e}_x^b &= -\hat{\boldsymbol{v}}_{rel}^{ECI}, \\
\boldsymbol{e}_y^b &= -\hat{\boldsymbol{v}}_{rel}^{ECI} \times \hat{\boldsymbol{r}}_{SC}^{ECI} \equiv -\boldsymbol{h}, \\
\boldsymbol{e}_z^b &= \hat{\boldsymbol{v}}_{rel}^{ECI} \times \boldsymbol{h}.
\end{aligned}$$

Here, $\boldsymbol{h}$ denotes the angular momentum vector of the orbit. The third attitude is labelled Sun pointing, which is basically the same concept as Nadir pointing. The orientation of the spacecraft is chosen so that the x-axis of the body-fixed frame points towards the sun at all times. Through this, the solar arrays are in the optimum position for producing electrical power. At last, a set of actual quaternions of Rosetta was provided. This set unfortunately ends at 02.03.2005, 21:16 and only covers ca. 10 % of the simulated duration. Therefore, no information about the actual attitude during critical mission phases are known. The approach for times in which no attitude is provided, is that the last available quaternion is held constant for the remaining simulation duration.
Further should be noted that for the first three attitude options a perfect controller is assumed. Meaning, no controller is designed for the simulation and the attitude is not propagated under the influence of control and perturbation torques. Instead, the specified condition is used to calculate an attitude which is then used as the actual.

7.4.2 Individual Analysis

The baseline obtained from Sections 7.1, 7.2 and 7.3 includes the effects of Earth's gravitational field up to order 26, an elastic model for solid-Earth

tides and eight additional solar-system bodies. In Figure 7.1, the position difference of the simulation with the complete three-body model to the actual Rosetta trajectory is pictured. Through extension with the mentioned models, this difference could be reduce from 6923 km to 30.63 km. The progression of the difference for each vector component and the euclidean vector norm of the position difference is pictured in Figure 7.10.

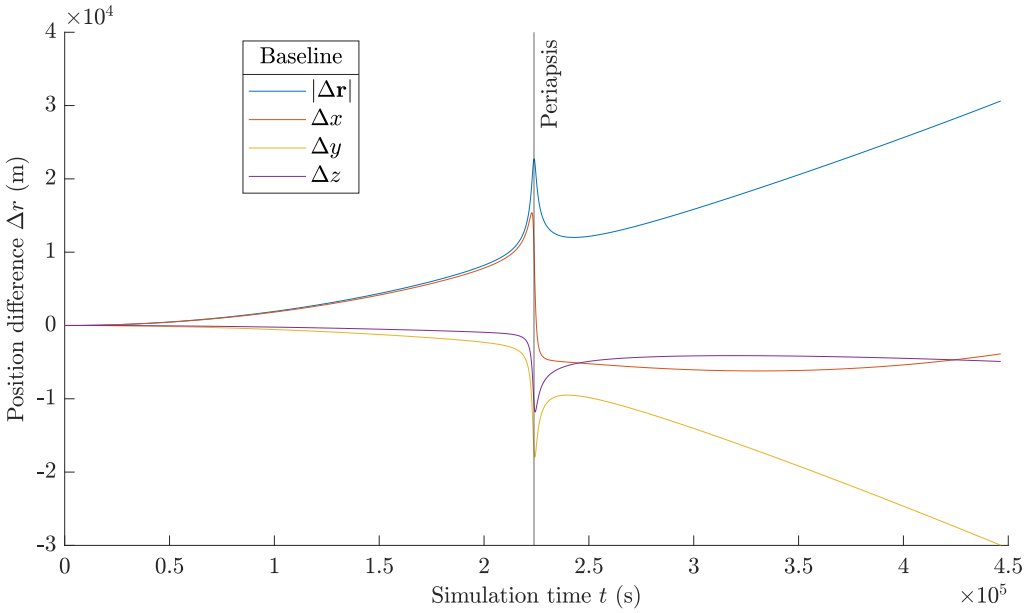

Figure 7.10: *The position difference of the baseline simulation to the Rosetta trajectory plotted over time. Dedicated graphs for each vector component and the euclidean vector norm.*

In the following, the results of the first part of the non-gravitational perturbation analysis in terms of the individual effects of the perturbations on the trajectory is presented. The Simulink functions return a force instead of an acceleration vector and hence the results are divided by the mass of Rosetta to obtain an acceleration. The mass is assumed with 2895 kg at the time of the gravity assist as stated by Anderson et al. [55].

7.4.2.1 Atmospheric Drag

The atmospheric drag is an effect due to the residual atmosphere around Earth. The minimum altitude of the baseline simulation is at around 1954 km above the surface of Earth. Therefore, it can be expected that the decelerating acceleration due to the residual atmosphere is small. The atmospheric

drag procedure assumes that the atmosphere is rotating with Earth without any friction and viscous behaviour. This leads to the relative velocity of the spacecraft to the atmosphere as described by Eq. (2.23). The density of the atmosphere is dependent on many factors besides the altitude which is included in the HPS by the Jacchia-Bowman (JB2008) model [56]. This model provides a very precise description of the density up to 1000 km and the density is extrapolated for altitudes for which no model data exists. The combination of the extrapolation of the density and the calculation of the relative velocity causes a faulty perturbation. At the initial position, the crossproduct of the position vector and Earth's rotation vector introduce a significant additional velocity component, which is higher than the heliocentric velocity of the spacecraft:

$$\boldsymbol{v}_{atm} = \boldsymbol{\omega}_E \times \boldsymbol{r}_{SC}^{ECI}, \tag{7.3}$$

$$\boldsymbol{v}_{atm} = \begin{pmatrix} 0 \\ 0 \\ 7.29 \end{pmatrix} \cdot 10^{-5} \times \begin{pmatrix} -9.176 \\ 2.25 \\ 0.451 \end{pmatrix} \cdot 10^{8}, \tag{7.4}$$

$$\boldsymbol{v}_{atm} = \begin{pmatrix} -1.64 \\ -6.69 \\ 0 \end{pmatrix} \cdot 10^{4}. \tag{7.5}$$

The extrapolation of the density yields a very small value at the initial position. Nevertheless, in combination with the relative velocity the function produces an atmospheric drag perturbation where no atmosphere exists. Due to this occurrence, a boundary condition is introduced for the atmospheric drag, which ensures that this perturbation is only calculated for altitudes under 10000 km. The spacecraft is below this altitude for a duration of 63 min, which is not long related to the overall simulation duration of 124 h. Based on the results, it is decided if the atmospheric drag has an influence that has to be further regarded or can be omitted due to the altitude and short duration.

The euclidean norm of the acceleration is pictured in Figure 7.11 for the four different attitudes over the duration the spacecraft is under 10000 km altitude above Earth. Overall, the strongest acceleration occurs for the constant flight path angle as the cross section area perpendicular the relative velocity vector is the the largest and constant. The accelerations for the Sun-pointing and real Rosetta attitude follow each other closely. Before the periapsis the trend for the constant flight path angle is very similar to these two as well. The Nadir-pointing graph is below the mentioned three attitudes for the most time of the plotted duration. This graph shows a dip in the acceleration at the periapsis.

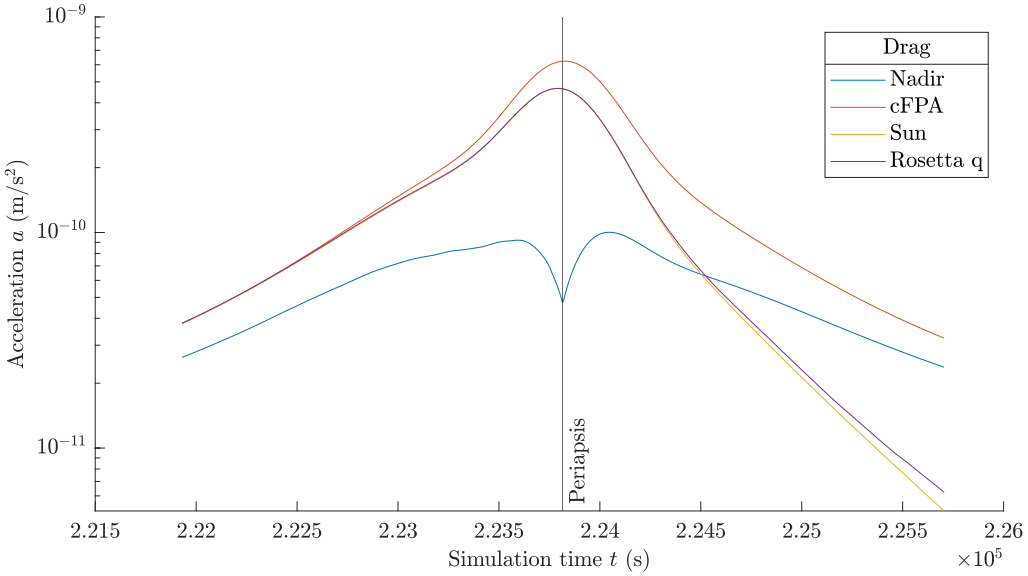

Figure 7.11: *The magnitude of the acceleration due to the atmospheric drag for four different attitudes plotted over the duration of 63 min.*

The effect of the perturbation on the velocity is pictured in Figure 7.12, where the plot begins at the time step the perturbation is turned on as the Δv before this point is zero. The same order as for the acceleration can be seen here. For the constant flight path angle the velocity difference is the highest, the Sun-pointing and real Rosetta attitude align very closely and for Nadir pointing the Δv is the smallest. It is important to note that all velocity differences are negative, meaning the spacecraft is decelerated due to the direction of the acceleration pointing against the velocity vector relative to the atmosphere. The maximum velocity difference of all four attitudes is $1.54{\cdot}10^{-6}$ m/s, which is little more than 2 % of the threshold for the gravitational effects ($6.7{\cdot}10^{-5}$ m/s). The perturbation yields a maximum position difference to the baseline of 0.4 m for the constant flight path angle at the last time step of the simulation.

7.4.2.2 Solar Radiation Pressure

The solar radiation pressure is a perturbation that acts on the spacecraft during the whole trajectory. With regard to the accelerations due to all celestial bodies (see Figure 7.6) and the nearly constant trend of the acceleration caused by the Sun, it can be expected that the magnitude of the solar-radiation acceleration is only depending on the attitude and potential shadowing of the spacecraft. The part of the solar radiation power in the

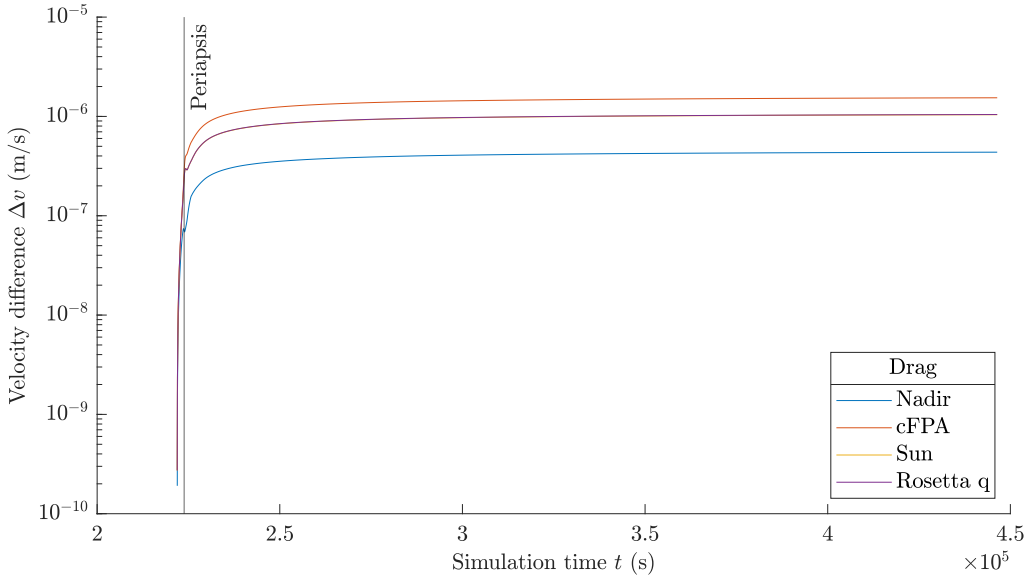

Figure 7.12: *The velocity difference to the baseline simulation due to the atmospheric drag for four different attitudes plotted over the duration of 63 min.*

acceleration follows the same trend as the gravitational acceleration, as it is also only dependent on the distance to the Sun. In Figure 7.13, the acceleration magnitude of all four attitudes plotted over the simulation duration can be seen and three different trends can be distinguished. The acceleration for the Sun-pointing and real Rosetta trajectory are again very similar and stay nearly constant at a value around $1.46{\cdot}10^{-7}\,\mathrm{m/s^2}$. Given the constant flight path angle, the acceleration at the beginning of the simulation is close to its overall minimum and increases until shortly before the periapsis. In the time until 40 min after the periapsis the acceleration decreases drastically to then increase to close to the first two attitudes. This trend is somewhat inverted for Nadir pointing. Until shortly before the periapsis the acceleration is in the same regime as for Sun pointing and the real Rosetta attitude. It then decreases rapidly and increases just as fast to decrease again. From its minimum to the end of the simulation the magnitude increases again. The trends of the accelerations have a direct influence on the velocity and the position.

In both Figure 7.14 and 7.15 for the velocity and position difference, respectively two distinct progressions can be seen. The first is the mostly overlapping progression for the Nadir-pointing, Sun-pointing and real Rosetta attitude. The acting direction of the solar radiation pressure is away from the Sun and due to the relative positions of the Sun, Earth and spacecraft, this leads to a smaller velocity of the perturbed simulation up to the periap-

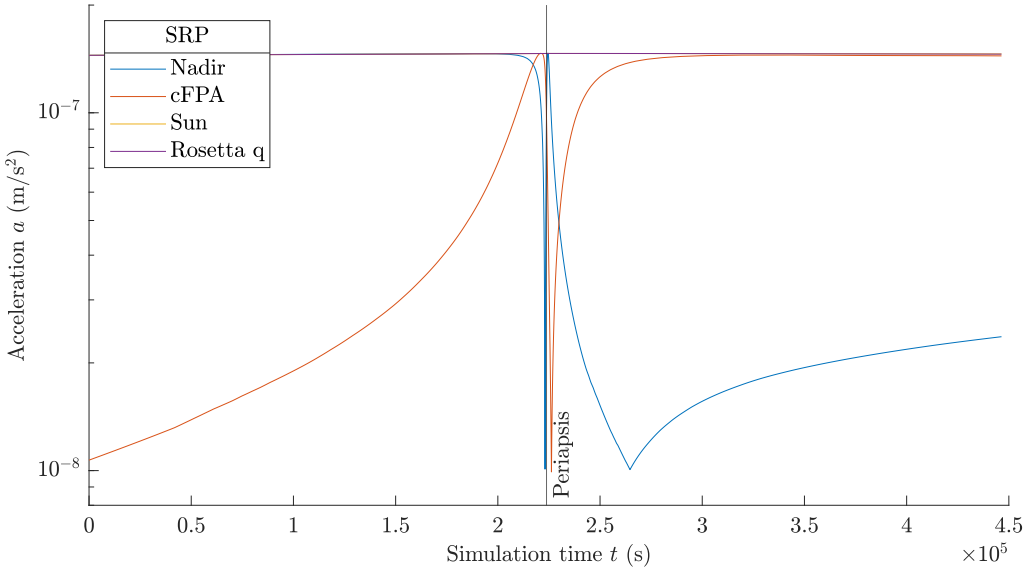

Figure 7.13: *The magnitude of the acceleration due to the solar radiation pressure for four different attitudes plotted over the simulation duration.*

sis. Around the periapsis is a dip in the velocity difference which indicates a switch of the velocity difference sign. From the minimum until the next minimum, the velocity of the perturbed trajectory is higher. From there till the end of the simulation the difference is negative again. Because the accelerations are similar up to the periapsis both the velocity and position change for all three in the same manner. After the periapsis the Sun-pointing and real Rosetta graphs stay close together because the acceleration is also not differing significantly. The graph for the Nadir-pointing attitude then starts to diverge from the other two as the acceleration is significantly lower. The second graph is for the constant flight path angle. Before the periapsis the acceleration is lower than for the other three attitudes, that is why the velocity and position differences are both smaller as well. After the periapsis the gap between the two graphs in the position difference is decreasing but not closed. The nearly constant acceleration of $1.46{\cdot}10^{-7}\,\mathrm{m/s^2}$ for Sun pointing leads to a maximum position difference to the baseline simulation of 11.9 km.

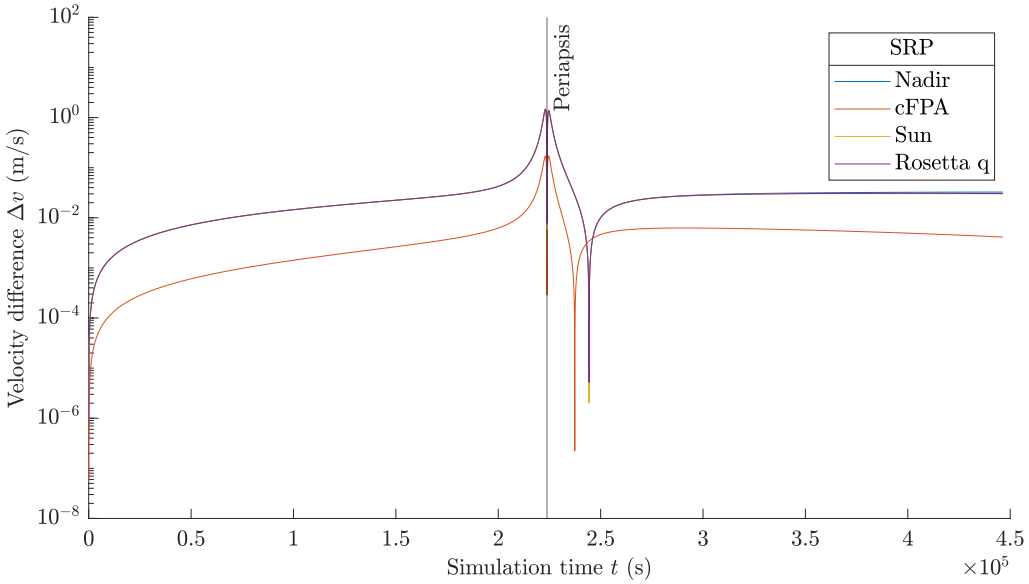

Figure 7.14: *The velocity difference to the baseline simulation due to the solar radiation pressure for four different attitudes plotted over the simulation duration.*

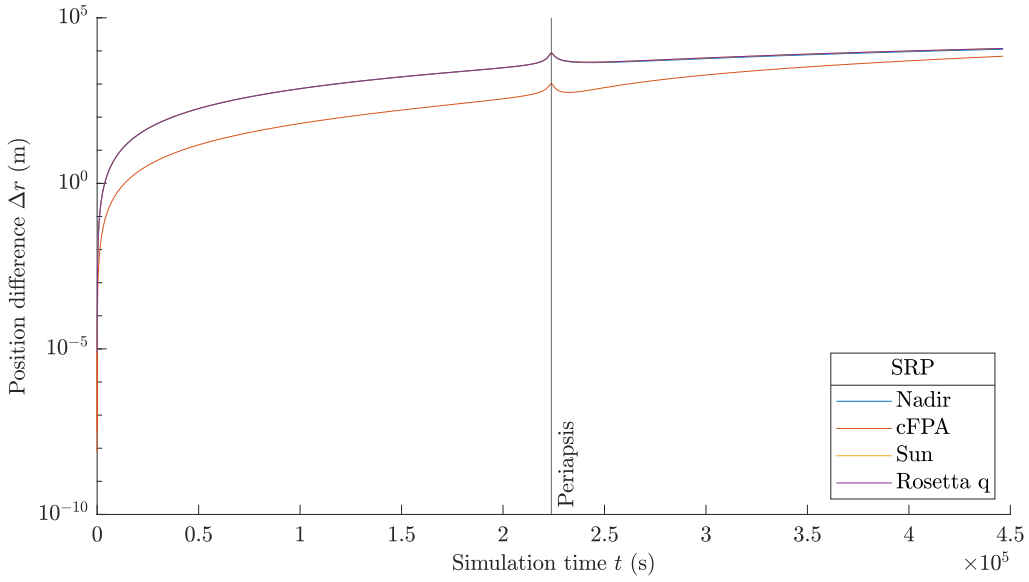

Figure 7.15: *The position difference to the baseline simulation due to the solar radiation pressure for four different attitudes plotted over the simulation duration.*

7.4.2.3 Thermal Radiation Pressure

The acceleration due to the thermal radiation pressure is closely coupled with the solar radiation pressure. As stated before, the fraction of Earth albedo and infrared had to be omitted in the simulations due to computational limitations. The thermal radiation pressure is therefore a certain percentage of the solar radiation pressure depending on the absorption coefficient of the incident surface elements and the emissivity of all surface elements. Figure 7.16 shows the acceleration due to the thermal radiation pressure for the whole simulation duration. It can be seen that the acceleration due to the thermal radiation follows the same trends as the solar radiation pressure for the respective attitudes. The Figures C.1 and C.2, picturing the exact ve-

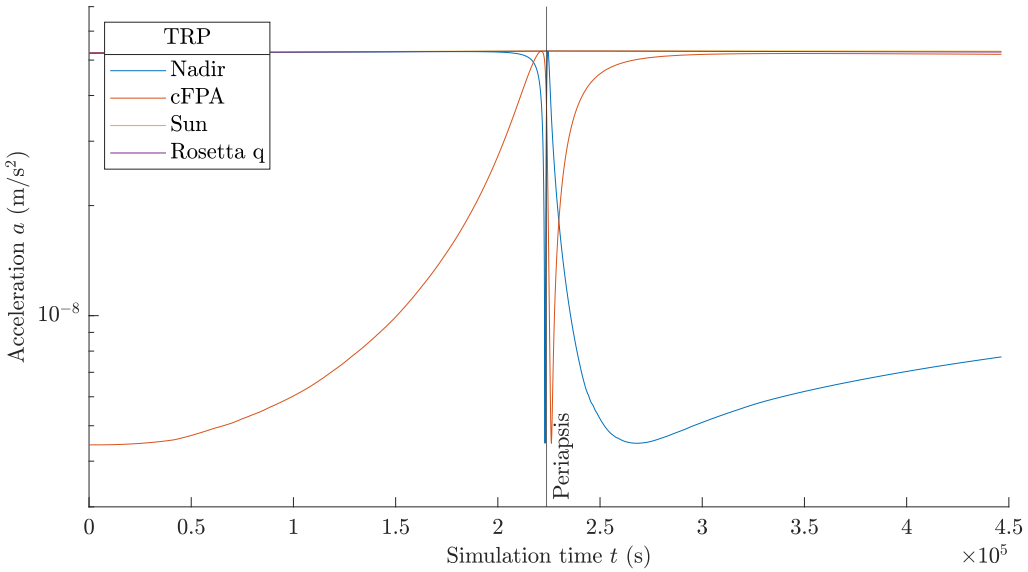

Figure 7.16: *The magnitude of the acceleration due to the thermal radiation pressure for four different attitudes over the simulation duration.*

locity and position differences for the thermal radiation pressure, are listed in the Appendix C due to their similarity to Figure 7.14 and 7.15.
The acceleration of the thermal radiation pressure varies between 31 % and 45 % of the acceleration due to the solar radiation pressure. For the Sun-pointing and real Rosetta trajectory, the percentage stays almost constant at 36 %. The value of 36 % reoccurs in the relation of solar radiation and thermal radiation pressure for the velocity and position difference of Sun-pointing and real Rosetta attitude. The relation of the acceleration for Nadir pointing and the constant flight path angle is not evident in the respective Δv and

Δr plots. For example, the position difference for the constant flight path angle reaches values of up to 108 % of the solar radiation.

7.4.2.4 Earth Albedo and Infrared

Earth albedo and infrared are two distinct accelerations with different sources but are treated as one in this master thesis. The albedo is the on Earth reflected solar radiation and dependent on the longitude and latitude of the spacecraft position above Earth as well as the date of the flyover. The infrared is a radiation of Earth ruled by Planck's law and the temperature of Earth. Therefore both perturbations have the same origin and act in the same direction. The magnitude of both phenomena are pictured in Figure 7.17. The graphs are plotted in a logarithmic scale over the duration of the simulation.
Again, two distinct progressions can be seen before the periapsis in both subfigures. One for Nadir pointing, Sun pointing and the real Rosetta attitude as they are aligned very closely and the second for the constant flight path angle. After the periapsis four individual graphs are visible. In the albedo figure, the noise is a product of the calculation procedure and the level of the acceleration is higher after the periapsis than before. The general trend visible in both acceleration figures is that the acceleration increases with the decreasing distance to Earth. The acceleration is therefore highest at the periapsis, where the distance to Earth is smallest. In the infrared figure the graphs are more mirrored at the periapsis line. The graphs for the Sun-pointing and real Rosetta attitude are staying close together even after the periapsis. Overall, the accelerations span a range of five orders of magnitude and the highest acceleration is detected for Nadir pointing for both, Earth albedo and infrared.
Figure 7.18 and 7.19 show the velocity and position difference due to the Earth albedo and infrared plotted in a logarithmic scale over the simulation duration. Reoccurring is again the distinction of two graphs with the same distribution as for the acceleration. The perturbation due to albedo and infrared leads to a maximum velocity difference of $4.5{\cdot}10^{-5}$ m/s and 7.2 m for the position difference, both for Nadir pointing.

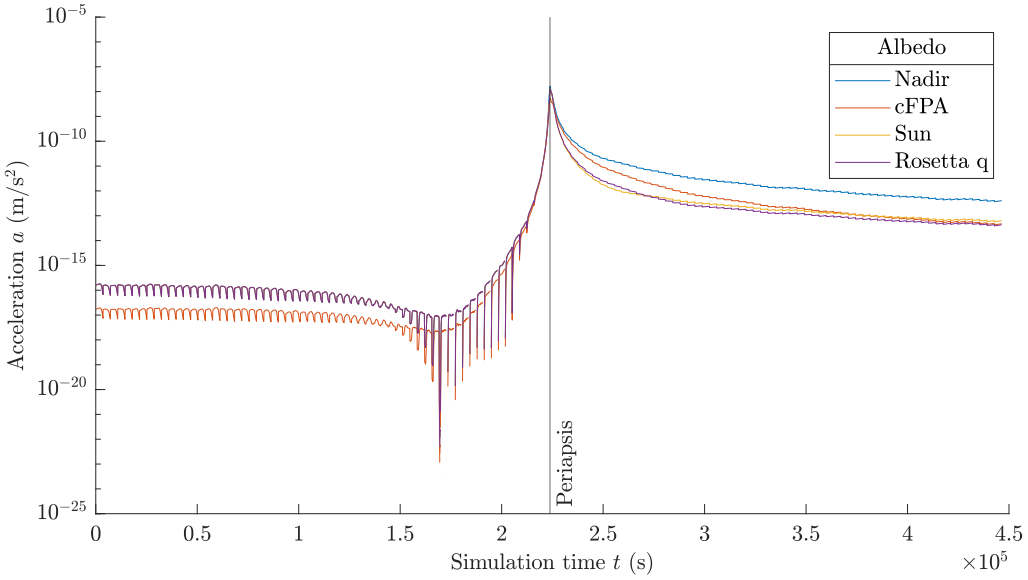

(a) *Earth albedo*

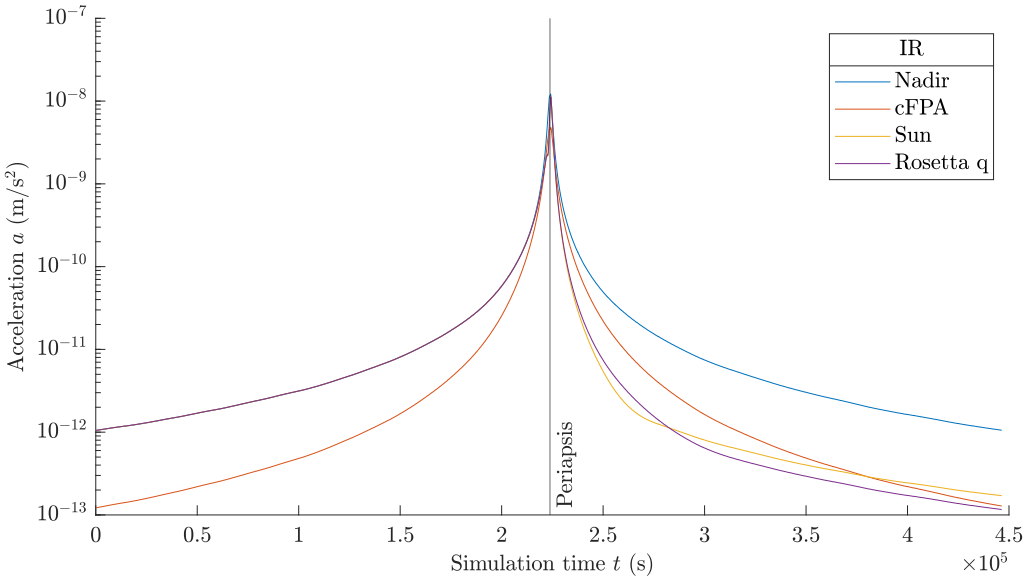

(b) *Earth infrared*

Figure 7.17: *The magnitude of the acceleration due to Earth albedo and infrared for four different attitudes over the simulation duration.*

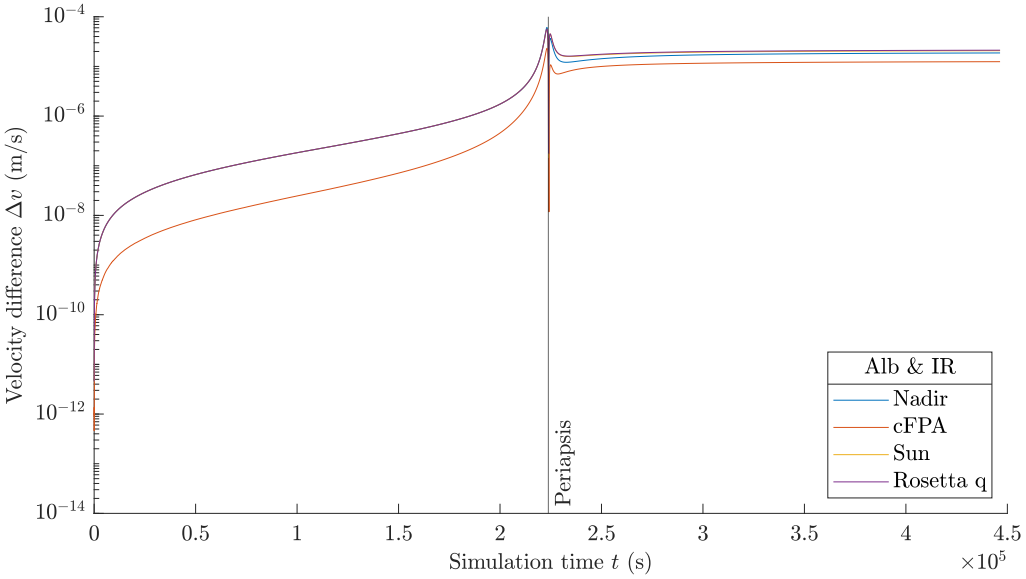

Figure 7.18: *The velocity difference to the baseline simulation due to albedo and infrared for four different attitudes plotted over the simulation duration.*

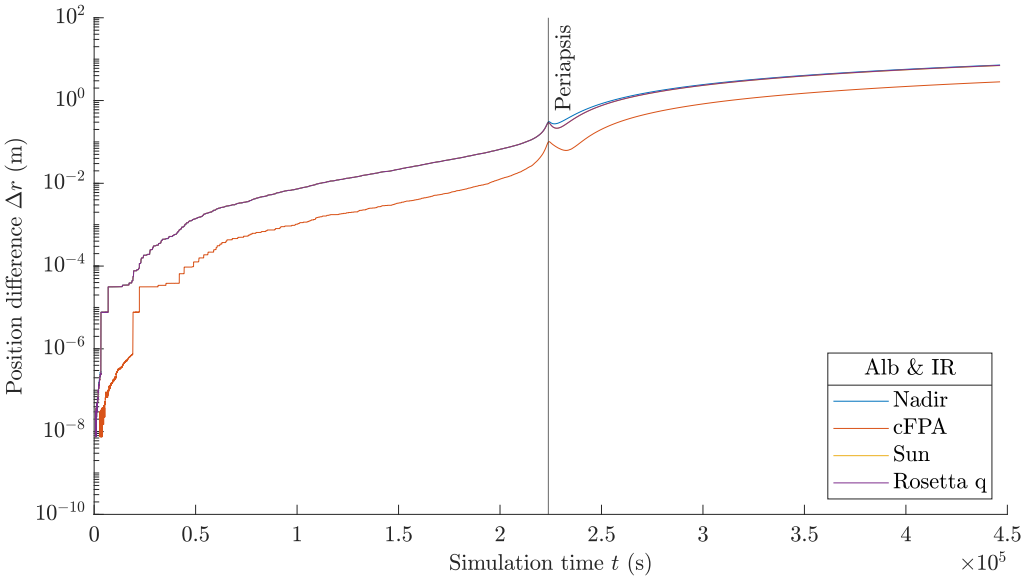

Figure 7.19: *The position difference to the baseline simulation due to albedo and infrared for four different attitudes plotted over the simulation duration.*

7.4.3 Discussion

The simulation of the atmospheric drag gives the first indication of the impact of the different attitudes. The similarity in the acceleration (see Figure 7.11) of Sun pointing, the real Rosetta attitude and the constant flight path angle before the periapsis indicates that the area perpendicular to the relative velocity vector is similar in size during this time. After the periapsis, Sun-pointing and Rosetta stay similar but diverge from the acceleration for cFPA. For the Nadir-pointing attitude the local minimum indicates a rapid decrease of the cross-section area which could be caused by the solar array normal vector turning to 90° with respect to the relative velocity vector. The general increase of the acceleration towards the periapsis is the product of higher density and velocity at smaller distances to Earth. The magnitude of the velocity and position difference indicates that the atmospheric drag can be neglected without significant precision losses. Brown [8, p. 271f.] states that for spacecraft in Earth orbits below 1000 km the drag perturbation needs to be considered as it leads over time to orbital decay. In the case of Rosetta and the simulated trajectories the minimum altitude is about the double of the stated boundary and the time close to Earth is short as well (regard the duration below 10000 km as stated in Section 7.4.2.1). This supports the decision of omitting the atmospheric drag in the comparison to the real Rosetta trajectory.
The acceleration plots for the atmospheric drag alone do not allow a statement about the actual differences of the attitudes because the direction of the acceleration is changing with the relative velocity vector. The acceleration plots of the solar radiation pressure (see Figure 7.13) give additional information about the attitude. The axes of the spacecraft are orientated constantly with respect to the Sun for Sun pointing. Because the real Rosetta attitude delivers almost identical acceleration values, it can be assumed that the spacecraft is oriented in the same direction. The similar behaviour of Sun-pointing and real Rosetta attitude can be observed for all non-gravitational perturbations. The Nadir pointing graph for the solar radiation pressure indicates that the Sun and Earth are located in the same direction seen from the spacecraft before the gravity assist as the accelerations match during this time. After the periapsis the direction of Earth and the Sun seen from the spacecraft diverge, which leads to the distinguishable graphs in the acceleration figure. For both, the Nadir pointing and constant flight path angle the graphs indicate that the attitude towards the Sun changes drastically based on the quick succession of local minima and maxima. The positions of spacecraft and Earth in the heliocentric frame are pictured in Figure 7.20 and the vectors indicate the direction of the Sun. This figure supports the

statements about the relative positions of the Sun, Earth and SC before and after the periapsis.

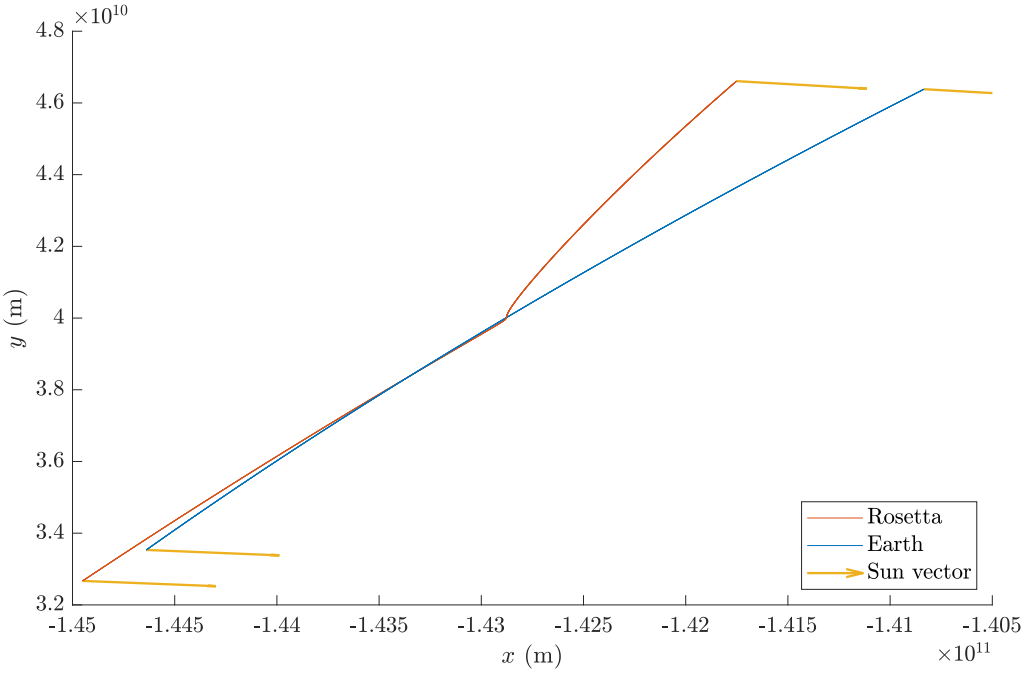

Figure 7.20: *The heliocentric flight path of Rosetta and Earth. The direction of the Sun is indicated by yellow vectors. Direction of flight is from north-east to south-west. LoS along -z-axis.*

The acceleration graphs of the thermal radiation pressure are similar in terms of the trends to the solar radiation pressure as stated in Section 7.4.2.3. Considering Nadir pointing and the constant flight path angle, the percentages of the accelerations vary over the course of the trajectory. This is attributed to the different absorption coefficients of the spacecraft parts (see Table 4.1) and shadowing of elements by other elements depending on the attitude. When surfaces of the spacecraft that have a higher absorption coefficient are incident with albedo and infrared radiation, the spacecraft temperature and consequently the thermal-radiation acceleration rises. If a larger amount of elements are shadowed by some other structure, the incident area is reduced and therefore the acceleration decreases. These two assumptions are made on the basis that the emission coefficients and surface area of the spacecraft stay constant.
The acceleration for Earth albedo, as shown in Figure 7.17, shows a higher acceleration after the periapsis then before. This is especially evident for Nadir pointing which indicates that this increase is not due to changing attitude

with respect to Earth. Most likely, this trend is induced by the illuminated portion of Earth's surface in the field of view. This is supported by the nearly identical acceleration of Sun and Nadir pointing before periapsis which indicates, similar to the solar-radiation acceleration, that Earth and the Sun are located in the same direction from the satellite (see Figure 7.20). Due to this, the portion of the illuminated surface in the field of view is minor as the Sun is located behind Earth seen from the spacecraft. After the periapsis, the relative positions of the Sun, Earth and spacecraft is drastically different and a greater portion of Earth's surface in the field of view is illuminated. With respect to the negligence of Earth albedo and infrared as an additional source for the thermal radiation, the values of the maximum differences are multiplied with 36 %. The relation of the thermal pressure to the solar radiation pressure, applied to the acceleration due to albedo and infrared gives an estimate of the neglected perturbation. It has to be noted that the absorption coefficient differs for the visible and infrared spectrum, which is omitted in this estimation. The estimate for the velocity and position difference are $1.6{\cdot}10^{-5}$ m/s and 2.6 m, respectively. This yields an acceptable precision loss when again regarding the ten percent threshold of the Flyby Anomaly ($6.7{\cdot}10^{-5}$ m/s).

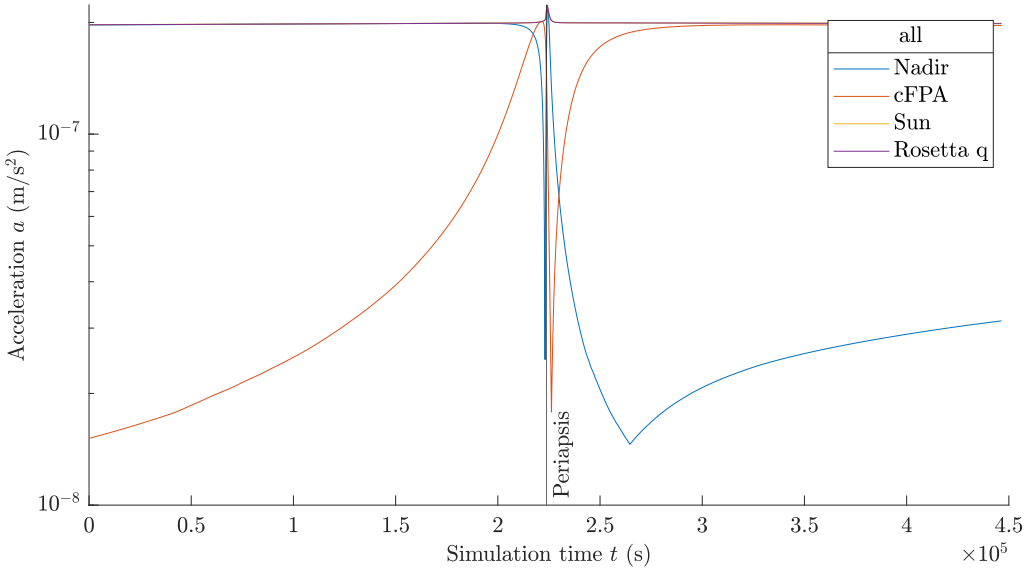

Figure 7.21: *The magnitude of the sum of all non-gravitational perturbations for four different attitudes over the simulation duration.*

With the knowledge from all simulations about the accelerations of each perturbation it can be conducted that the solar radiation pressure has the

greatest influence. Its acceleration is at its highest in the $10^{-7}\,\mathrm{m/s^2}$ range. The progression of the combination of all accelerations during the course of the trajectory is pictured in Figure 7.21, where it can be seen that close to Earth, albedo and infrared also have a distinct part in the acceleration.
The analyses of the individual influence of each perturbation gives a clearer understanding of the accelerations depending on the different attitudes. Three of the four attitudes were chosen for a plausible use-case (Sun-/Nadir-pointing) or to maximize a perturbation (cFPA). The simulations show that depending on the source of the perturbation the attitude with the greatest cross-section area produced the greatest perturbation - constant flight path angle for atmospheric drag, Sun pointing for solar and thermal radiation pressure, Nadir pointing for albedo and infrared. Another deduction is that the real Rosetta trajectory is most likely a Sun-pointing attitude. For the majority of the trajectory no data about the attitude is available but the similarity in the accelerations to the Sun-pointing attitude supports this hypothesis. With a Sun-pointing attitude the spacecraft can produce the necessary electrical power and communication is ensured by a movable high-gain antenna.

7.5 Rosetta Comparison

All prior conducted simulations are done to define the setup for the simulation of Rosetta's trajectory. This setup consists of the following effects and perturbations:

- complete three-body model with
  - spherical harmonics Earth potential field of order and degree 26
  - elastic solid-Earth tide of order four
- third-body perturbations of
  - Mercury
  - Venus
  - Mars
  - Jupiter
  - Saturn
  - Uranus
  - Neptune
  - Moon
- non-gravitational perturbations of
  - solar radiation pressure
  - thermal radiation pressure
  - Earth albedo and infrared

The simulations are performed with the real Rosetta attitude, which is only known for 10 % of the trajectory and the Sun-pointing attitude. The latter was determined to be similar to the real Rosetta attitude in previous simulations. By simulating with the Sun-pointing attitude and comparing to the real Rosetta trajectory it is thought to further support the hypotheses that the actual Rosetta trajectory is Sun pointing. Furthermore, the position and velocity difference are examined more closely to determine the direction of difference and narrow down possible error sources.
The simple comparison of the two simulations to the Rosetta trajectory in terms of the velocity and position difference is pictured in the Appendix in Figure C.3 and C.4, respectively. It shows that both attitudes are nearly identical in their divergence from Rosetta and the maximum differences between the Δv and Δr of both are as small as 3.2 mm/s and 136 m. The position difference to the real Rosetta trajectory is the smallest for the Sun-pointing attitude with 14.6 km. With regard to the orbit radius of Rosetta at that time (945855.7 km), this difference is 0.0016 %, which is infinitesimal small. Nevertheless, the smaller difference for the Sun-pointing attitude further substantiates Sun pointing as the real Rosetta trajectory. Overall, the stepwise extension of the simulation reduced the difference of the simulation and the Rosetta data from 6913 km for the C3BM to 30.6 km for the baseline simulation to a final 14.6 km for the simulation including non-gravitational perturbations and the Sun-pointing attitude.
Figure C.3 shows the velocity difference in the ECI. Considering that the velocity with respect to Earth increases drastically during the approach of Earth and decreases with the same rate after the periapsis (see Figure C.5), the small velocity difference between the simulation and the measurement data could be caused by a slightly displaced spacecraft in the simulation. Meaning, the simulation reaches its closest approach to Earth slightly before or after the real Rosetta spacecraft. This time difference would lead to an earlier or later acceleration and deceleration causing the velocity difference. If the simulation and real Rosetta spacecraft reach their closest approach at the same time, a different distance to Earth and therefore a higher or lower maximum velocity could also be the reason for the velocity difference. To analyse which hypothesis causes the remaining difference the velocity and position differences are examined more closely and the trajectories are compared not only in time but in space as well.
Plotting the velocity difference without the logarithmic scale in Figure 7.22, shows that the velocity difference is positive before the periapsis, falls in the negative after periapsis and increases again to a slightly positive difference. In Figure 7.23, the position difference is split into its vector components and plotted over the simulation duration. The relative position vector between

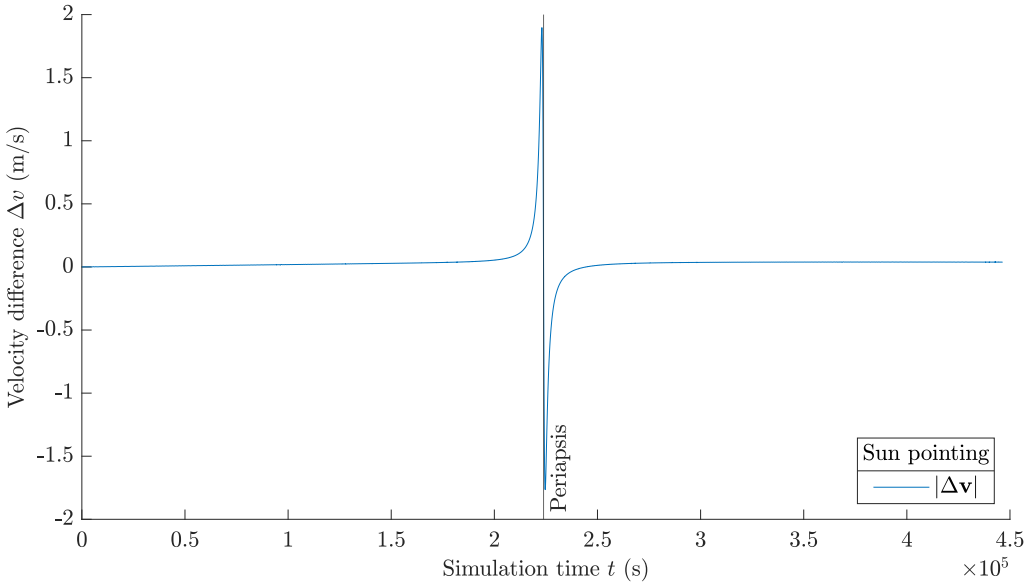

Figure 7.22: *The velocity difference to real Rosetta for Sun pointing plotted over the simulation duration.*

the simulation and Rosetta points from Rosetta to the simulation. With the vector orientation and the plot of the trajectory in the ECI frame (see Figure 6.7), Figure 7.23 can be interpreted. Most of the position difference before the periapsis is in the positive x-direction with a smaller part in the negative y-direction. In z-direction the smallest difference occurs. This changes after the periapsis. The greatest portion of the difference is now in negative y-direction with both a smaller difference in negative x and z-direction. Regarding the trajectory plot in Figure 6.7, from both the positive difference in x before and the negative difference in y-direction after the periapsis, it can be derived that most of the position difference is in direction of the spacecraft's motion. This statement holds better for the approach of Earth than for the departure, as the motion of the spacecraft is more along the x-axis before then along the y-axis after the periapsis. A more precise assertion is not achievable with the available data.
Additionally, the altitude at the closest approach of the simulation is compared with the real Rosetta data and the time of the periapsis is analysed. Figure 7.24 shows the distance to Earth in a time frame of 50 min in which Rosetta is below an altitude of 7000 km. The time of the periapsis of both trajectories is marked in the figure and shows that the simulation reaches its closest approach 40 s before Rosetta. The different time of the periapsis means that the spacecraft flies over different portions of Earth and expe-

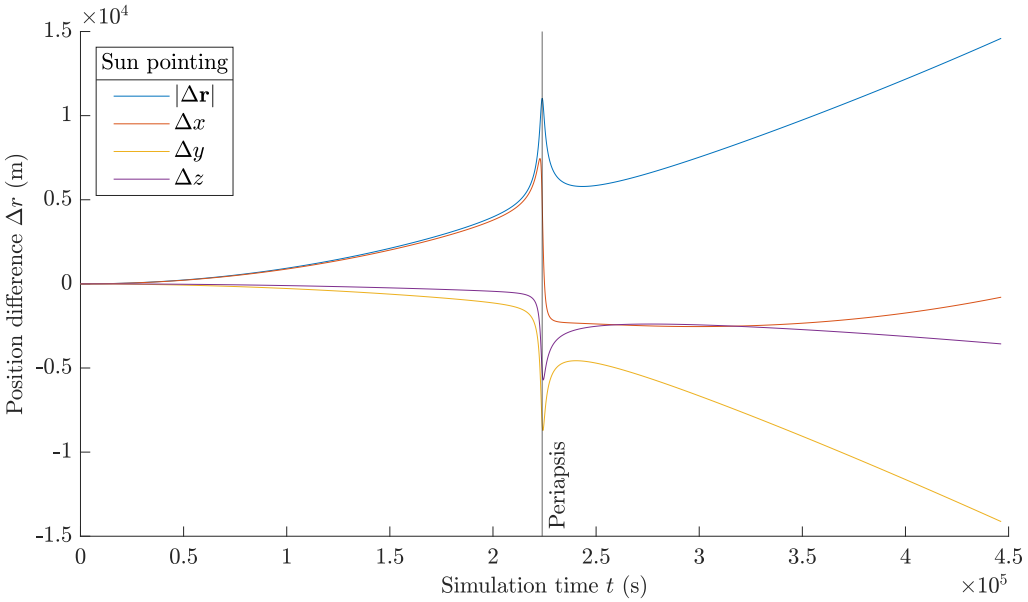

Figure 7.23: *The position difference to real Rosetta for Sun pointing plotted over the simulation duration. Dedicated graphs for the Euclidean norm and every vector component.*

riences distinct gravitational attraction. For a potential field of order 26 including a tide model this time difference might noticeably change the trajectory.

Not evident in these graphs is the altitude difference at the closest point to Earth, which is 1.47 km closer for the simulation. This could be caused by the different gravitational acceleration of Earth during the simulation. The combination of both, the timing and the altitude difference might be the cause of the remaining difference between the simulation and the real trajectory.

In the last part of this master thesis a short survey is done to explore the behaviour of the simulation if the initial velocity is slightly changed or the orientation of Earth is different during the gravity assist. Only a general estimation about the behaviour of the simulation with respect to the applied changes can be done. The task of further minimizing the position difference of the simulation to the real Rosetta data is an optimization problem with numerous unknown dependencies.

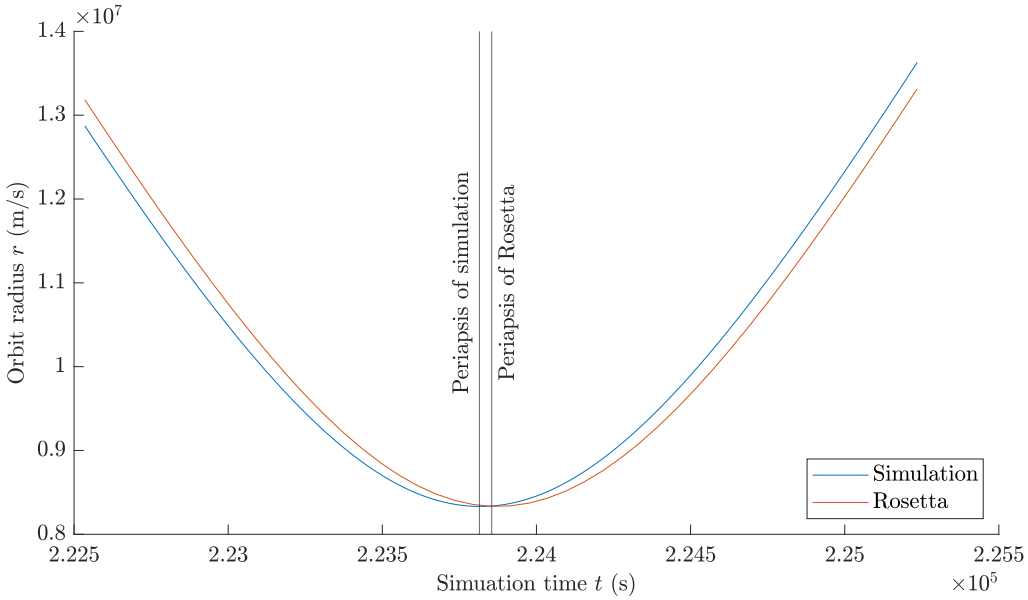

Figure 7.24: *The orbit radius of the simulation and Rosetta plotted over the duration Rosetta is below an altitude of 7000 km.*

7.5.1 Manual Simulation Adjustment

One result of the comparison of the simulated trajectory to the real Rosetta trajectory is the discovery of the time difference between the two periapsis. Figure C.3 shows that the velocity difference before the periapsis is in the range of $1{\cdot}10^{-2}$ m/s for the most time. According to this, the initial velocity is reduced to 99.9995 % of its magnitude. The orientation of the vector is kept constant in the following way:

$$\boldsymbol{v}_{i,new} = \boldsymbol{v}_i - \boldsymbol{v}_i \cdot 0.000005. \tag{7.6}$$

This procedure reduces the initial velocity about $1.99{\cdot}10^{-2}$ m/s and changed the trajectory as follows. The velocity difference is pictured in Figure 7.25, where it can be see that the maximum velocity difference is decreased to well below the m/s mark. The difference starts in the negative with the value of the reduction and increases to a positive difference before the periapsis. After the periapsis the velocity of the simulation stays higher than the velocity of Rosetta.
In the position difference in Figure 7.26, the velocity reduction has the following impact. The difference in x-direction is the highest of the three vector components during the whole trajectory. Before the periapsis, the difference increases and decreases, which can be assigned to the velocity difference

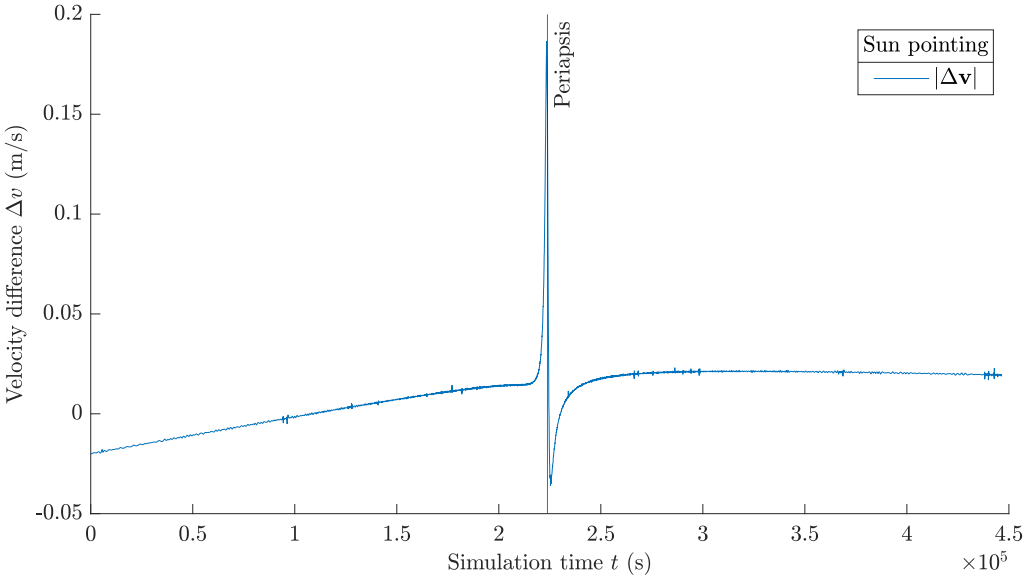

Figure 7.25: *The velocity difference of the simulation with decreased initial velocity and Rosetta plotted over the simulation duration.*

increasing from a negative to a positive value. After the periapsis, the position also diverges in z-direction which was not the case before the periapsis. Overall, the position difference could be reduced to a maximum of 8.62 km through the velocity reduction. The desired effect of aligning the closest approach of the simulation with Rosetta is not achieved as they remain 35 s apart.

The second conclusion from the Rosetta comparison is that due to the position offset of the trajectory and the time offset of the closest approach the spacecraft flies over different parts of Earth and experiences different accelerations. To analyse the influence of a different part of Earth, the NHPS has to be adapted again. An option for a time offset is introduced to the *core parameters*. This offset manipulates the transformation between the ECI and the ECEF. The transformation between these two frames is described in Section 2.3.5.3 and is composed out of three major rotations. One of those rotations is the rotation of Earth about its pole axis. This rotation is time dependent and is manipulated with the time offset Δt to virtually alter the orientation of Earth. By this method, it is pretended that for example the spacecraft is some time later and Earth has rotated further without changing the position of any member of the simulation. According to the findings the time offset is set to 40 s and the effects of a positive and negative offset are examined.

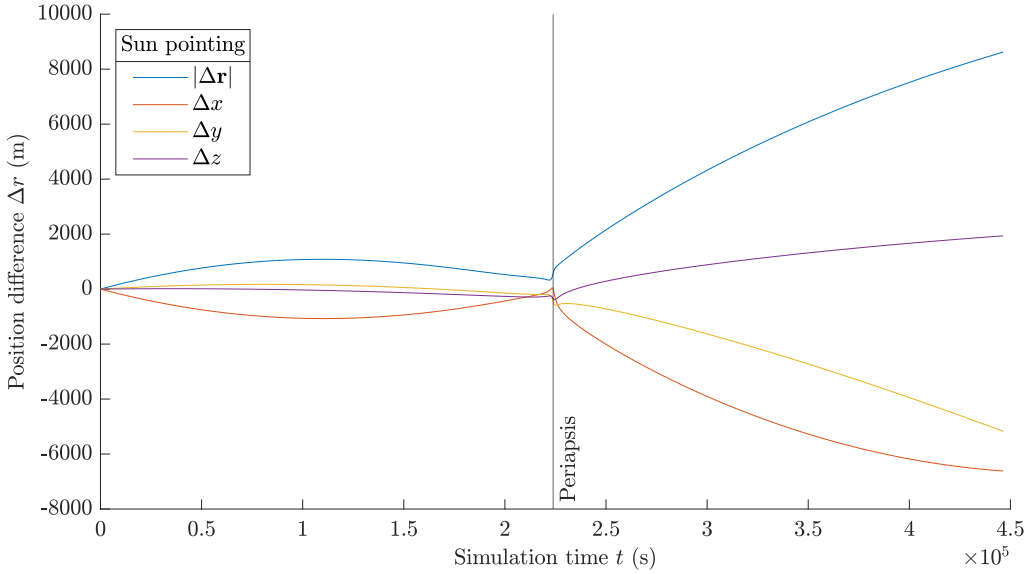

Figure 7.26: *The position difference of the simulation with decreased initial velocity and Rosetta plotted over the simulation duration.*

The here presented results are calculated between the simulations with an artificially rotated Earth and the native simulation. The differences due to the offset is orders of magnitude smaller than the remaining difference of the native simulation and the real Rosetta data and this comparison is auxiliary for the clarity of the graphs. Due to the magnitude of the effect, only the position vectors are compared. In Figure 7.27, the effect of the rotated Earth on the trajectory is pictured over the whole simulation duration. Only close to the periapsis does the different Earth orientation have an on the trajectory. For the most part of the first half of the simulation no difference is detectable. Around the periapsis a difference occurs, which is then propagated till the end of the simulation. The maximum difference is for both offsets ca. 4.8 m. The progression of the difference close to the periapsis cannot be described from this figure as it happens in a short duration with respect to the overall simulation duration. Figure 7.28 shows three graphs, one for each vector component. Each graph is plotted over the duration the spacecraft is below an altitude of 15000 km to show the noticeable differences around the periapsis. The detailed view of the position difference reveals that its direction is reversed for the different offsets. For each vector component the difference is more or less mirrored at the time axis. This is not evident in Figure 7.27 where only the magnitude of the difference can be seen. The undulations of the graphs are limited to a short time frame around the periapsis and the re-

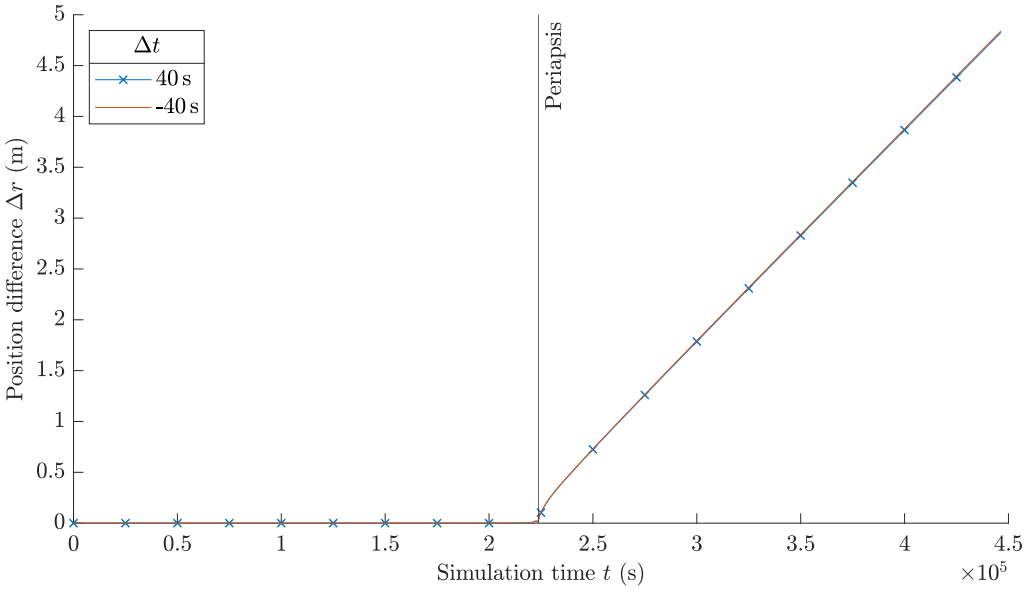

Figure 7.27: *The position difference of the simulation with artificially rotated Earth and the native simulation plotted over the simulation duration.*

sulting differences only proceed over the remaining course of the simulation.

7.5.2 Discussion

According to the velocity graphs (Figure C.3 and 7.25), the velocity of Rosetta changes with a different rate than the velocity of the simulation. This is evident by the fast increase in the beginning of the simulation in Figure C.3 and the trend of the difference before the periapsis in Figure 7.25. Even though the initial velocity was reduced for the simulation, the difference becomes positive. The varying velocity between the two could be caused by an incorrectly modelled perturbation, a thrust of Rosetta or the precision of the Horizons data, which is not known. Regarding the non-gravitational perturbations, the solar radiation pressure has the greatest influence and its description involves parameters with a high uncertainty. During the course of an interplanetary mission the surface properties change drastically but for this master thesis the assumptions do not include degradation of any form. The effect of different surface properties is therefore unknown and a possible error source. A thrusting manoeuvre of Rosetta is another plausible error source as deep space manoeuvres or orbit corrections during the approach of a planet are common techniques.

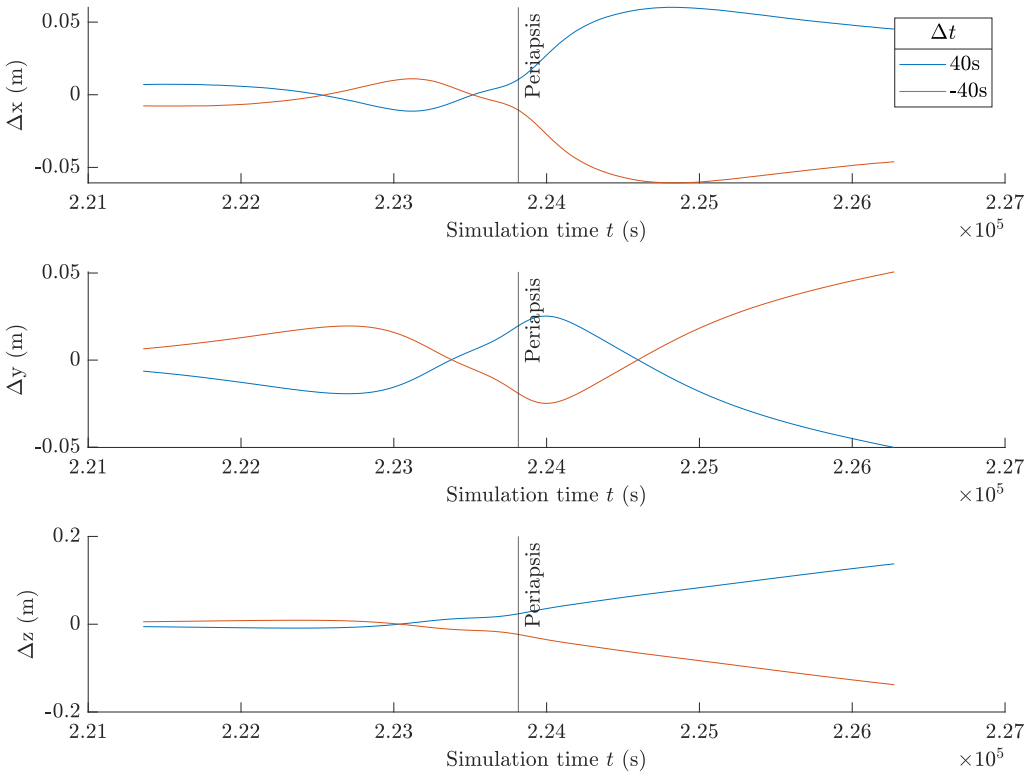

Figure 7.28: *The difference for every component of the position vector of the simulation with artificially rotated Earth and the native simulation plotted over the simulation duration.*

It is important to note that the time offset and the altitude difference of the closest approach could also be the result of the sample rate of the Rosetta data. The shortest interval available at JPL Horizons [53] is 60 s and the actual closest approach of Rosetta could be at times between sample points. Both the time offset for the slowed down and native simulation are smaller than the Rosetta sample rate.
The results from the simulation with the artificially rotated Earth clearly show that a different orientation of Earth is not the cause of the 14.6 km position difference left between the simulation and Rosetta. But it shows the precision of the simulation tool. In the previous chapter the position difference is stated as a fraction of the distance of the spacecraft to Earth with 0.0016 %. Doing the same for the position difference observed in this analysis yields $5.1 \cdot 10^{-7}$ %. Additionally, through these simulations a rough effect of the maximum and minimum distribution of the SHM can be examined. The opposite signs of the differences indicate that the trajectories with the

rotated Earth are either deflected by a greater or smaller angle. The time offset of 40 s leads to a stronger deflected trajectory and the negative offset to a less deflected one. Consequently, the spacecraft experiences a stronger gravitational acceleration for the positive time offset.

7.6 Concluding Discussion

The influence of the studied perturbations in terms of the position difference is set in relation to the gravitational effects in Table 7.2. The influence of the third bodies is by far the most influential addition to the simulation setup. Then, solar and radiation pressure follow with differences in the kilometre range. Albedo, IR and atmospheric drag have the smallest effect on the trajectory. The values for the non-gravitational perturbations are given for the Sun-pointing attitude. As stated before, the maximum velocity and position

Table 7.2: *The influence of various effects in terms of a position difference on the simulation of the Rosetta trajectory.*

Effect	Δr **(m)**
third bodies	6850000
solar radiation	11900
thermal radiation	4310
solid-Earth tide	3200
SHM order	22.6
albedo & IR	7.0
atmospheric drag	0.3

differences of the simulation to the Rosetta data are 1.8 m/s and 14.6 km, respectively. As a percentage of the velocity and position vector magnitudes this reads as 0.0002 % and 0.0016 %, respectively. This indicates the precision of the simulation with respect to the Rosetta data obtained from the Horizon website [53]. Due to the circumstance that the closest approach of the spacecraft can not be tracked, a fitting procedure is used to match the pre- and post-encounter measurements. This fit includes the anomalous velocity change. [57]
To determine if one of the non-gravitational perturbations is a possible source of the anomaly, the velocity difference due to the perturbations at the peri-

apsis is examined. The values of the Δv of each perturbation can be found in Table 7.3.

Table 7.3: *The velocity difference due to the non-gravitational perturbations at the periapsis with respect to the baseline simulation.*

Perturbation	Δv **(m/s)**
solar radiation	-0.11
thermal radiation	-0.04
albedo & IR	$-9.87 \cdot 10^{-6}$
atmospheric drag	$-2.36 \cdot 10^{-7}$

First, it has to be noted that the Flyby Anomaly for the first Rosetta Flyby is determined as a positive instantaneous velocity change [55]. Unfortunately, all perturbations cause a negative velocity difference at periapsis. Due to the magnitude of the difference, albedo and infrared as well as atmospheric drag can be ruled out. The effect of these two perturbations is smaller than 1 % of the Flyby Anomaly and an error which changes the effect to close the magnitude of the anomaly is assumed highly unrealistic. This is different for the solar and thermal radiation pressure. For these two perturbations an error of below 2 %, respectively 1 % could account for a change in the velocity difference of magnitude of the Flyby Anomaly. According to the omitted degradation of the radiation surface properties, an error of this scale is highly plausible.
These findings align closely with the results of the sensitivity study of Jouannic et al. [37]. They also obtained variations of the solar radiation pressure in the range of the anomaly for very small changes to the surface radiation properties. By contrast, Lämmerzahl et al. ruled out every perturbation as a cause of the Flyby Analysis based on an estimated acceleration. They compared the acceleration due to the different space-environmental effects to an acceleration that is needed for the observed anomaly. Based on the too little acceleration of every perturbation, all effects were discarded. The results of this thesis clearly contradicts their estimations for the solar radiation pressure; the thermal radiation pressure was not considered in their study. Lämmerzahl et al. estimate the acceleration due to solar radiation in the range of 10^{-9} m/s, which is two OoM smaller than the acceleration of $1.46 \cdot 10^{-7}$ obtained in this study. The acceleration Lämmerzahl et al. estimate, necessary to account for the Flyby anomaly is of order 10^{-4}. Even though the solar radiation pressure asserts a smaller acceleration on the spacecraft the

effect is of higher magnitude than the anomaly. This indicates that the orbit propagation and simulating of the various effect for an extended duration yields more precise results.

Chapter 8

Conclusion

The model evaluation showed satisfactory results for the investigated simulation cases. Confirming that the adaption of the HPS was successful and the chosen equations of motion and coordinate transformations work as desired in the simulation of interplanetary trajectories. The precision of elliptic orbits around Earth simulated with the NHPS in the heliocentric ecliptic frame is not worse than 0.02 % compared to the results of the HPS. The difference between the HPS and NHPS simulations is the consideration of the motion of Earth around the Sun in the NHPS.
The behaviour of the trajectory differences for interplanetary trajectories led to the conclusion that numerical errors propagate during the simulation and distort the results. To minimize this numerical error, a scaling scheme was developed which further reduced the differences between the NHPS and HPS simulations in Earth orbits and an exemplary interplanetary trajectory. Unfortunately, the application of the scaling scheme in the remodelling of the actual flown trajectory of Rosetta showed no ambiguous improvement of the results. A revision of the scaling and change of calculations did not lead to conclusively enhanced precision of the simulation. Consequently, the scaling was disregarded for all further simulations.
In retrospective, the position difference for the interplanetary trajectory of 0.9 % is acceptable from the author's point of view and the observed plane change is a sometimes desired effect of a gravity assist.
Comparing the velocity change of simulated Earth-gravity assists to the theoretical Δv value showed that the NHPS models the heliocentric energy transfer of gravity assists in adequate precision. Based on the variation of the initial position, closer to or farther away from Earth, it can be seen that a gravity assist is more precisely modelled the closer the spacecraft states are evaluated to the infinity of the trajectory.

Through the study of additional gravitational effects and non-gravitational perturbations, the simulation setup is updated with the adequate effects for the analysis of the simulation of Rosetta's trajectory. The threshold for the inclusion is set to ten percent of the Flyby Anomaly of Rosetta ($6.7 \cdot 10^{-5}$ m/s). Not only the influences of external perturbations are examined but also the dependency of the spacecraft's attitude on the influence of the perturbations. Sorting the gravitational effects and non-gravitational perturbations by the magnitude of the change in the trajectory, Table 7.2 is obtained. The inclusion of all major solar-system bodies except Pluto has by far the greatest influence on the trajectory, followed by the solar radiation and thermal radiation pressure. For the latter two, the attitude of the spacecraft has an unsurprising influence on the magnitude of the perturbation. This dependency can also be observed for the other non-gravitational perturbations. From four Earth tide models only one has an effect worth including in the Rosetta simulations. The literature research revealed the sensitivity of Gravity-Assist simulations on the Spherical Harmonics Earth Potential Filed up to order and degree 100. The study in this master thesis concerning the order led to the justified truncation of the SHM at order 26. The results for the atmospheric drag show that its influence is negligible as the trajectory of Rosetta passes Earth at an altitude above 1954 km.
For most of the non-gravitational perturbations, a general direction of the perturbation can be stated. They are either acting away from its source or against the velocity vector of the spacecraft relative to the atmosphere (for the atmospheric drag). For the thermal radiation no such statement is made. The direction of this acceleration depends on factors like the radiation surface properties of the different spacecraft parts and the attitude of the spacecraft. To detect the effective direction more studies are necessary.
The simulations with different attitudes showed that the magnitude of the non-gravitational perturbations strongly depend on the attitude. The solar and thermal radiation pressure are at a maximum for a Sun-pointing attitude. For Earth albedo and infrared the highest acceleration is obtained in combination with Nadir pointing. The atmospheric drag is the highest for a flight path angle that aligns the maximum cross-section area of the spacecraft perpendicular to the relative velocity vector. In general, the perturbation is the largest if the maximum cross-section area is oriented perpendicular to the direction of the perturbation. Additionally, it is observed that the real Rosetta attitude, which is only known for about 10 % of the simulation duration, closely aligns with the Sun-pointing attitude. If the last known quaternion of Rosetta is kept constant for the remaining simulation duration the angular difference to Sun pointing is only 3.13° at the last simulation time step.
The comparison of the simulation, including all relevant perturbations and

utilizing the Sun-pointing attitude, to the real Rosetta data [53] revealed a remaining position difference of 14.6 km at the last time step and a maximum velocity difference of 1.8 m/s shortly before the periapsis. Based on the discovery of a time and position offset of the periapsis two manual simulation adaptions are made to assess the general behaviour of the simulation to these adaptions. First, the initial velocity vector of the simulation is decreased to 99.9995 % to reduce the velocity difference of the simulation and the real data. The percentage is chosen according to the magnitude of the velocity difference during most of the trajectory leading up to the periapsis. This adaption leads to a further decrease in both the maximum velocity and position difference, but the more important discovery is the progression of the velocity difference. Even though the initial velocity of the simulation is smaller than the real Rosetta data at the initial position, the velocity increases to a higher value than the real data until the periapsis. The reason for this is unknown but could be ascribed to an orbit manoeuvre of Rosetta, an incorrectly modelled perturbation or the uncertainty of the Horizons data.
Second, the effect of the position difference of the spacecraft to Earth in the time around the periapsis is evaluated. Could the different part of Earth which the spacecraft flies over lead to a different trajectory due to its different gravitational acceleration? The time difference of the periapsis between the simulation and the real data is 40 s. Therefore, the orientation of Earth is artificially rotated by this value in a further simulation. The artificial rotation is done by manipulating the coordinate transformation between the ECI and the ECEF. The trajectory is only altered due to the different orientation by a maximum of 4.8 m and is therefore dismissed as the cause of the remaining difference. The essence of this manual adaption is that a differently oriented Earth changes the deflection angle of the trajectory. Due to the segmentation of Earth's potential field in minima and maxima through the spherical harmonic development, a different oriented Earth increases or decreases the gravitational acceleration with respect to the unchanged orientation.

From the non-gravitational-perturbation study, non of the perturbations can be clearly determined as the cause of the Flyby Anomaly. For the comparison of the results to the Flyby Anomaly the magnitude of velocity difference at the periapsis as well as the sign of the difference is important. These differences are given in Table 7.3.
The Flyby Anomaly for the first Rosetta Flyby at Earth is detected as a positive instantaneous velocity change of 0.00067 m/s. The solar and thermal radiation lead to a velocity difference higher than the anomaly but with the wrong sign. Albedo, infrared and the atmospheric drag are ruled out as a cause by both the magnitude and sign of the velocity difference.

However, every perturbation model contains errors. Assuming an error of below 2 % in the thermal-radiation model could already lead to a variation of the velocity difference very similar to the Flyby Anomaly. Due to the strong dependency of the thermal radiation pressure on the radiation surface properties of the different parts of the spacecraft, an incorrect representation of this effect is highly possible. For the solar radiation pressure an error of below 1 % in the model could account for the anomalous velocity change. This aligns closely with the findings of Jouannic et al. [37], who found a high sensitivity to the radiation surface properties, which are not exactly known due to degradation as stated before.
Lämmerzahl et al. [16] estimated the acceleration necessary to account for the anomalous velocity change and dismissed several space environmental effects based on the magnitude of their acceleration. The here obtained accelerations for solar and thermal radiation are higher than the value of Lämmerzahl et al. but still smaller than the apparently necessary acceleration required to obtain the Flyby Anomaly. Nevertheless, they result in larger velocity changes than the Flyby Anomaly. This discrepancy between two studies of the Flyby Anomaly aligns with the failure of research groups of conclusively assigning the Flyby Anomaly to a standard physical or relativistic effect [3, 4] or even more revolutionary physics [5].
In conclusion, a modelling error of a non-gravitational perturbation can result in a velocity change at the periapsis similar to the Flyby Anomaly. The remaining position difference of the simulation and the Rosetta data of 0.0016 % shows the achievable precision of the new HPS. It can be said that the new HPS is a suitable tool for the simulation of interplanetary trajectories and the further study of non-gravitational perturbations.

8.1 Outlook

Following this master thesis, several further studies can be conducted. For this thesis, only accelerations are considered while the HPS is capable of calculating additional perturbative effects. For example torques due to eccentric pressure points or gravitational gradients. Staying with accelerations, the dependencies of the perturbations are not nearly covered by only regarding different attitudes. The radiation perturbations, like solar radiation and Earth albedo and infrared strongly depend on the surface radiation properties. The absorption and reflection coefficients are afflicted with high uncertainties due to the environmental effects on the surfaces. A sensitivity study with regard to these parameters can further classify the effects of the perturbation on interplanetary trajectories. The same is true for the emissivity of the surfaces and the consequent thermal radiation pressure. The used FE model featured some simplifications whose impact on the radiation perturbations is unknown. Refining the model with respect to the potentially varying radiation surface properties of different surfaces of one spacecraft part might have a significant impact on the magnitude and direction of the perturbations. Regarding the thermal radiation pressure, the effect of albedo and infrared on the thermal balance of the spacecraft needs to be considered in future simulations. This impact was omitted here. More precise thermal models including thermal conductivity may yield different thermal radiation pressures as well.

Considering the comparison of simulations to actual flown trajectories, the mass of the spacecraft and the uncertainty of the initial spacecraft states have an influence on the simulations. For a better assessment of the NHPS capabilities it is also helpful to evaluate if the simulation results match the comparison data within their uncertainty. Also, the minimization of the remaining error should be formulated as an orbit-determination problem because the minimization can only be properly done as an optimization.

In this master thesis, only the trajectory of the first Rosetta flyby was examined but the Flyby Anomaly occurs for several more gravity assists. For a closer study of the Flyby Anomaly a revision of the simulation procedure similar to the one of Jouannic et al. [37] could be considered. They propagate the trajectory in two different directions instead of only forward in time. Through this an analysis of the differences at perigee between the two simulations is possible. This kind of analysis might give a different view on the influence of the space environmental effects than the comparison to a baseline simulation or measurement data.

Appendix A

HPS

Table A.1: *Elements of core parameters*

Parameter	**Options**
gravity model	spherical symmetric spherical harmonics model
ocean tide	no yes
solid-Earth tide	no yes
pole tide	no yes
centre-of-mass effect	no spherical potential J_2 potential
post-Newtonian correction	no Schwarzschild + Lense-Thirring + de Sitter
gravity-gradient torque	no spherical potential with gravity gradient matrix

Continuation on next page

Parameter	**Options**
ephemeris model	analytical Montenbruck JPL DE405 JPL DE430 JPL DE431
3rd-body inclusion	no (individually) yes (individually)
IERS2010 convention	complete trafo future EOP estimation only z-rotation
integration-stop time	simulation duration [s]
integration-step size	step size [s]
integration method	Runge-Kutta (8th order) Runge-Kutta (5th order) Adams-Bashforth-Moulton (28th order)
integration error	truncation error [ ]
ECI2ECEF matrix update	every integration sub step inside integration routine simplified inside integration routine every integration step (step size)
gravity field model update	every integration step inside integration routine every step size no
output ECI2ECEF matrix	no yes
output ECEF states ($\boldsymbol{v}$, $\boldsymbol{r}$)	no yes
output number integration-sub steps	no yes
output gravity-gradient torque	no yes
output Ephemeris	no (individually) yes (individually)

Continuation on next page

Parameter	Options
output integration status	no some detailed

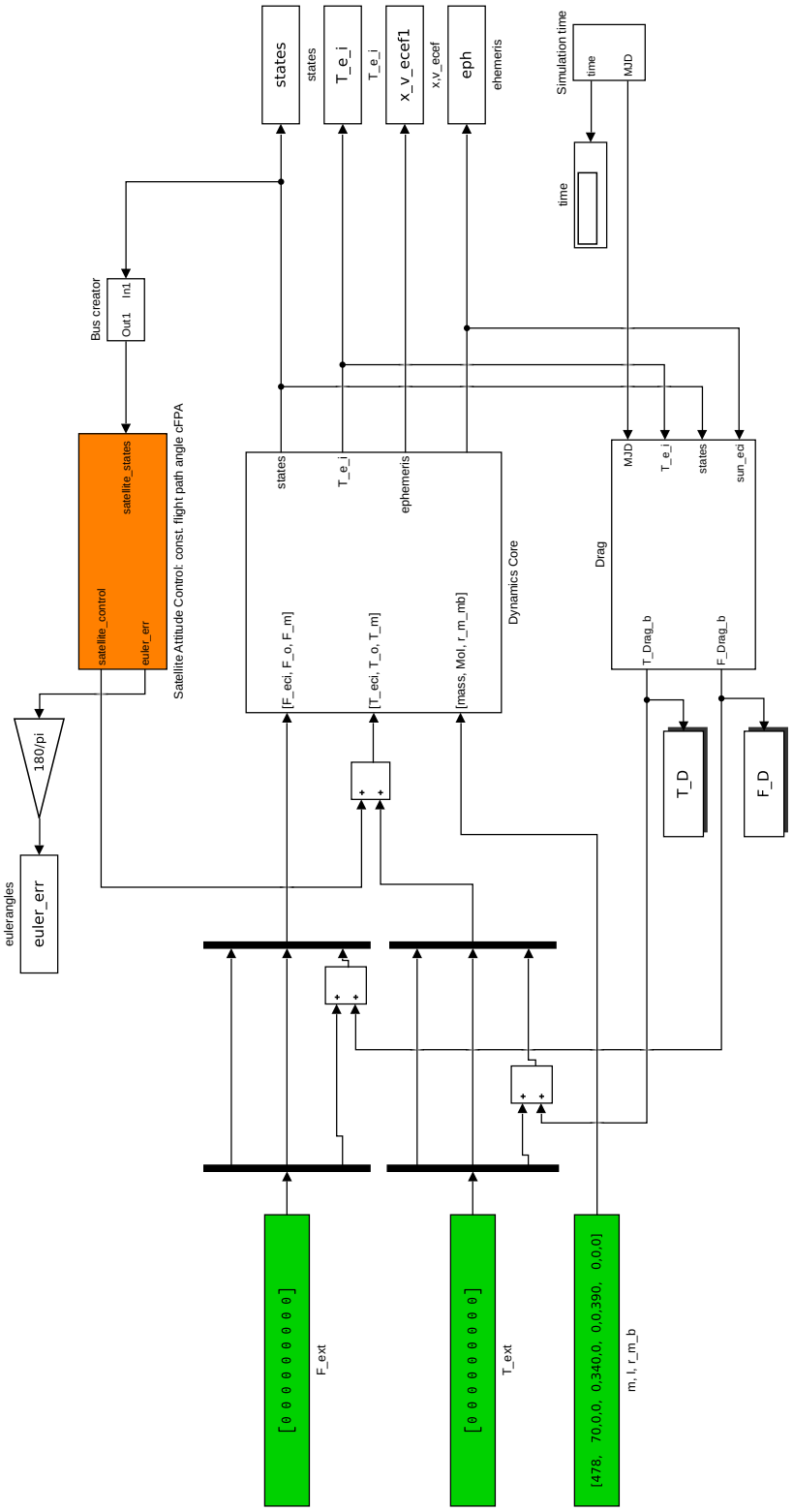

Figure A.1: *Example of an HPS model including atmospheric drag and attitude control*

Appendix B

NHPS

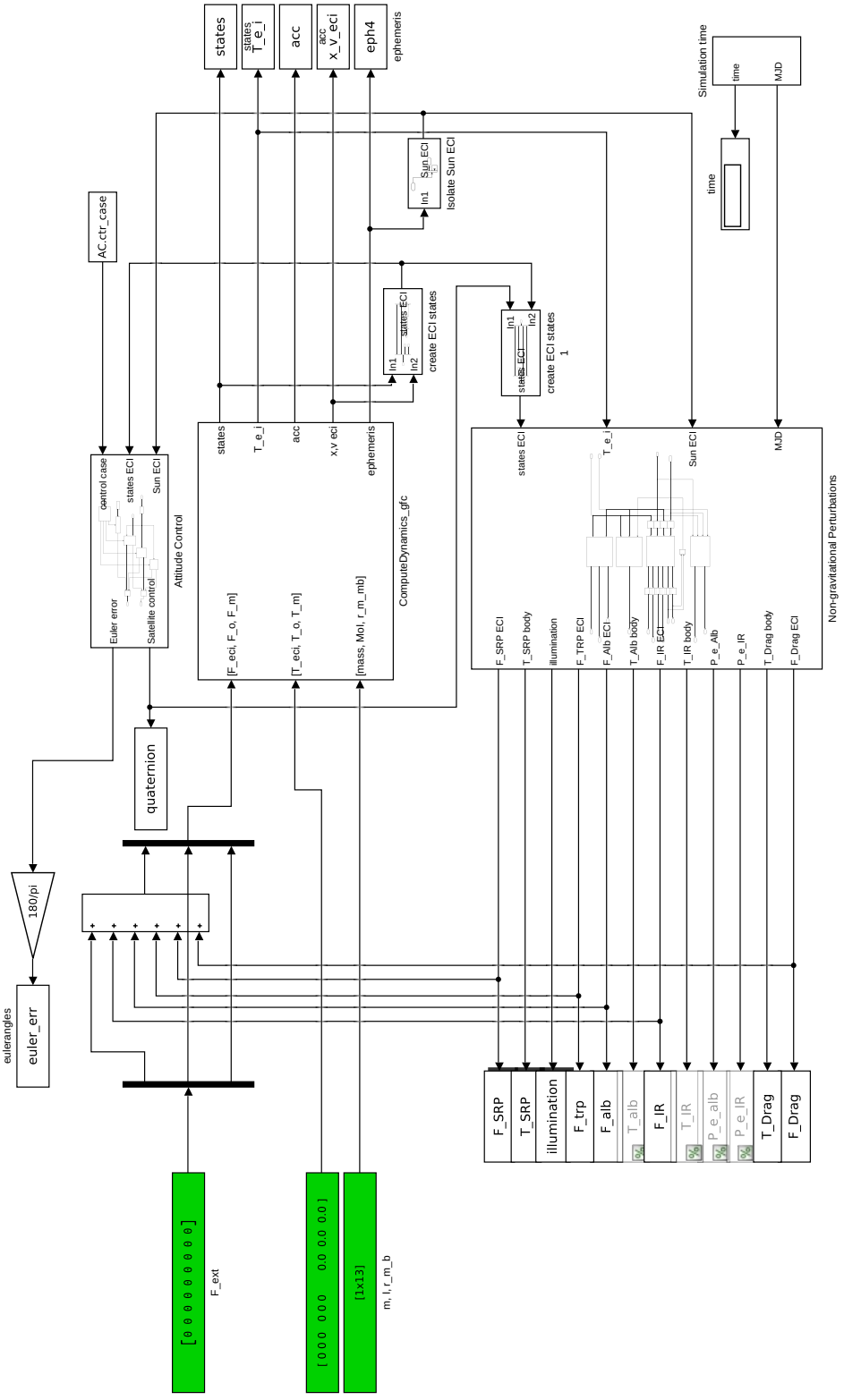

Figure B.1: *NHPS Simulink model including non-gravitational perturbations and attitude control*

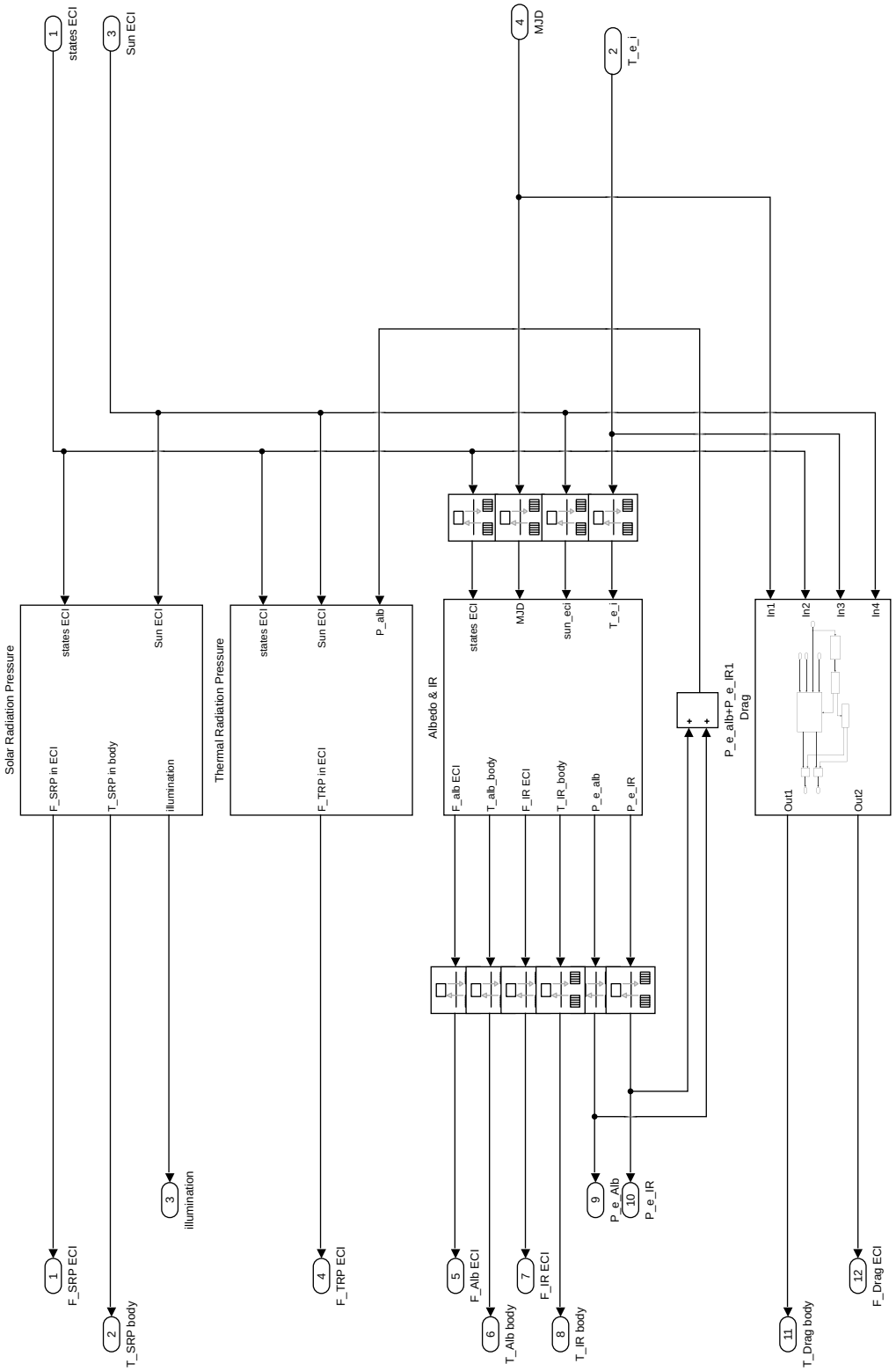

Figure B.2: *NHPS Simulink model of non-gravitational perturbations including SRP, TRP, Earth albedo and infrared and atmospheric drag*

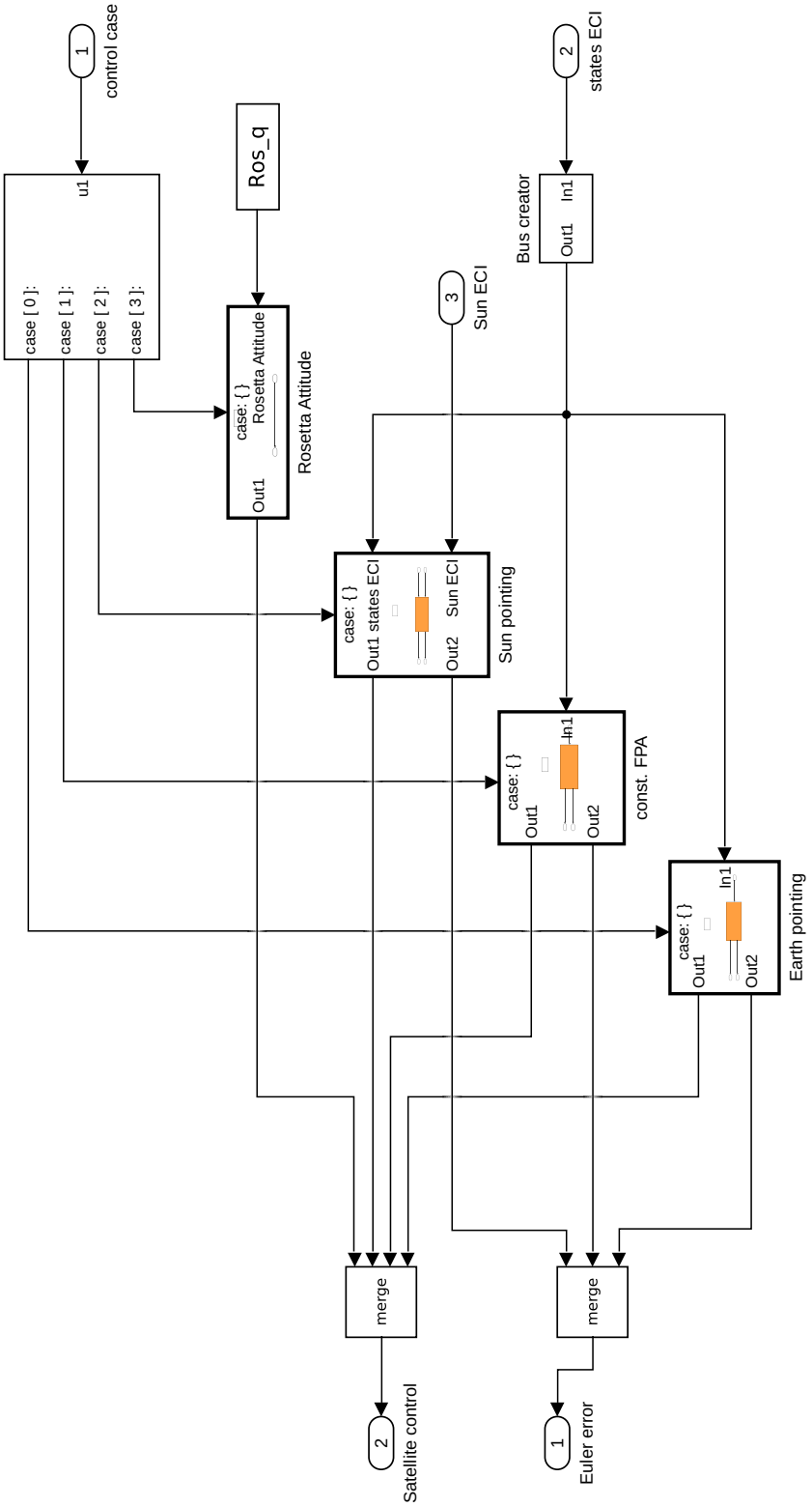

Figure B.3: *NHPS Simulink model of Attitude Control including actual Rosetta attitude, Sun pointing, constant flight path angle, Earth pointing (Nadir)*

Appendix C

Study of Space-Environmental Effects

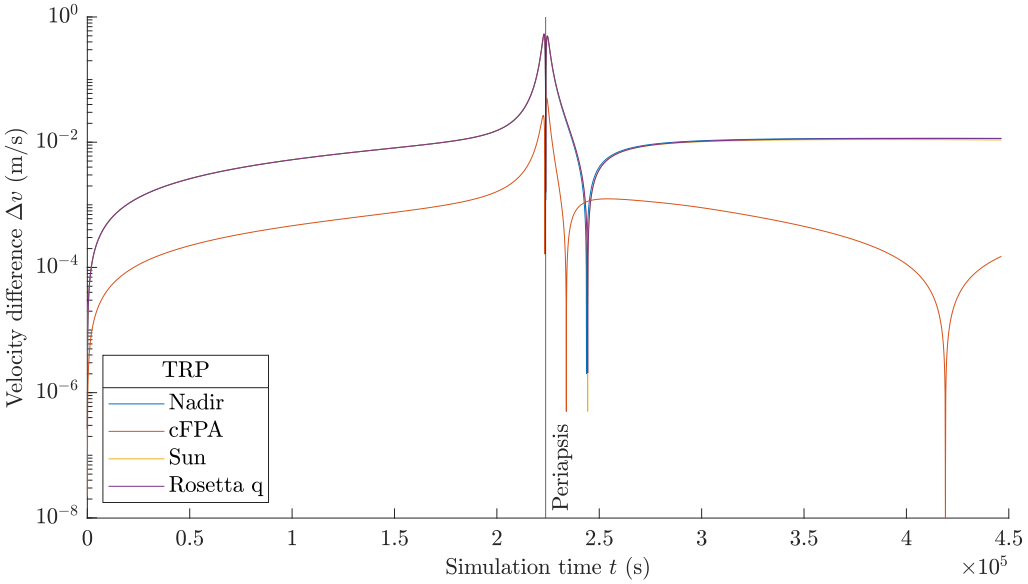

Figure C.1: *The velocity difference to the baseline simulation due to the thermal radiation pressure for four different attitudes plotted in a logarithmic scale over the simulation duration.*

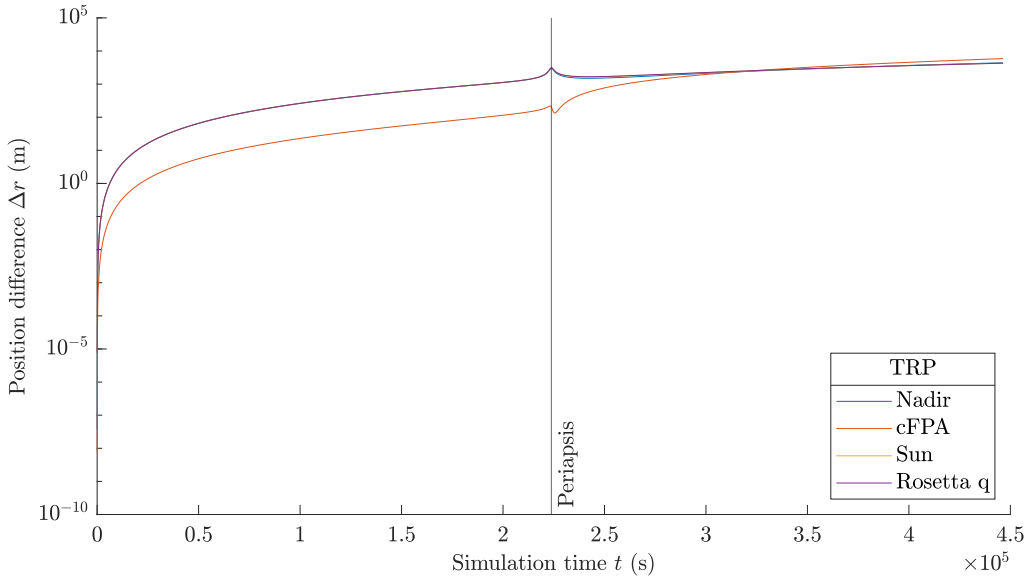

Figure C.2: *The position difference to the baseline simulation due to the thermal radiation pressure for four different attitudes plotted in a logarithmic scale over the simulation duration.*

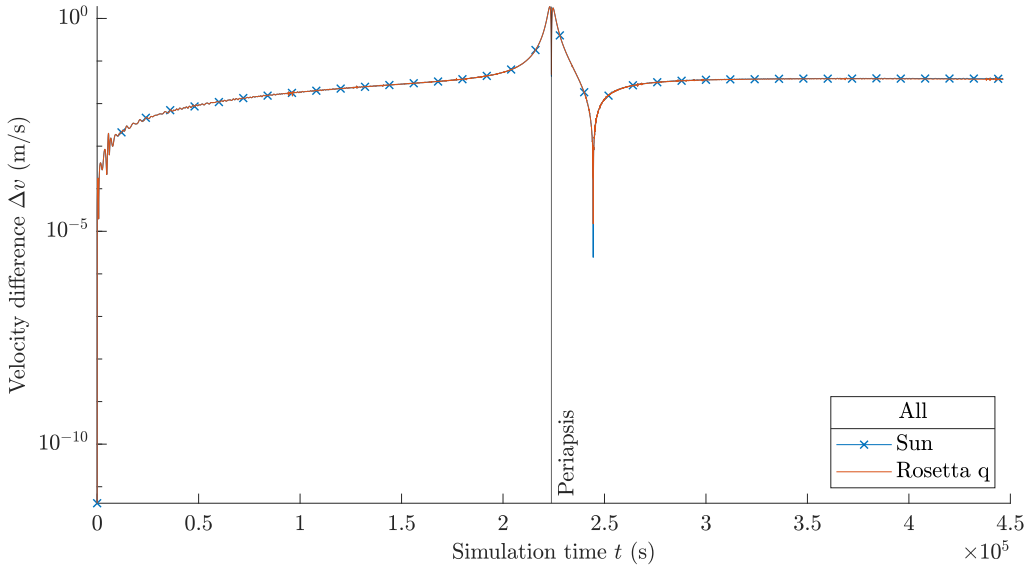

Figure C.3: *The velocity difference of the simulation to the real Rosetta velocity plotted over the simulation duration.*

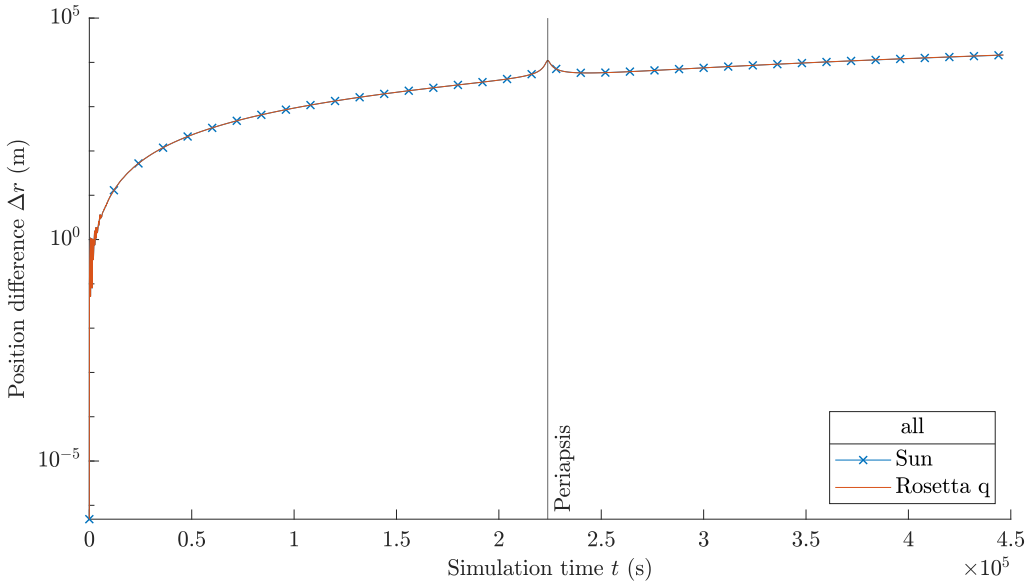

Figure C.4: *The position difference of the simulation to the real Rosetta trajectory plotted over the simulation duration.*

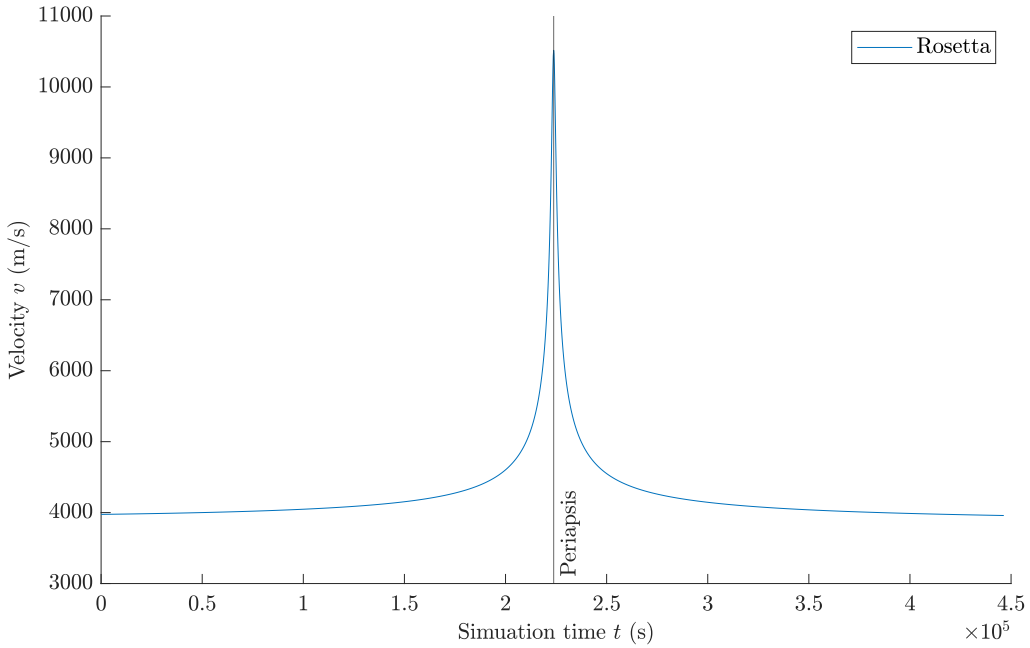

Figure C.5: *The velocity of Rosetta with respect to Earth plotted over the simulation duration.*

Bibliography

[1] John D. Anderson et al. "Anomalous Orbital-Energy Changes Observed during Spacecraft Flybys of Earth". In: *Physical Review Letters* 100.9 (Mar. 3, 2008), p. 091102. ISSN: 0031-9007, 1079-7114.

[2] Peter Antreasian and Joseph Guinn. "Investigations into the unexpected Delta-V increases during the Earth gravity assists of Galileo and NEAR". In: *AIAA/AAS Astrodynamics Specialist Conference and Exhibit*. AIAA/AAS Astrodynamics Specialist Conference and Exhibit. event-place: Boston,MA,U.S.A. American Institute of Aeronautics and Astronautics, Aug. 10, 1998. DOI: 10.2514/6.1998-4287.

[3] Lorenzo Iorio. "The Effect of General Relativity on Hyperbolic Orbits and Its Application to the Flyby Anomaly". In: *Scholarly Research Exchange* 2009 (2009), pp. 1–8. ISSN: 1687-8299, 1687-8302.

[4] Jean Paul Mbelek. "Special relativity may account for the spacecraft flyby anomalies". In: (2009), p. 4.

[5] O Bertolami, F Francisco, and P J S Gil. "Hyperbolic orbits of Earth flybys and effects of ungravity-inspired conservative potentials". In: *Classical and Quantum Gravity* 33.12 (June 23, 2016), p. 125021. ISSN: 0264-9381, 1361-6382.

[6] Stefanie Bremer et al. *HPS Design Document*. ZARM, University of Bremen, Sept. 14, 2013.

[7] Eric Poisson and Clifford M. Will. *Gravity: Newtonian, Post-Newtonian, Relativistic*. Cambridge: Cambridge University Press, 2014. ISBN: 978-1-139-50748-6.

[8] Charles D. Brown. *Elements of Spacecraft Design.pdf*. American Institute of Aeronautics and Astronautics, 2002. 622 pp. ISBN: 1-56347-524-3.

[9] John E. Prussing and Bruce A. Conway. *Orbital mechanics*. New York: Oxford University Press, 1993. 194 pp. ISBN: 978-0-19-507834-3.

[10] Helmholtz Centre Potsdam. *International Centre for Global Earth Models (ICGEM)*. URL: http://icgem.gfz-potsdam.de (visited on 10/27/2020).

[11] Franz Barthelmes. "Global Models". In: *Ecyclopedia of Geodesy* (2014). DOI: 10.1007/978-3-319-02370-0.

[12] Howard D. Curtis. *Orbital mechanics for engineering students*. 1. ed., reprinted. Elsevier Aerospace engineering series. Amsterdam: Elsevier/Butterworth-Heinemann, 2008. 673 pp. ISBN: 978-0-7506-6169-0.

[13] John P. Vinti. "Representation of the Earth's Gravitational Potential.pdf'. In: *Celestial Mechanics* 4.3 (1971), pp. 348–367.

[14] Cambridge University Press. *Cambridge Dictionary*. URL: https://dictionary.cambridge.org/de/worterbuch/englisch/satellite (visited on 09/25/2020).

[15] Stephen Kemble. *Interplanetary mission analysis and design*. Springer-Praxis books in astronautical engineering. Berlin ; New York : Chichester: Springer ; Praxis Publishing, 2006. 484 pp. ISBN: 978-3-540-29913-4.

[16] C. Lämmerzahl, O. Preuss, and H. Dittus. "Is the physics within the Solar system really understood?" In: *arXiv:gr-qc/0604052* (Apr. 11, 2006). arXiv: gr-qc/0604052.

[17] B. D. Tapley et al. "The Joint Gravity Model 3". In: *Journal of Geophysical Research: Solid Earth* 101 (B12 Dec. 10, 1996), pp. 28029–28049. ISSN: 01480227.

[18] Florian Wöske et al. "GRACE accelerometer calibration by high precision non-gravitational force modeling". In: *Advances in Space Research* 63.3 (Feb. 2019), pp. 1318–1335. ISSN: 02731177. DOI: 10.1016/j.asr.2018.10.025.

[19] P. Knocke, J. Ries, and B. Tapley. "Earth radiation pressure effects on satellites". In: *Astrodynamics Conference*. Astrodynamics Conference. Minneapolis,MN,U.S.A.: American Institute of Aeronautics and Astronautics, Aug. 15, 1988. DOI: 10.2514/6.1988-4292.

[20] Benny Rievers et al. "NUMERICAL ANALYSIS OF THERMAL RADIATION PERTURBATIONS FOR A MERCURY ORBITER". In: *Advances in Astronautical Science* (Jan. 2013), p. 21.

[21] R.C. Johnson. *The Slingshot Effect*. Jan. 2003.

[22] C Ma and M Feissel. "Definition and Realization of the International Celestial Reference". In: (June 1997), p. 289.

[23] Gerard Petit and Brian Luzum. *IERS Technical Note; No. 36*. Frankfurt am Main: International Earth Rotation and Reference Systems Service, 2010, p. 179.

[24] Claude Boucher, ed. *The ITRF2000*. IERS technical note 31. OCLC: 177330106. Frankfurt am Main: Verl. des Bundesamts für Kartographie und Geodäsie, 2004. 270 pp. ISBN: 978-3-89888-881-3.

[25] Z. Altamimi et al. *Analysis and results of ITRF2014*. IERS Technical Note No. 38. Frankfurt am Main: Verlag des Bundesamts für Kartographie und Geodäsie, 2017. 73 pp. ISBN: 978-3-86482-088-5.

[26] C. Boucher and Z. Altamimi. "ITRS, PZ-90 and WGS 84: current realizations and the related transformation parameters". In: *Journal of Geodesy* 75.11 (Nov. 1, 2001), pp. 613–619. ISSN: 0949-7714, 1432-1394.

[27] H. M. Nautical Almanac Office. *Explanatory Supplement to the Astronomical Ephemeris and the American Ephemeris and Nautical Almanac*. 1961.

[28] Oliver Montenbruck and Thomas Pfleger. *Astronomie mit dem Personal Computer*. Berlin, Heidelberg: Springer Berlin Heidelberg, 1994. ISBN: 978-3-662-05861-9.

[29] James Diebel. "Representing Attitude: Euler Angles, Unit Quaternions, and Rotation Vectors". In: (Oct. 20, 2006), p. 35.

[30] Dietmar Gross et al. *Technische Mechanik 3*. Springer-Lehrbuch. Berlin, Heidelberg: Springer Berlin Heidelberg, 2015. ISBN: 978-3-642-53953-4.

[31] Bob Palais, Richard Palais, and Stephen Rodi. "A Disorienting Look at Euler's Theorem on the Axis of a Rotation". In: *American Mathematical Monthly* 116.10 (Dec. 1, 2009), pp. 892–909. ISSN: 00029890, 19300972.

[32] Shiyu Zhao. "Time Derivative of Rotation Matrices: A Tutorial". In: (Sept. 20, 2016).

[33] William M Folkner et al. "The Planetary and Lunar Ephemerides DE430 and DE431". In: (Feb. 15, 2014), p. 81.

[34] Kurt Magnus and Hans H Müller-Slany. *Grundlagen der Technischen Mechanik*. OCLC: 957697427. 2009. ISBN: 978-3-8351-0007-7.

[35] Brian Harvey and Olga Zakutnyaya. *Russian space probes: scientific discoveries and future missions*. Springer-Praxis books in space exploration. New York: Springer, 2011. 514 pp. ISBN: 978-1-4419-8149-3.

[36] Paul F Thompson et al. "Reconstruction of EarthFlyby by the Juno spacecraft". In: (2014), p. 14.

[37] B Jouannic and R Noomen. "The Flyby Anomaly: An Investigation into Potential Causes". In: (2015), p. 17.

[38] National Aeronautics and Space Administration. *General Mission Analysis Tool (GMAT) Mathematical Specification*. Mar. 2020.

[39] Theodore D. Moyer. *Mathematical Formulation of the Double-Precission Orbit Determination Program (DPODP*. May 15, 1971.

[40] NASA. *GEODYN Software Package*. Jan. 8, 2020. URL: `https://space-geodesy.nasa.gov/techniques/tools/GEODYN/GEODYN.html` (visited on 04/20/2020).

[41] W Kahan. "IEEE Standard 754 for Binary Floating-Point Arithmetic". In: (1997), p. 30.

[42] John J. McCarthy et al. *GEODYN Systems Description Volume 1*. Feb. 2015.

[43] M Vasile. "On the Preliminary Design of Multiple Gravity-Assist Trajectories". In: (2011), p. 35.

[44] Sam Wagner and Bong Wie. "Hybrid Algorithm for Multiple Gravity-Assist and Impulsive Delta-V Maneuvers". In: *Journal of Guidance, Control, and Dynamics* 38.11 (Nov. 2015), pp. 2096–2107. ISSN: 0731-5090, 1533-3884.

[45] Volker Maiwald. "Optimization of Low-Thrust Gravity-Assist Trajectories under Application of Tisserand's Criterion". Dissertation. Bremen: University Bremen, 2018.

[46] Paul Melchior. "Earth Tides". In: *Geophysical Surveys* 1 (1974), pp. 275–303.

[47] Stefanie Bremer et al. *HPS Usere's Guide*. ZARM, University of Bremen, Sept. 14, 2013.

[48] F Barlat and J Lian. *Mechanical APDL Element Reference*. Nov. 2011.

[49] Srinivas Bettadpur. *GRACE Product Specification Document*. Austion: Centre of Space Research, The University of Texas, May 2012.

[50] James Richard Wertz and Wiley J. Larson, eds. *Space mission analysis and design*. 3rd ed. Space technology library. El Segundo, Calif. : Dordrecht ; Boston: Microcosm ; Kluwer, 1999. 969 pp. ISBN: 978-0-7923-5901-2.

[51] N. Karjanto. "Properties of Chebyshev polynomials". In: (Feb. 3, 2020).

[52] Greg Miller. *Format of the JPL Ephemeris Files*. Greg Miller's Astronomy Programming. 2019. URL: `http://www.astrogreg.com/jpl-ephemeris-format/jpl-ephemeris-format.html` (visited on 07/10/2020).

[53] Ryan S. Park and Alan B. Chamberlin. *HORIZONS Web-Interface*. 1996. URL: `https://ssd.jpl.nasa.gov/horizons.cgi` (visited on 07/10/2020).

[54] David Goldberg. "What every computer scientist should know about floating-point arithmetic". In: *ACM Computing Surveys* 23.1 (Mar. 1991), pp. 5–48. ISSN: 0360-0300, 1557-7341.

[55] John D. Anderson, James K. Campbell, and Michael Martin Nieto. "The Energy Transfer Process in Planetary Flybys". In: *New Astronomy* 12.5 (July 2007), pp. 383–397. ISSN: 13841076. arXiv: `astro-ph/0608087`.

[56] Bruce Bowman et al. "A New Empirical Thermospheric Density Model JB2008 Using New Solar and Geomagnetic Indices". In: *AIAA/AAS Astrodynamics Specialist Conference and Exhibit*. AIAA/AAS Astrodynamics Specialist Conference and Exhibit. Honolulu, Hawaii: American Institute of Aeronautics and Astronautics, Aug. 18, 2008. ISBN: 978-1-62410-001-7.

[57] T. Morley and F. Budnik. "Rosetta Navigation at its first Earth Swing-By". In: 19th International Symposium on Space Flight Dynamics. Kanazawa, Japan, 2006.